Department of Precision and Microsystems Engineering

Topology Optimisation of Pressure-Actuated Soft Robots

Dehlia Hedera Iris Menger

Report no : 2024.005
Coach : Dr. Ir. S. Koppen
Professor : Prof. Dr. Ir. M. Langelaar
Specialisation : Computational Design and Mechanics
Type of report : Master Thesis
Date : 31st January

Delft University of Technology

Department of Precision and Microsystems Engineering

Topology Optimisation of Pressure-Actuated Soft Robots

Thesis Document
Submitted in Partial Fulfillment of the Requirements
for the Degree of Master of Science in Mechanical Engineering

Author:
Dehlia Hedera Iris Menger
4649451

Committee Members:

Prof. Dr. Ir. M. Langelaar
Dr. Ir. S. Koppen
Dr. Ir. R.A.J. van Ostayen
Dr. J. Wu

TU Delft

Contents

Acknowledgements

This section is dedicated to acknowledging the instrumental contributions of individuals who have significantly enriched my research experience throughout this thesis. I am grateful for the opportunity and wish to express my gratitude to my supervisors, Matthijs Langelaar and Stijn Koppen. The success of this thesis owes much to their guidance, expertise, support, and thorough checking of my work.

Furthermore, I extend my appreciation to Ron van Ostayen. His comprehensive understanding and expertise in COMSOL significantly contributed to the enhancement of my COMSOL skills. With his instrumental guidance and remarkable ability to facilitate action and provide assistance, I could handle the complexities of COMSOL. One example is that one day, the COMSOL server broke for the second time. Despite numerous emails, the issue remained unresolved. However, after seeking Ron's assistance, the server was fixed within a day. This example is only one of the many.

My gratitude extends to Josh Pinskier, who assisted me with COMSOL and went above and beyond to help me proceed with my studies in Australia. Although the plan to go to Australia did not become a realisation, Josh's support persisted. I also want to thank Prabhat Kumar for his shared knowledge and keen interest in this thesis.

My heartfelt thanks extend to my old and new friends who patiently listened to my thesis struggles and respected my choice to skip some late-night fun to start early in the mornings. Their knowledge, support, and love throughout this journey have been unwavering. Their consistent encouragement has been the driving force behind both my academic and personal growth. They made this experience enjoyable and enriching.

Special appreciation goes to my family—Eric, Carin, Iris, Hedera, and Rutger—who supported me unconditionally at every step. Their support took various forms, whether through wise advice from different perspectives or financial support, and even in the form of enjoyable evenings filled with games and delicious food. I also should not forget to thank the extended family—Koen and Ellen—for the enjoyable conversations and moments.

Finally, I would like to thank Daniel for always being there and giving me a listening ear or a hug when needed. His never-ending stories, wisdom, good advice, and love helped me through the frustrating times.

Dehlia Hedera Iris Menger
Delft, January 2024

Abstract

Soft robots, characterised by compliant mechanisms (CMs) made from low-stiffness materials, offer improved adaptability compared to traditional, rigid robots. These CMs are often actuated by pressure loads. Moreover, soft robots provide new possibilities in the area of robotics. They can be used in search and rescue and interact safely in collaboration with humans.

The current state-of-the-art in Topology Optimisation (TO) for design-dependent pressure-actuated CMs (PACMs) relies heavily on linear models. The determination of design-dependent pressure loads involves employing the Darcy method, which integrates Darcy's law with the drainage term to obtain the pressure field. Subsequently, the finite element method (FEM) is used to transform the pressure field into consistent nodal forces. However, it is crucial to acknowledge that these linear models are only valid for small displacements.

This thesis introduces a novel approach by incorporating nonlinearities into the solid mechanics of the TO process for PACMs in conjunction with the Darcy method. Additionally, this work incorporates nonlinearities into the solid mechanics of the TO process for PA multi-material compliant mechanisms, presenting another novel method.

Four nonlinearities in the solid mechanics of PA soft robots may occur, two of which are addressed in this thesis: geometric nonlinearities and a hyperelastic material model. Geometric nonlinearities arise from large deformations caused by high applied pressures. The Neo-Hookean material model is implemented to describe the low-stiffness material accurately.

The TO of pressure-actuated (PA) soft robots is simulated using COMSOL, a commercial software program for multi-physics simulation. This research presents a detailed comparison between theoretical predictions and practical outcomes as realised in COMSOL. Furthermore, this thesis includes a case study validating the successful implementation of the new method, covering a PA inverter, a PA compliant gripper, a PA member of the Pneumatic Networks, and a PA multi-material compliant gripper. The obtained results indicate limitations on the allowable applied pressure loads for the mechanisms, specifically in the case of the PA member of the Pneumatic Networks and a PA multi-material-compliant gripper. However, the PA inverter and PA compliant gripper validate the expectation that incorporating a hyperelastic material model yields significantly different results than the linear elastic material model. Moreover, the TO with the hyperelastic material model can predict displacements more accurately than the linear TO, as the differences between the displacements obtained from the TO and the analysis align more closely.

The Wang method is investigated to observe its influence on the range of the applied pressure loads during the TO of PA soft robots. The Wang method employs an interpolation technique that interpolates between linear and nonlinear theories. In this approach, void elements are described using linear theory, while solid elements are characterised by nonlinear theory. This interpolation method is developed to address distorted elements during large displacements. It effectively extended the range of applied loads during the TO of structures. However, it is found that this method does not influence the range of the applied load during the TO of CMs.

Nomenclature

Symbol	Description	unit
β_k	Parameter to control the rate of change of the flow coefficient K	-
$\boldsymbol{\chi}$	Motion of the body $\mathbf{x} = \boldsymbol{\chi}(\mathbf{X}, t)$	m
$\boldsymbol{\epsilon}$	Linearised Green-Lagrange strain	-
η_k	Parameter to control when the flow coefficient K changes from K_v to K_s	-
γ_e	Interpolation factor to interpolation between linear and nonlinear theory	-
Γ	Complete boundary	m^2
Γ_e	Element boundary	m^2
κ	Permeability of a material	N/m^3
λ	First Lamé parameter	N/m^2
λ_i	Eigenvalues of **C** with i = 1,2,3	
μ	Second Lamé parameter; shear modulus	N/m^2
μ_f	Fluid viscosity	N/m^2 s
∇	Gradient operator	m^{-1}
ν	Poisson ratio	-
ϕ	Interpolated strain energy density function	J/m^3
ϕ_{HE}	Neo-Hookean strain energy density function	J/m^3
ϕ_L	Linear strain energy density function	J/m^3
ϕ_{VK}	Saint Venant-Kirchhoff strain energy density function for small deformation	J/m^3
Π	Total potential energy	J
Π^{ext}	External potential energy	J
Π^{int}	Internal potential energy	J
Ω	Total domain	m^3
Ω_0	Domain of the initial configuration of the body	m^3
$\partial\Omega_{0,\sigma}$	Boundary surface where the traction vector **t** is prescribed	m^2
Ω_e	Element domain	m^3
$\boldsymbol{\rho}$	Vector of design variables	-
ρ_e	Value design variables of element	-
$\boldsymbol{\sigma}$	Linear stress	N/m^2
A	Global flow matrix	-
$\mathbf{A}_e$	Flow matrix of the element	-
b	Body force	N
B	Matrix of spatial derivatives of the matrix of shape functions	m^{-1}
$\mathbf{B}_p$	Matrix of spatial derivatives of the vector of shape functions	m^{-1}
C	Right Cauchy-Green deformation tensor	-
$\mathbf{C}_{min}$	Compliance	m/N
D	Elastic modulus	N/m^2
D_s	Drainage coefficient	$m^2N^{-1}s^{-1}$
e	Element index parameter	-
E	Young's modulus	N/m^2
E_e	Element Young's modulus	N/m^2
E_0	Young's modulus for the void elements ($\rho_e = 0$)	N/m^2
E_i	Young's modulus for the solid elements ($\rho_e = 1$) with i=1 for a single material problem and i=1,2 for a multi-material problem	N/m^2
$\mathbf{E}_{W,i}$	The ith strain interpolation method with i = 1,2,3	-
$\mathbf{E}_{GL}$	Green-Lagrange strain tensor	-
f_0	Objective function	-

$\mathbf{f}$	Global force vector	N
$\mathbf{f}_d$	Unit dummy load	N
$\mathbf{f}_e$	Nodal force vector	N
$\mathbf{f}^{ext}$	External force vector	N
$\mathbf{f}_{flow,e}$	Loading vector of the element	m^3/s
$\mathbf{f}_{flow}$	Global loading vector	m^3/s
$\mathbf{f}^{int}$	Internal force vector	N
$\mathbf{F}$	Deformation gradient tensor	-
$\mathbf{H}_e$	Conversion matrix from nodal pressures $\mathbf{p}^e$ to the nodal loads $\mathbf{f}_e e$	m^2
$\mathbf{H}$	Conversion matrix from nodal pressures $\mathbf{p}$ to the nodal loads $\mathbf{f}$	m^2
$\mathbf{I}$	Identity matrix	
I_1	First invariant of $\mathbf{C}$	-
I_3	Third invariant of $\mathbf{C}$	-
K	Flow coefficient	Nm^4/s
K_s	Flow coefficient for solid elements ($\rho_e = 1$)	Nm^4/s
K_v	Flow coefficient for void elements ($\rho_e = 0$)	Nm^4/s
$\mathbf{K}$	Global stiffness matrix	N/m
$\mathbf{K}_e$	Element stiffness matrix	N/m
$\mathbf{n}$	Boundary normal vector	-
$\mathbf{N}$	Matrix of Shape functions	-
$\mathbf{N}_p$	Vector of Shape functions	-
p	Penalisation factor	-
p_{out}	Output pressure	N/m^2
$\mathbf{p}$	Pressure vector	N/m^2
$\mathbf{p}_e$	Nodal pressure values of the element	N/m^2
$\mathbf{q}$	Darcy flux; volume velocity through porous medium	m/s
$\mathbf{q}_\Gamma$	Prescribed Darcy flux at the boundary	m/s
Q_{drain}	Volumetric drainage per second per unit volume (Drainage term)	s^{-1}
r	Ratio of input pressure to pressure at depth Δs	m
$\mathbf{S}$	Interpolated second Piola-Kirchhoff stress in the EMMI method	N/m^2
$\mathbf{S}_L$	Linear second Piola-Kirchhoff stress	N/m^2
$\mathbf{S}_{NL}$	Nonlinear second Piola-Kirchhoff stress	N/m^2
Δs	Penetration depth of the pressure	m
$\mathbf{t}$	Traction force	N
$\mathbf{u}$	Displacement vector	m
$\mathbf{u}_e$	Nodal displacements vector	m
$\mathbf{v}$	Displacement vector due to the dummy load fd	m
V	Volume	m^3
$V*$	Permitted volume	m^3
W^{ext}	External work	J
W_e^{ext}	Element external work	J
W^{int}	Internal work	J
$\mathbf{x}$	Spatial coordinates	m
$\mathbf{X}$	Material coordinates	m

List of abbreviations

Abbreviation	Description
ALE	Arbitrary Lagrangian-Eulerian
CM	Compliant Mechanism
DOF	Degree Of Freedom
FEA	Finite Element Analysis
FEM	Finite Element Method
GCMMA	Global Convergent Method of Moving Asymptotes
MSE	Mutual Strain Energy
PA	Design-dependent Pressure-Actuated
PACM	Design-dependent Pressure-Actuated Compliant Mechanism
PSBM	Pseudo-Rigid Body Model
PneuNets	Pneumatic Networks
SE	Strain Energy
SEDF	Strain Energy Density Function
SIMP	Simplified Isotropic Material with Penalisation
TO	Topology Optimisation

List of Figures

List of Tables

1

Introduction

Currently, robots are indispensable in our society, used in applications for medicine, industrial production, and agriculture. Conventional, rigid robots have been crucial in industry due to their precision, high speed, and repeatability. These robots are built with rigid joints, such as revolute and prismatic joints, limiting their degrees of freedom (DOFs). To function effectively, these rigid robots require complex sensing and control systems. As the demand for more versatile and adaptable robots grows, the focus has shifted towards soft robots.

Soft robots, known for their lightweight and flexible structures, offer new functionalities in robotics. Examples of these functionalities are safe interaction with fragile objects and adapting to various shapes and tasks, and their monolithic (compliant) design makes production using additive manufacturing possible. Combining soft materials with advanced 3D and 4D printing makes it possible to create soft robots for tasks like search and rescue and safe collaboration with humans (Pinskier and Howard 2022). In contrast to conventional robots that rely on sliding or rolling for motion, soft robots achieve movement through their soft materials, which are materials with a low stiffness (Chen et al. 2020). Figure 1.1 illustrates an example of a soft robot capable of picking up a raw egg.

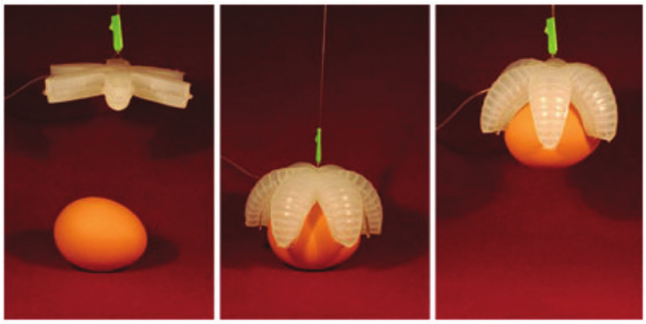

Figure 1.1: An example of a soft robot: a soft gripper picking up a raw egg. This figure is obtained from Shintake et al. (2018)

Compliant mechanisms

Soft robots feature compliant mechanisms (CMs), which achieve motion through flexible components, often replacing rigid elements. Not only are CMs simple designs, but the use of CMs also reduces maintenance requirements in engineering systems. The characteristics of CMs offer numerous advantages, including friction-free motion, high precision, and the absence of assembly processes.

However, designing CMs remains a challenging task (Howell 2001). Various design methods are available, with the Pseudo-Rigid-Body model (PRBM) and Topology optimisation (TO) being the most common. In the PRBM Method, complex flexible structures are simplified by representing the deflection path using the kinematics of a rigid-body mechanism, approximating the stiffness of the flexible members by springs.

This thesis will employ TO since it has demonstrated promising results in the design of soft robots (Pinskier, Kumar, et al. 2023). In the TO process, designers divide the design domain into finite elements, forming a mesh. Consequently, the material distribution is optimised to obtain the best objective function.

The research topic in this thesis is modelling design-dependent pressure-actuated CMs (PACM [1]) using TO. This choice is driven by the observation that actuation primarily relies on design-dependent loads during the TO of soft robots, which are more frequently used than actuation driven by design-independent loading. Design-independent loads, such as constant forces, are independent of the mechanism's design during the TO. In contrast, design-dependent loads rely on the design and change as the load boundary evolves throughout the TO process (Kumar and Langelaar 2022). Examples of design-dependent loads include pneumatic or hydraulic pressures, which are design-dependent relying on the problem statement.

Design-dependent pressure-actuated compliant mechanisms
PA compliant mechanisms (PACMs) are commonly used as soft robots. Incorporating these design-dependent pressure loads into the formulations is crucial, as demonstrated by Kumar, Frouws, et al. (2020). A schematic view in Figure 1.2 shows a design problem where pressure loads are applied on boundary Γ_p. The possible result of the TO of the problem of Figure 1.2a is illustrated in Figure 1.2b. These subfigures serve the purpose of introducing the reader to the TO of PACMs.

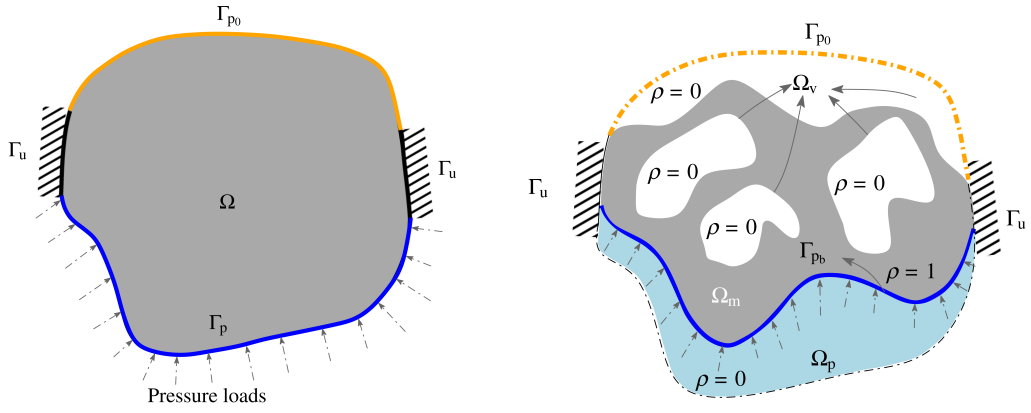

(a) A pressure loading design problem

(b) A possible outcome for TO problem of (a)

Figure 1.2: a) An example of a design problem with design-dependent pressure loading which are the dash-dotted arrows on the pressure boundary Γ_p. b) A possible outcome for the TO problem of (a). Here, Γ_{p_b} = the evolving pressure boundary. Γ_{p_0} = the zero pressure boundary. Γ_u = the boundary where displacements are fixed. ρ = the material density. Ω = the design domain. Ω_m = the solid domain where $\rho = 1$. Ω_v = the void domain where $\rho = 0$. Ω_p = the pressure domain where $\rho = 0$. The figure is obtained from Kumar, Frouws, et al. (2020).

Designing PACMs introduces challenges inherent to their complexity and soft robotic characteristics (Kumar and Langelaar 2022; Kumar, Frouws, et al. 2020). These challenges include identifying the pressure boundary, defining the relationship between the pressure and the design variables, calculating load sensitivities, and incorporating nonlinearities.

The challenge in identifying the pressure boundary arises from the difficulty of determining the solid-void boundary, primarily due to intermediate values for the design variables during the TO process. The most recent TO methods for PACMs employ the Darcy method (Kumar, Frouws, et al. 2020; Kumar and Langelaar 2022) to overcome the first three challenges mentioned in the previous paragraph. This method is detailed in Chapter 3 and provides the derivation of the relationship between the pressure and the design variables. To better understand the load sensitivity derivation, readers are referred to the work by Kumar, Frouws, et al. (2020).

[1]The reader should note that PA means design-dependent pressure-actuated

The state-of-the-art in TO of PACMs primarily incorporates a linear model. However, Kumar and Langelaar (2022) stated that incorporating full nonlinear mechanics in the design formulation has a significant effect. They analysed the incorporation of geometric nonlinearities, a Neo-Hookean material model, and a follower load on the obtained results from the TO of a PA inverter and PA compliant gripper. The analysis revealed a 90% decrease in displacements for the PA inverter compared to the linear analysis and a 76% decrease for the PA compliant gripper. Hence, their influence is significant and crucial to consider. The reader should note that the objective function was a minimisation; therefore, a decrease means improvement.

Despite these advancements, the challenges of incorporating nonlinearities caused by deformation-dependent pressures, large displacements, and the use of low-stiffness materials in soft robots still need to be addressed. The subsequent paragraph explains the four nonlinearities encountered in the solid mechanics of PA soft robots.

The four nonlinearities in the solid mechanics of pressure-actuated soft robots
Designers encounter four types of nonlinearities in the solid mechanics of PA soft robots, categorised based on the relationships between mechanical properties (Kim 2015), as illustrated in Figure 1.3. The four nonlinearities are enumerated as follows:

1. **Geometric nonlinearity** Geometric nonlinearities arise when there is a nonlinear relation between the strain and the displacement. They typically occur when structures and CMs undergo large displacements due to their soft materials, leading to significant changes in the geometry (Holzapfel 2000). During TO, if large deformations occur, low-stiffness elements may experience excessive distortion, potentially resulting in inverted elements. These distortions can introduce numerical instabilities in the Newton-Raphson iterations (Wang, Lazarov, Sigmund, and Jensen 2014).
2. **Material nonlinearity** To accurately model the behaviour of soft materials, it becomes necessary to implement hyperelastic materials. This implementation introduces the second type of nonlinearity, known as material nonlinearity, which involves the nonlinear relationship between strain and stress (Holzapfel 2000).
3. **Boundary nonlinearity** Boundary nonlinearities result from nonlinear boundary conditions, representing a nonlinear connection between the displacement and the prescribed displacement. When soft robots deform significantly, it is possible that (self-)contact can occur, leading to boundary nonlinearities (Kim 2015).
4. **Force nonlinearity** The fourth type is force nonlinearity, characterised by nonlinear force boundary conditions, representing a nonlinear relationship between the stress and the applied forces. This nonlinearity is particularly relevant for PACMs, where the magnitude, direction, or location of the pressure loads change due to deformation, resulting in force nonlinearities. Loads that exhibit force nonlinearities are called follower forces (Kim 2015).

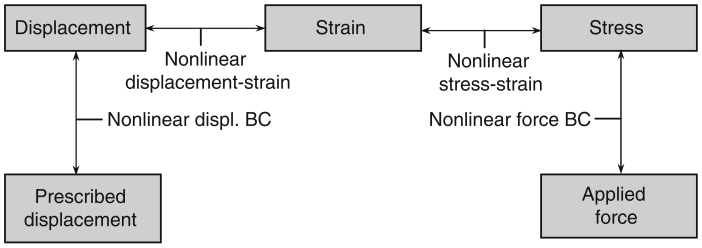

Figure 1.3: The different types of nonlinearities involved in the solid mechanics of the TO process and their nonlinear relationship with the parameters of the solid mechanics. This figure is obtained from Kim (2015)

Literature review design-dependent pressure-actuated soft robots
Kumar, Frouws, et al. (2020) conducted a literature review on methods developed for the TO of PACMs. They examined various existing approaches; however, they concluded that each method fell short in addressing at least one of the first three challenges encountered when designing PACMs, mentioned on page 2. Consequently, they developed an approach combining Darcy's law with the drainage term to handle pressure loads effectively.

The method developed by Kumar, Frouws, et al. (2020) has demonstrated its effectiveness in three-dimensional PA soft robots (Kumar and Langelaar 2021), multi-material pneumatically actuated soft robots (Pinskier, Kumar, et al. 2023), and the TO of a member of the Pneumatic Networks (Kumar 2023). Additionally, Kumar and Langelaar (2022) has developed a robust TO approach for synthesising PACMs by modelling pressures using Darcy's law. However, these papers do not include nonlinearities in the solid mechanics.

Caasenbrood et al. (2020) incorporated nonlinearities into the solid mechanics for the TO of PA soft robots. Nevertheless, Pinskier, Kumar, et al. (2023) stated that the results obtained from the method of Caasenbrood et al. (2020) result in unrealistic designs with disconnected areas of pressure. Additionally, a drawback is that the algorithm heavily depends on the user's skills, making it difficult for a wide range of users to utilise it successfully. The algorithm requires a high level of expertise to operate effectively, and it contains complex parameters that are only adjustable with a deep understanding of the algorithm.

To the best of the authors' knowledge, nonlinearities have not been implemented in the solid mechanics of the TO of PA soft robots in conjunction with the Darcy method. Furthermore, to the best of the authors' knowledge, nonlinearities have not been implemented in the solid mechanics of the TO of multi-material PA soft robots.

Contribution

For numerous systems, the linear theory sufficiently describes the behaviour of various systems in our lives accurately. However, due to the large displacements possible in PA soft robots and the low stiffness material used, the linear theory is not accurate enough to describe the behaviour of the PA soft robots anymore. A 'reality' gap can be encountered when using the linear theory in the TO to design PA soft robots. This reality gap represents the mismatch between the behaviour of the simulated designs and their actual functionality in real-world scenarios (Pinskier and Howard 2022). As discussed before, the significance has been investigated by Kumar and Langelaar (2022). When accounting for nonlinearities, the behaviour of the PA soft robots can be described more accurately, effectively bridging this gap.

This thesis builds upon the method developed by Kumar, Frouws, et al. (2020) by introducing geometric nonlinearities and a hyperelastic material model to reduce the gap. Due to time constraints, force and boundary nonlinearities have not been incorporated into solid mechanics.

The programs COMSOL and MATLAB are used in this thesis. COMSOL is a commercial software program for multi-physics simulation and modelling. It is used for the modelling, simulation and analysis of the soft robots. MATLAB is a widely used program for numerical computing, data analysis, and mathematical modelling. It is used for deriving specific equations and calculations.

This thesis introduces a novel TO method for PA single-material and PA multi-material soft robots. The method is developed in conjunction with the Darcy method and involves the incorporation of geometric nonlinearities and a hyperelastic material model in solid mechanics. It is important to emphasise that the TO method for PA single-material soft robots is specifically novel when combined with the Darcy method, as previous approaches have already implemented geometric nonlinearities and a hyperelastic material model. However, to the best of the author's knowledge, this thesis introduces the first method to incorporate these nonlinearities into the solid mechanics of the TO process for PA multi-material soft robots.

Furthermore, it investigates how geometric nonlinearities and a hyperelastic material model can be incorporated into the TO of soft robots in conjunction with the Darcy method in COMSOL. Implementing the TO of PACM is highly user-dependent when using MATLAB, as it heavily relies on the user's skills, knowledge, and preferences. In contrast, COMSOL is a user-friendly program offering robust model implementation. By 'robust,' we mean that the implementation in COMSOL is significantly less dependent on individual user factors, providing a more standardised and accessible approach. Users can perform the TO of even the most complex geometries with only basic knowledge. Moreover, adding solid mechanics and physics to these geometries is simple.

Research questions
The aim of this thesis is to incorporate geometric nonlinearities and a hyperelastic material model into the solid mechanics of the TO process for PA soft robots. This incorporation aims to provide a more accurate description of their behaviour compared to linear models. Furthermore, the TO is performed in conjunction with the Darcy method, and simulations are conducted using COMSOL.

To achieve the thesis aim, this research represents the following key questions:

SQ1 ***To what extent can geometric nonlinearities and a hyperelastic material model be incorporated into the solid mechanics of the topology optimisation process for design-dependent pressure-actuated soft robots in COMSOL?***

During the modelling process in COMSOL, large applied pressure loads can result in large displacements of the PACMs. As discussed in chapter 4, these large displacements result in inverted elements, leading to numerical instabilities. These instabilities, in turn, limit the maximum applied pressure load. This subquestion explores the feasibility of incorporating geometric nonlinearities and a hyperelastic material model into the solid mechanics of the TO of PACMs. If feasible, the study seeks to identify the allowable range of pressure load that can be applied to the system.

SQ2 ***How does integrating geometric nonlinearities and a hyperelastic material model influence the design and behaviour of design-dependent pressure-actuated soft robots in COMSOL?***

This investigation aims to determine the significance of incorporating geometric nonlinearities and a hyperelastic material model. It seeks to assess how the obtained design and behaviour differ from those obtained using TO with a linear elastic material model for PA soft robots.

SQ3 ***What techniques can be employed to improve the range of maximum applied pressure load for the topology optimisation for design-dependent pressure-actuated soft robots, incorporating geometric nonlinearities and a hyperelastic material model in the solid mechanics?***

This subquestion investigates the possibilities of enhancing maximum pressure loads by effectively handling inverted elements. Various techniques exist to address inverted elements and increase the maximum applied pressure loads. This thesis explores the impact of the use of the Wang method, which is explained in chapter 5.

Thesis outline
This thesis is structured as follows: Chapter 2 introduces TO, incorporating a linear elastic material model. It is recommended that readers unfamiliar with TO and linear solid mechanics refer to this chapter. In Chapter 3, the application of Darcy's law to calculate pressure loads for linear TO is explained for PACM. Chapter 4 delves into the nonlinearities that can occur in the solid mechanics of PA soft robots, specifically those considered in this thesis, along with different descriptions of solid mechanics. Chapter 5 presents the results obtained from the investigation of the Wang method. Chapter 6 discusses the results obtained from the TO with geometric nonlinearities and the hyperelastic material model incorporated in the solid mechanics across four examples of PACM. Finally, Chapter 7 provides the discussion, and in Chapter 8, conclusions and recommendations are presented.

2

Linear topology optimisation

TO was initially introduced by Bendsøe and Kikuchi (1988), who developed a homogenisation method utilising the Finite Element Method (FEM). From that point onward, the field of TO experienced significant growth. TO is a technique to determine the optimal distribution of material within a given design domain. The aim of TO is to achieve the desired performance while minimising factors such as weight, material usage, or other specified objectives. By systematically changing the distribution of material, the method finds the configuration with the best objective function that meets the requirements and constraints. TO has applications in various fields, including aerospace, automotive, architecture, and bio-mechanics (Sigmund and Maute 2013). Figure 2.1 shows an example to demonstrate the working principle of TO, where Figure 2.1a shows the original structure before the TO and Figure 2.1b shows the structure obtained after the TO. The objective function of this TO problem is to minimise compliance.

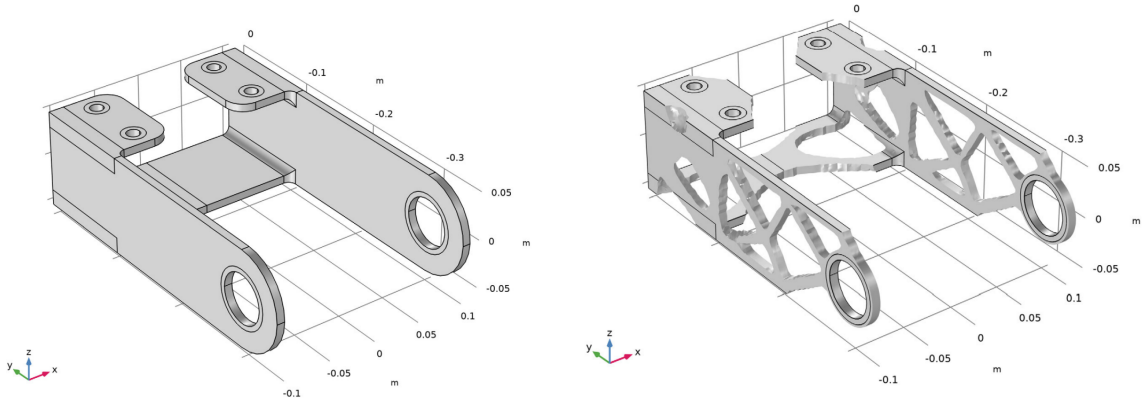

(a) The original structure of the bracket

(b) The TO result of the bracket

Figure 2.1: Comparison of the original structure and the TO result of a bracket to demonstrate the working principle of TO. These brackets are designed by COMSOL (2023).

Numerous TO techniques have been developed, among which Simplified Isotropic Material with Penalisation (SIMP) and the level set method are commonly used. For a comprehensive overview of these obtained methods, the reader is referred to Sigmund and Maute (2013). This overview explains and compares the different TO approaches in different fields.

This chapter is organised as follows: First, in Section 2.1, the steps involved in the TO process are discussed. Next, Section 2.2 details linear solid mechanics, followed by a specific focus on its implementation in COMSOL in Section 2.3. Lastly, Section 2.4 presents the TO problem formulations for structures and CMs.

2.1. Topology optimisation process

The TO process occurs in predefined steps, shown in Figure 2.2. First, the design problem is determined using the FEM, which includes creating the mesh, defining material properties, and specifying boundary conditions, all under the assumption of homogeneous material distribution. Then, the iterative part of the process begins with the design parameterisation, where the design variables are chosen and specified. Then, the Finite Element Analysis (FEA) is conducted, which computes the resulting displacements, strains, and other parameters. After the FEA, the sensitivity analysis is performed. Finally, the objective function and constraints are calculated. If the difference is marginal compared to the last iteration, the mechanism is considered converged, and the iterative process stops, and the TO process is completed (Bendøe et al. 2003). The specific steps of the TO process are explained in detail in Appendix A.

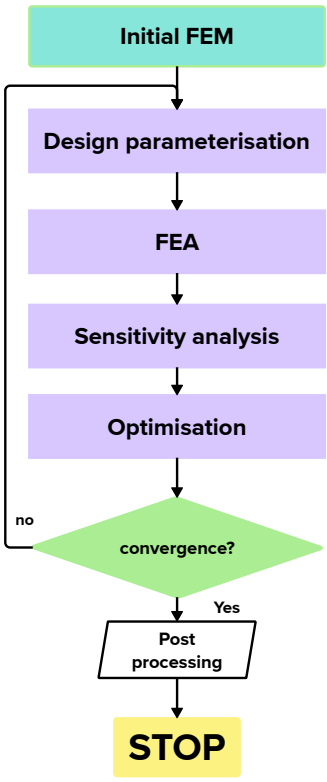

Figure 2.2: The steps of the topology optimisation process

2.2. Linear solid mechanics

The most common material model is the linear elastic material model, based on Hooke's law, shown in Equation 2.1. Hooke's law relates the stress tensor to the strain tensor, where σ, $\mathbf{D}$, and ϵ represent the stress, the elastic modulus, and the strain, respectively. The relation between the stress and the strain is called a constitutive model (Cook et al. 2002). Additionally, in linear systems, the displacement is assumed to be infinitesimal, meaning that the undeformed and the deformed models are almost identical.

$$\sigma = \mathbf{D} : \epsilon \tag{2.1}$$

In linear cases, $\mathbf{D}$ and ϵ remain constant and are expressed by Equation 2.2 and Equation 2.3, respectively (Cook et al. 2002). In Equation 2.2, E and ν represent the Young's modulus and the Poisson ratio, respectively. Additionally, Equation 2.3 introduces $\mathbf{u} = [u \;\; v]$, assuming the plane strain condition where deformation in the out-of-plane direction is considered zero.

It is important to note that for materials that do not exhibit linear elastic behaviour, like hyperelastic materials, the assumption of **D** being constant breaks down. In such cases, more complex constitutive models are required to accurately describe the behaviour of the material (Kim 2015). Nonlinear elastic behaviour is discussed in chapter 4.

$$\mathbf{D} = \begin{bmatrix} \frac{E(\nu-1)}{(2\nu-1)(\nu+1)} & -\frac{E\nu}{(2\nu-1)(\nu+1)} & -\frac{E\nu}{(2\nu-1)(\nu+1)} & 0 & 0 & 0 \\ -\frac{E\nu}{(2\nu-1)(\nu+1)} & \frac{E(\nu-1)}{(2\nu-1)(\nu+1)} & -\frac{E\nu}{(2\nu-1)(\nu+1)} & 0 & 0 & 0 \\ -\frac{E\nu}{(2\nu-1)(\nu+1)} & -\frac{E\nu}{(2\nu-1)(\nu+1)} & \frac{E(\nu-1)}{(2\nu-1)(\nu+1)} & 0 & 0 & 0 \\ 0 & 0 & 0 & \frac{E}{2(\nu+1)} & 0 & 0 \\ 0 & 0 & 0 & 0 & \frac{E}{2(\nu+1)} & 0 \\ 0 & 0 & 0 & 0 & 0 & \frac{E}{2(\nu+1)} \end{bmatrix} \tag{2.2}$$

$$\boldsymbol{\epsilon} = \begin{bmatrix} u_{,X} & \frac{1}{2}(u_{,Y} + v_{,X}) & 0 \\ \frac{1}{2}(u_{,Y} + v_{,X}) & v_{,Y} & 0 \\ 0 & 0 & 0 \end{bmatrix} \tag{2.3}$$

Calculation of the displacements
The principle of virtual work enables the calculation of the displacement field within a model, which is presented in Equation 2.4. Here, δW^{ext} represents the virtual external work, shown in Equation 2.5 and δW^{int} represents the virtual internal work, shown in Equation 2.6. The proof of Equation 2.5 and Equation 2.6 have been omitted. For a more comprehensive and detailed explanation of the principle of work, please refer to Cook et al. (2002).

$$\delta W^{ext} - \delta W^{int} = 0 \tag{2.4}$$

$$\delta W^{ext} = \int_{\Gamma} \mathbf{t} \cdot \delta \mathbf{u} dA + \int_{\Omega} \mathbf{b} \cdot \delta \mathbf{u} dV \tag{2.5}$$

where **t** represents the traction, acting on surface Γ, while **b** denotes the external body forces acting on domain Ω.

$$\delta W^{int} = \int_{\Omega} \delta \boldsymbol{\epsilon}^T \boldsymbol{\sigma} dV \tag{2.6}$$

The discretised form of Equation 2.5, expressed as Equation 2.7, is used to calculate the nodal forces, shown in Equation 2.8. In these two equations, **N** represents the matrix of shape functions, and $\mathbf{u}_e$ represents the nodal displacements vector.

$$W_e^{ext} = \int_{\Gamma} \delta \mathbf{u}_e^T \mathbf{N}^T \mathbf{t} dA + \int_{\Omega} \delta \mathbf{u}_e^T \mathbf{N}^T \mathbf{b} dV = \delta \mathbf{u}_e^T \mathbf{f}_e \tag{2.7}$$

$$\mathbf{f}_e = \int_{\Gamma_e} \mathbf{N}^T \mathbf{t} dA + \int_{\Omega_e} \mathbf{N}^T \mathbf{b} dV \tag{2.8}$$

The element stiffness matrix can be calculated as expressed in Equation 2.9. **B** is constructed using the derivatives of the shape function N with respect to the standard element coordinates $\xi$and η. The nodal forces and the element stiffness matrix can be transformed into the global force vector **f** and global stiffness matrix **K**, respectively. With **f** and **K**, the deformation **u** can be calculated using Equation 2.10.

$$\mathbf{K}_e = E_e \int_{\Omega} \mathbf{B}^T \mathbf{D} \mathbf{B} dV \tag{2.9}$$

$$\mathbf{K}\mathbf{u} = \mathbf{f} \tag{2.10}$$

2.3. Linear solid mechanics in COMSOL

The strain in COMSOL is the linearised Green-Lagrange strain, equivalent to Equation 2.3. Furthermore, the stress is presented with the Second Piola-Kirchhoff stress tensor **S**, which, in the case of the linear elastic material model, is equivalent to Equation 2.1. Consequently, the linear strain energy density function (SEDF) can be calculated, as shown in Equation 2.11. The SEDF is the body's internal energy, stored under deformation.

$$\phi_L = \frac{1}{2}\mathbf{S}_L : \boldsymbol{\epsilon} = \frac{1}{2}\mathbf{D} : \boldsymbol{\epsilon} : \boldsymbol{\epsilon} \tag{2.11}$$

Equation 2.11 is obtained from Gould (2013). Equation 2.11 is widely used and is also the default of COMSOL. However, in chapter 5, the Saint Venant-Kirchhoff material model is utilised under the assumption of small displacements, which can be used to describe a linear elastic material model. The corresponding SEDF for the Saint Venant-Kirchhoff material model is expressed by Equation 2.12 (Gould 2013). Notably, ϕ_L and ϕ_{VK} are equivalent, indicating that the outcome is identical. This equivalence is validated through numerical analysis, as demonstrated by the MATLAB code presented in section E.1.

$$\phi_{VK}(\boldsymbol{\epsilon}) = \frac{1}{2}\lambda(tr(\boldsymbol{\epsilon}))^2 + \mu\boldsymbol{\epsilon} : \boldsymbol{\epsilon} \tag{2.12}$$

The VK in the subscript of ϕ_{VK} means that it is the SEDF of Saint Venant-Kirchhoff. In Equation 2.12, μ and λ present the Lamé parameters, given by Equation 2.13 and Equation 2.14, respectively. μ is called the shear modulus and measures the resistance to changes in shear deformation, while λ is a measure of the resistance to changes in the volume (Kim 2015).

$$\mu = \frac{E}{2(1+\nu)} \tag{2.13}$$

$$\lambda = \frac{E\nu}{(1+\nu)(1-2\nu)} \tag{2.14}$$

Calculating stress can be approached in two equivalent ways. The first method employs Hooke's law, as defined in Equation 2.1. Alternatively, the stress can be determined by differentiating the SEDF with respect to strain, leading to the second Piola-Kirchhoff stress tensor $\mathbf{S}_L$ (Holzapfel 2000). This is expressed in Equation 2.15, obtained from the paper of Holzapfel (2000).

$$\mathbf{S}_L = \underbrace{\mathbf{D} : \boldsymbol{\epsilon}}_{\text{Method 1}} = \underbrace{\frac{\partial \phi_L(\boldsymbol{\epsilon})}{\partial \boldsymbol{\epsilon}}}_{\text{Method 2}} \tag{2.15}$$

2.4. Topology optimisation problem formulation

While several TO categories exist, this thesis specifically focuses on the compliance TO and the TO of CMs. This section presents the problem formulation for compliance TO and CMs in Subsection 2.4.1 and Subsection 2.4.2, respectively.

2.4.1. Structure

The TO formulation for the compliance optimisation is given by Equation 2.16. This TO problem seeks a balance between **K** and the mass to achieve optimal structural performance, aiming to maximise stiffness while minimising mass. The objective function is often expressed by minimising the compliance $\mathbf{C}_{min} = \mathbf{K}^{-1}$, equivalent to minimising the expression $\mathbf{f}^T\mathbf{u} = \mathbf{u}^T\mathbf{K}\mathbf{u}$. Additionally, it is important to note that for design-independent loads, the loads do not depend on the design variables. However, when the loads become design-dependent, they are influenced by the design variable $\boldsymbol{\rho}$, as discussed in Chapter 3. The variables V^* and V represent the permitted and actual volumes of the design, respectively.

$$\left.\begin{aligned} \min_{\rho} \quad & f_0(\mathbf{u},\rho) = \mathbf{u}(\rho)^T\mathbf{K}(\rho)\mathbf{u}(\rho) \\ \text{such that} \quad & \mathbf{K}(\rho)\mathbf{u}(\rho) = \mathbf{f} \\ & \frac{V(\rho)}{V^*} - 1 \leq 0 \\ & \mathbf{0} \leq \rho \leq \mathbf{1} \end{aligned}\right\} \tag{2.16}$$

2.4.2. Compliant Mechanism

Compared to compliance TO, the TO of CMs presents two conflicting objectives: the kinematic and structural objectives. If the focus is solely on the structural objective, the mechanisms may become too stiff, resulting in unwanted stress during deformation. Conversely, if the focus is only on kinematic objectives, the necessary flexibility can be achieved, but this may lead to difficulties in resisting additional loads (Frecker et al. 1997).

Maximising the mutual strain energy (MSE) increases flexibility, while minimising strain energy (SE) maximises stiffness. Note that SE is defined as $SE = \frac{1}{2}\mathbf{C}_{min} = \frac{1}{2}\mathbf{u}^T\mathbf{K}\mathbf{u}$. This thesis employs the multi-criteria formulation developed by Frecker et al. (1997) for the TO formulation of the CMs. The multi-criteria formulation for the TO of CMs is expressed as Equation 2.17. In this equation, $\mathbf{v}$ represents the displacement vector due to the unit dummy load $\mathbf{f}_d$. This unit dummy load is a fictitious or simulated load intentionally applied at a particular location to observe the behaviour of the CMs. It serves to evaluate the resistance and response of the mechanisms under specific conditions. Additionally, the variables V^* and V denote the permitted and actual volumes of the design, respectively. For a more detailed derivation of the problem statement, the reader is referred to Frecker et al. (1997).

$$\left.\begin{aligned} \min_{\rho} \quad & f_0(\mathbf{u},\rho) = -\frac{MSE(\mathbf{u},\mathbf{v},\rho)}{2SE(\mathbf{u},\rho)} = -\frac{\mathbf{v}^T\mathbf{K}\mathbf{u}}{\mathbf{u}^T\mathbf{K}\mathbf{u}} \\ \text{such that} \quad & \mathbf{K}(\rho)\mathbf{u}(\rho) = \mathbf{f} \\ & \mathbf{K}(\rho)\mathbf{v}(\rho) = \mathbf{f}_d \\ & \frac{V(\rho)}{V^*} - 1 \leq 0 \\ & \mathbf{0} \leq \rho \leq \mathbf{1} \end{aligned}\right\} \tag{2.17}$$

3

Linear topology optimisation for design-dependent pressure loads

Identifying the pressure boundary during TO presents a challenge. The existence of intermediate values for design variables in this phase leads to the absence of a clearly defined solid-void boundary, complicating the determination of the pressure boundary.

Kumar, Frouws, et al. (2020) introduced an approach for designing PA structures and CMs, effectively addressing challenges posed by pressure loads. They applied the mathematical framework of Darcy's law to calculate pressure loads while treating all elements as porous media. These obtained pressure loads depend on the design during the TO, a condition not addressed in chapter 2. This approach is called the Darcy method. It is important to note that this chapter is based on a linear TO and is based on the paper by Kumar, Frouws, et al. (2020).

This chapter is structured as follows: The Darcy method is explained in Section 3.1. Second, Section 3.2 provides the TO formulation for a PA structure and a PACM. Additionally, to validate the implementation of the Darcy method in COMSOL, an investigation has been conducted in Appendix B for two different COMSOL models.

3.1. Modelling design-dependent pressure loads

Darcy's law describes the ability of a fluid to flow through a porous media and can be expressed using Equation 3.1. The flow coefficient K defines the ability of the fluid to permeate a porous medium. Solid elements ($\rho_e = 1$) offer high resistance to flow, while void elements ($\rho_e = 0$) provide low resistance to fluid flow. Table 3.1 provides the meaning and the units of the parameters used in Equation 3.1.

$$\mathbf{q} = -\frac{\kappa}{\mu_f}\nabla p = -K\nabla p(\mathbf{x}) \tag{3.1}$$

Parameter	Notation	unit
Darcy flux	$\mathbf{q}$	ms^{-1}
Pressure load gradient	∇p	Nm^{-3}
Permeability	κ	m^2
Fluid viscosity	μ_f	Pa s
Flow coefficient	K	$\mathrm{m}^4\mathrm{N}^{-1}\mathrm{s}^{-1}$

Table 3.1: The meaning, notation and the units for the parameters used in Equation 3.1.

A Heaviside function is used to distinguish between void and solid elements, ensuring a differentiable and smooth transition. Equation 3.2 shows the equation for the flow coefficient K of element e, where K_v and K_s represent the flow coefficient of the void and solid elements, respectively. The desired ratio is $\frac{K_s}{K_v} = 10^{-7}$, as explained by Kumar and Langelaar (2021).

$$K(\rho_e) = K_v - (K_v - K_s)\frac{\tanh(\beta_k\eta_k) + \tanh(\beta_k(\rho_e - \eta_k))}{\tanh(\beta_k\eta_k + \tanh(\beta_k(1 - \eta_k))} \tag{3.2}$$

The Heaviside function is visually represented for various values of ρ_0 and β_1 in Figure 3.1. Essentially, the Heaviside function takes on the value 0 when $\rho_e < \eta_k$ and 1 when $\rho_e > \eta_k$. The steepness of the transition from 0 to 1 is determined by the parameter β_k. Figure 3.1 aims to provide insights into the characteristics of the Heaviside function.

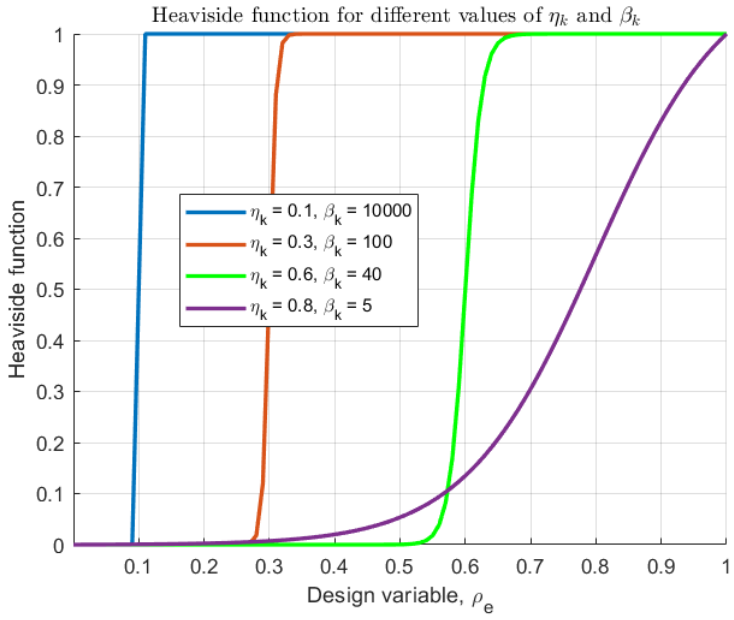

Figure 3.1: The Heaviside function for several values of η_k and β_k

The drawback of using Equation 3.1 is that it gradually decreases the pressure load over the area, leading to nodal forces within the material. However, nodal forces can only exist at the associated pressure boundaries. To solve this issue, a drainage term, expressed in Equation 3.3, is added to induce the pressure load to drop after the pressure boundary. This drainage term absorbs the flow after the pressure boundary, preventing it from entering the material. The effect of the drainage term is illustrated in Figure 3.3, with the corresponding schematic visualisation of the problem and its associated boundary conditions shown in Figure 3.2.

$$Q_{drain} = -D_c(\rho_e)(\mathbf{p} - \mathrm{p}_{out}) \tag{3.3}$$

where D_c and p_{out} represent the drainage coefficient and the external pressure load, respectively. The drainage coefficient D_c, as expressed in Equation 3.4, utilises a Heaviside function to achieve the desired pressure load drop for an element with $\rho_e = 1$. Additionally, d_s regulates the thickness of the pressure-penetration layer. Table 3.2 provides the meaning and units of the parameters presented in Equation 3.4.

$$D_c(\rho_e) = \underbrace{\left(\frac{ln(r)}{\Delta s}\right)^2 K_s}_{d_s} \frac{\tanh(\beta_h\eta_h + \tanh(\beta_h(\rho_e - \eta_h))}{\tanh(\beta_h\eta_h + \tanh(\beta_h(1 - \eta_h))} \tag{3.4}$$

Parameter	Notation	unit
Drainage coefficient	D_c	$m^2N^{-1}s^{-1}$
Ratio of input pressure load to pressure load at depth Δs	r	-
Penetration depth of the pressure load	Δs	m

Table 3.2: The meaning, notation and the units for the parameters used in Equation 3.4.

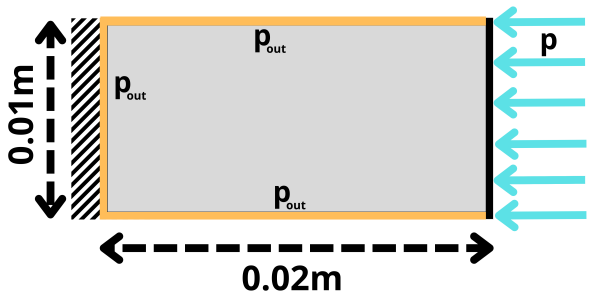

Figure 3.2: The schematic visualisation and the associated boundary condition of the beam corresponding to Figure 3.3

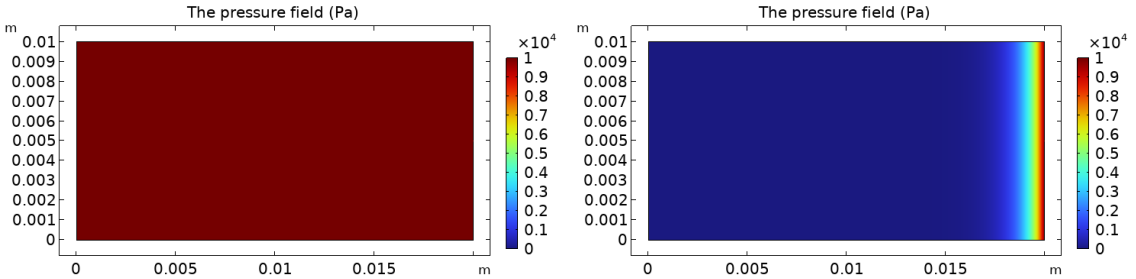

(a) Without a Drainage term

(b) With a Drainage term

Figure 3.3: The comparison of the pressure field obtained from the Darcy method without (a) and with (b) a Drainage term. The applied pressure load is 1×10^4 Pa

Calculation of the nodal forces

The mass conservation equation is used to determine the net flow of the system, as expressed in Equation 3.5. Equation 3.6 represents the weak formulation of the mass conservation equation, which is obtained by applying the Galerkin method to Equation 3.5. Table 3.3 provides the meaning and the units of the parameters of Equation 3.6.

$$\nabla \cdot \mathbf{q} - Q_{drain} = 0 \tag{3.5}$$

$$\underbrace{\int_{\Omega_e} (K\, \mathbf{B}_p^T \mathbf{B}_p + D_c\, \mathbf{N}_p^T \mathbf{N}_p)\, d\Omega_e}_{\mathbf{A}_e}\ \mathbf{p}_e = \underbrace{\int_{\Omega_e} D\, \mathbf{N}_p^T \mathrm{p}_{out} d\Omega_e - \int_{\Gamma_e} \mathbf{N}_p^T \mathbf{q}_\Gamma \cdot \mathbf{n}_e\, d\Gamma_e}_{\mathbf{f}_{flow,e}} \tag{3.6}$$

It is assumed that p_{out} and $\mathbf{q}_\Gamma$ are both zero, leading to $\mathbf{f}_{flow,e} = 0$. The assumption of $\mathbf{q}_\Gamma = 0$ maintains a steady-state condition. As a result, the pressure field can be determined by solving the global form of Equation 3.6, as depicted in Equation 3.7. This global form results from the assembly of Equation 3.6.

$$\mathbf{A}\mathbf{p} = \mathbf{f}_{flow} = 0 \tag{3.7}$$

In Equation 3.7, $\mathbf{A}$ and $\mathbf{f}_{flow}$ denote the global flow matrix and the global loading vector, respectively. The nodal forces for each element can now be calculated by combining the obtained pressure load from Equation 3.7, the force equilibrium $\mathbf{b}dV = -\nabla p(\mathbf{x})dV$, and Equation 2.8. The equation representing the nodal forces is expressed in Equation 3.8, where $\mathbf{H}_e$ is the conversion matrix for the elements. The stiffness matrix $\mathbf{K}$ and the displacement can be calculated similarly to Equation 2.9 and Equation 2.10, respectively.

$$\mathbf{f}_e = -\int_{\Omega_e} \mathbf{N}^T \nabla p(\mathbf{x}) dV = -\mathbf{p}_e \underbrace{\int_{\Omega_e} \mathbf{N}\mathbf{B}_p d\Omega_e}_{\mathbf{H}_e} \tag{3.8}$$

Parameter	Notation	unit
Vector of Shape functions	$\mathbf{N}_p$	-
Matrix of spatial derivatives	$\mathbf{B}_p = \nabla \mathbf{N}_p$	m^{-1}
Domain of the element	Ω_e	m^3
Boundary of the element	Γ_e	m^2
Prescribed Darcy flux at the boundary	$\mathbf{q}_\Gamma$	m s^{-1}
Boundary normal vector	$\mathbf{n}$	-
Pressure load of the element	$\mathbf{p}_e$	Pa
Flow matrix of the element	$\mathbf{A}_e$	$m^5 N^{-1} s^{-1}$
Loading vector of the element	$\mathbf{f}_{flow,e}$	m^3 s^{-1}

Table 3.3: The meaning, notation and the units for the parameters used in Equation 3.6.

3.2. Topology optimisation formulation of pressure-actuated compliant mechanisms

This section provides the TO formulation of PACMs. The TO formulation of the PA compliance optimisation problem is omitted since it will not be used in this thesis. The reader is referred to Kumar, Frouws, et al. (2020) for the TO formulation of the PA compliance optimisation problem.

Which TO approach is best suited for PACMs remains uncertain. Therefore, the multi-criteria formulation is implemented, as it proved effective in the work by Kumar, Frouws, et al. (2020) and Kumar and Langelaar (2022). The problem formulation for PACMs differs from that of CMs, primarily due to the incorporation of the Darcy method. The Darcy method introduces additional constraints to the problem formulation, as given in Equation 3.9. Here, $\mathbf{A}$, $\mathbf{p}$, and $\mathbf{H}$ represent the global flow matrix, the global pressure load vector, and the global conversion matrix, respectively. It should be noted that $\mathbf{H}$ is the assembly of $\mathbf{H}_e$ and is independent of the design variables. For readers interested in the sensitivity analysis of PACMs, comprehensive derivations can be found in Kumar, Frouws, et al. (2020).

$$\left.\begin{aligned} \min_{\rho} \quad & f_0(\mathbf{u}, \boldsymbol{\rho}) = -\frac{MSE(\mathbf{u}, \mathbf{v}, \boldsymbol{\rho})}{2SE(\mathbf{u}, \boldsymbol{\rho})} = -\frac{\mathbf{v}(\boldsymbol{\rho})^T \mathbf{K}(\boldsymbol{\rho}) \mathbf{u}(\boldsymbol{\rho})}{\mathbf{u}(\boldsymbol{\rho})^T \mathbf{K}(\boldsymbol{\rho}) \mathbf{u}(\boldsymbol{\rho})} \\ \text{such that} \quad & \mathbf{A}\mathbf{p}(\boldsymbol{\rho}) = 0 \\ & \mathbf{K}(\boldsymbol{\rho})\mathbf{u}(\boldsymbol{\rho}) = \mathbf{f}(\boldsymbol{\rho}) = -\mathbf{H}\mathbf{p}(\boldsymbol{\rho}) \\ & \mathbf{K}(\boldsymbol{\rho})\mathbf{v}(\boldsymbol{\rho}) = \mathbf{f}_d \\ & \frac{V(\boldsymbol{\rho})}{V^*} - 1 \leq 0 \\ & \mathbf{0} \leq \boldsymbol{\rho} \leq \mathbf{1} \end{aligned}\right\} \tag{3.9}$$

4

Nonlinear topology optimisation for design-dependent pressure load

Many phenomena encountered in our daily lives exhibits nonlinear behaviour, such as inflating a balloon or objects undergoing plastic deformation. Considering the impact of these nonlinearities when designing and analysing mechanisms is crucial. However, this can be challenging, and explaining nonlinearities requires understanding linear behaviour first. A system exhibits linear behaviour when it follows the principles of superposition and homogeneity. Superposition means that the combined response to multiple inputs equals the sum of their individual responses, while homogeneity states that scaling the input results in proportional output scaling.

The paper by Kumar and Langelaar (2022) concludes that incorporating all nonlinearities in solid mechanics is crucial when designing PACMs. This necessity is emphasised by their findings, where a linear system, though offering a good approximation for the displacement of bodies like buildings, proves insufficient to describe the behaviour of PACMs accurately. In their study, the authors conducted a linear TO followed by a nonlinear analysis of the designs obtained from the TO. The results highlighted significant differences due to nonlinearities in their system, reinforcing the importance of considering all nonlinear aspects in PACM design.

In this chapter, Section 4.1 delves into the nonlinearities that can occur in the solid mechanics of soft robots. Additionally, Section 4.2 introduces nonlinear solid mechanics, while Section 4.3 explores various formulations of the solid mechanics. Finally, Section 4.4 discusses nonlinear solvers.

4.1. Nonlinearities of solid mechanics

As introduced, the TO of PACMs involves addressing four types of nonlinearities: geometric, material, boundary, and force nonlinearities. This thesis concentrates explicitly on integrating geometric nonlinearities (Subsection 4.1.1) and hyperelastic material models (Subsection 4.1.2) into the solid mechanics of the TO process. Furthermore, force nonlinearities (Subsection 4.1.3) are introduced in the analysis of the results obtained from the TO, though not incorporated into the solid mechanics of the TO. It is important to note that this study does not incorporate both force and boundary nonlinearities in the TO, as it is beyond the scope of the present research.

4.1.1. Geometric nonlinearity

Geometric nonlinearities occur when the relationship between the strain and the displacement is nonlinear, resulting from large displacements. In such cases, a linear relationship cannot accurately describe the behaviour because of the large displacements involved. The most common strain formulation is the Green-Lagrange strain tensor $\mathbf{E}_{GL}$, which is expressed in Equation 4.1. Note that the nonlinear part may be neglected when the displacement is significantly small such that $\frac{\partial \mathbf{u}}{\partial \mathbf{X}} \ll 1$, resulting in the linearised Green-Lagrange strain, as shown in Equation 2.3.

$$
\begin{aligned}
\mathbf{E}_{GL} &= \frac{1}{2}(\mathbf{F}^T\mathbf{F} - \mathbf{I}) \\
&= \frac{1}{2}(\mathbf{C} - \mathbf{I}) \\
&= \frac{1}{2}(\underbrace{\frac{\partial \mathbf{u}}{\partial \mathbf{X}} + \frac{\partial \mathbf{u}^T}{\partial \mathbf{X}}}_{\text{Linear}} + \underbrace{\frac{\partial \mathbf{u}^T}{\partial \mathbf{X}}\frac{\partial \mathbf{u}}{\partial \mathbf{X}}}_{\text{Nonlinear}}) \\
&= \begin{bmatrix} \frac{1}{2}(2u_{,X} + (u_{,X}^2 + v_{,X}^2)) & \frac{1}{2}(u_{,Y} + v_{,X} + (u_{,X}u_{,Y} + v_{,X}v_{,Y})) & 0 \\ \frac{1}{2}(u_{,Y} + v_{,X} + (u_{,X}u_{,Y} + v_{,X}v_{,Y})) & \frac{1}{2}(2v_{,Y} + (u_{,Y}^2 + v_{,Y}^2)) & 0 \\ 0 & 0 & 0 \end{bmatrix}
\end{aligned}
\tag{4.1}
$$

In Equation 4.1, $\mathbf{F}$ represents the deformation gradient and $\mathbf{C}$ denotes the right Cauchy-Green deformation tensor, which is calculated as $\mathbf{C} = \mathbf{F}^T\mathbf{F}$. $\mathbf{F}$ is the primary measure of deformation and can be defined as Equation 4.2, where $\nabla\mathbf{u}$ represents the gradient of the displacement field $\mathbf{u}$.

$$
\mathbf{F} = \mathbf{I} + \nabla\mathbf{u} \tag{4.2}
$$

4.1.2. Hyperelastic material model

Material nonlinearities arise when a nonlinear relationship exists between the strain and stress. In Section 2.2, the constitutive model for a linear elastic material is shown in Equation 2.1. This relation remains linear as long as $\mathbf{D}$ is constant; however, this condition does not hold for hyperelastic materials.

This thesis focuses solely on the hyperelastic material model due to its significant importance in designing PA soft robots. Various nonlinear material models, such as hyperelasticity, viscoelasticity, and elastoplasticity, exist to describe the nonlinear behaviour of materials. Among these models, hyperelastic materials stand out as they can undergo large displacements without experiencing failure. This characteristic makes them ideal for PA soft robots, where achieving large displacements is often necessary for desired movements and functionalities (Caasenbrood et al. 2020).

Hyperelastic materials can undergo large deformations while returning to their original shape when the load is removed. These materials are typically used to model rubber-like or soft tissues. One characteristic of hyperelastic materials is their path-independence. This means that the energy required to deform a hyperelastic material is solely determined by the final state of displacement and is not influenced by how the material was loaded, up to a certain extent (Belytschko et al. 2014). This behaviour is because the Second Piola-Kirchhoff stress $\mathbf{S}$ is equivalent to the derivative of the SEDF ϕ with respect to the strain, as expressed in Equation 4.3 (Kim 2015). The subscript NL in $\mathbf{S}_{NL}$ denotes the nonlinear Second Piola-Kirchhoff stress.

$$
\mathbf{S}_{NL} = \frac{\partial \phi(\mathbf{E}_{GL})}{\partial \mathbf{E}_{GL}} = 2\frac{\partial \phi(\mathbf{C})}{\partial \mathbf{C}} \tag{4.3}
$$

This formula is obtained from Holzapfel (2000). This thesis implements the Neo-Hookean material model, chosen from a range of available hyperelastic material models, including the Saint-Venant-Kirchhoff, Mooney-Rivlin, and Yeoh models. The selection of the Neo-Hookean material model is supported by its demonstrated effectiveness in the literature (Conlan-Smith et al. 2018; Kumar and Langelaar 2022; Dou et al. 2023)

Neo-Hookean material model

While the Neo-Hookean material model has various formulations for the SEDF, as discussed by Klarbring et al. (2013), it is crucial to note that COMSOL utilises a specific SEDF, as expressed in Equation 4.4.

$$
\phi_{HE} = \frac{1}{2}\mu(-3 + I_1) - \mu\ln(\sqrt{I_3}) + \frac{1}{2}\lambda\ln(\sqrt{I_3})^2 \tag{4.4}
$$

In Equation 4.4, I_1 and I_3 represent the first and third invariants of $\mathbf{C}$, respectively. I_1 is the trace of $\mathbf{C}$ and can be calculated as shown in Equation 4.5, where λ_1 and λ_3 are two out of the three eigenvalues of $\mathbf{C}$. I_3 is the determinant of $\mathbf{C}$ and can be expressed as Equation 4.6. Note that I_3 will be equal to 1 if the material is incompressible (Kim 2015).

$$I_1 = \text{tr}(\mathbf{C}) = \lambda_1^2 + \lambda_2^2 + \lambda_3^2 \tag{4.5}$$

$$I_3 = \det(\mathbf{C}) = \lambda_1^2 \lambda_2^2 \lambda_3^2 \tag{4.6}$$

Modelling of a Neo-Hookean material model

When modelling a compressed beam in COMSOL, notable differences arise between using a linear, geometric nonlinear, and Neo-Hookean material model. A schematic visualisation of the beam and the corresponding boundary conditions are presented in Figure 4.1. The results for various values of the applied load using a linear material model are depicted in Figure 4.2. In contrast, the results of a Neo-Hookean material model are illustrated in Figure 4.3. The results of the beam incorporating the geometric nonlinear material model are omitted for comparison in the figure. The reason for this is that the maximum value of the applied load subjected to the beam is significantly smaller than that for the Neo-Hookean and linear elastic material models.

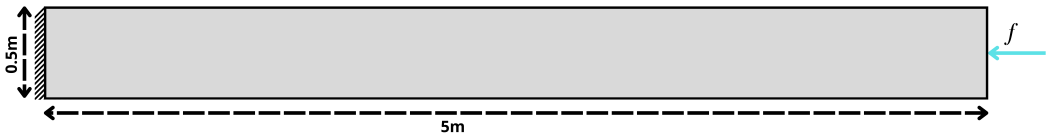

Figure 4.1: The schematic visualisation of a beam under compression

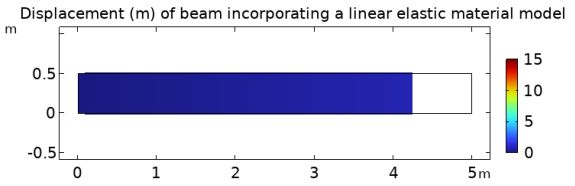

(a) $f = 5 \times 10^8$ N

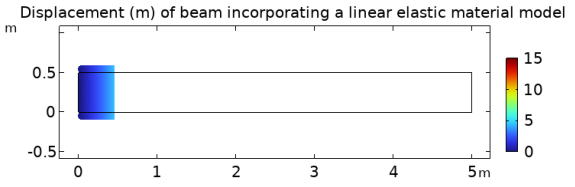

(b) $f = 3 \times 10^9$ N

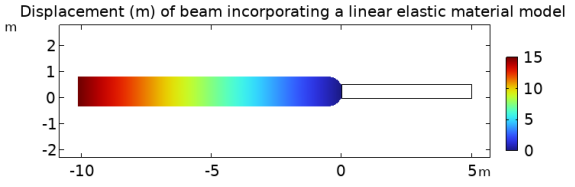

(c) $f = 1 \times 10^{10}$ N

Figure 4.2: The displacement of a beam under various applied loads, simulated using a linear elastic material model in the solid mechanics

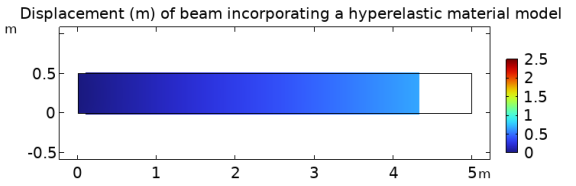

(a) $f = 5 \times 10^8$ N

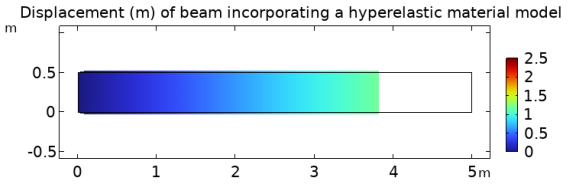

(b) $f = 1 \times 10^9$ N

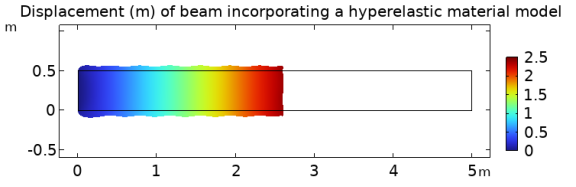

(c) $f = 3 \times 10^9$ N

Figure 4.3: The displacement of a beam under various applied loads, simulated using a Neo-Hookean material model in the solid mechanics

If the applied load on the beam, incorporating a linear material model, is significantly large. In that case, the compressed beam will eventually transition to the opposite side, as illustrated in the shift from Figure 4.2b to Figure 4.2c. This figure shows that the beam has flipped to the other side of the fixed boundary. In contrast, this flipping behaviour is absent when incorporating a Neo-Hookean material model. In this case, the maximum applied force under compression is 3×10^9N, as shown in Figure 4.3c. The analysis will fail if this value is exceeded since a solution can not be found. In physical reality, the flipping behaviour observed in the linear elastic material model is not feasible. As a result, the Neo-Hookean material model better aligns with the actual behaviour of the beam, where such flipping is absent.

The maximum applied force achievable for the beam, incorporating geometric nonlinearities in the solid mechanics, is 5×10^8N. Exceeding this limit results in distorted elements, leading to a failing analysis. Due to the distorted elements, the maximum applied force is significantly lower compared to the linear and Neo-Hookean material models. It is worth noting that geometric nonlinearities are inherently incorporated into the solid mechanics when implementing the Neo-Hookean material model in COMSOL. The introduction of the Neo-Hookean material model alongside geometric nonlinearities notably expands the range of applied load values. Consequently, it can be concluded that incorporating a Neo-Hookean material model increases stability when the structure undergoes large displacements.

Figure 4.4 illustrates a force-displacement curve for incorporating a linear elastic, geometric nonlinear, and Neo-Hookean material model for a beam under compression and tension. When incorporating a geometric nonlinear material model, the limitations of the model can be observed immediately. Specifically under compression, the model with geometric nonlinearities cannot handle large forces compared to the model with the Neo-Hookean material model. Moreover, significant deformations may occur when considering a beam under tension with a Neo-Hookean material model. In contrast, the stiffness becomes significantly large under compression, preventing the flipping behaviour observed in the linear elastic material model.

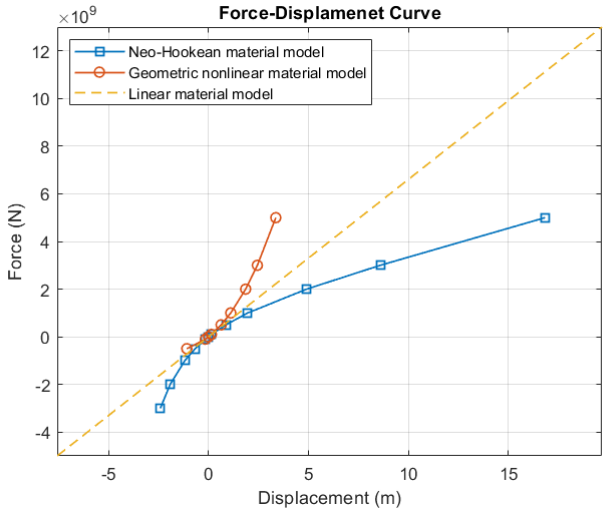

Figure 4.4: The force-displacement curve for a cantilever beam with a linear (dotted line), geometric nonlinear (circles), and Neo-Hookean material (squares) model under different applied force values.

4.1.3. Force nonlinearities

Force nonlinearities occur when the relationship between stress and applied force becomes nonlinear, typically when the applied load or pressure depends on the deformation. These loads change in magnitude, direction, and location as the structure or mechanism undergoes displacement (Kim 2015). Loads that depend on the displacement are called follower forces. Figure 4.5 is an example to illustrate the force nonlinearities.

Force nonlinearities are commonly present when modelling PA soft robots since large displacements are inevitable. Nevertheless, introducing force nonlinearities into TO can pose challenges for sensitivity analysis and modelling. Addressing these challenges is crucial for the successful implementation of the force nonlinearities.

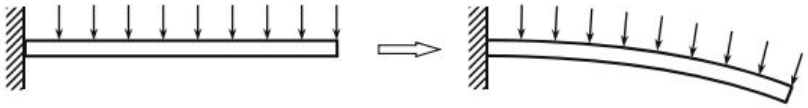

Figure 4.5: The left figure illustrates the initial state of a cantilever beam, while the right figure depicts the beam subjected to a distributed load, highlighting the change in the direction of the follower forces. This figure is obtained from Kim (2015)

4.2. Nonlinear solid mechanics formulations

In nonlinear solid mechanics, the Green-Lagrange strain and Second Piola-Kirchhoff stress represent the strain and stress, respectively. Expressions for these quantities, along with the SEDF for a Neo-Hookean material model, can be found in Equation 4.1, Equation 4.4, and Equation 5.1, respectively. This section presents the derivation of the nonlinear stiffness matrix, based on Holzapfel (2000). For a more comprehensive explanation, readers are encouraged to refer to Holzapfel (2000).

Hyperelastic materials are conservative, meaning the minimum potential energy principle can be applied. The total potential energy can be calculated as the sum of the external potential energy, Π^{ext}, and the internal potential energy Π^{int}, as expressed in Equation 4.7. It is important to note that the loads are not dependent on the displacement. In Equation 4.7, Ω_0 is the surface area of the initial configuration of the body, and $\Omega_{0,\sigma}$ is the boundary surface where the traction vector $\mathbf{t}$ is prescribed.

$$\Pi(\mathbf{u}) = \Pi^{int}(\mathbf{u}) + \Pi^{ext}(\mathbf{u}) = \underbrace{\int_{\Omega_0} \phi(\mathbf{F}(\mathbf{u}))dV}_{\Pi^{int}} \underbrace{- \int_{\Omega_0} \mathbf{b}\cdot\mathbf{u}dV - \int_{\partial\Omega_{0,\sigma}} \mathbf{t}\cdot\mathbf{u}dS}_{\Pi^{ext}} \tag{4.7}$$

The principle of stationary potential energy, represented as $\delta\Pi(\mathbf{u}, \delta\mathbf{u})$, states that when potential energy reaches a stationary point, the change in potential energy $\delta\Pi(\mathbf{u}, \delta\mathbf{u})$ is zero. $\delta\Pi(\mathbf{u}, \delta\mathbf{u})$ can be expressed as Equation 4.8 (proof is omitted), where $\frac{\partial\phi}{\partial F} = \frac{\partial\phi}{\partial\nabla\mathbf{u}}\frac{\partial\nabla\mathbf{u}}{\partial F} = \frac{\partial\phi}{\partial\nabla\mathbf{u}}$.

$$\begin{aligned}
\delta\Pi(\mathbf{u}, \delta\mathbf{u}) &= \int_{\Omega_0} \frac{\partial\phi(\mathbf{F}(\mathbf{u}))}{\partial F} : \nabla\delta\mathbf{u}dV - \int_{\Omega_0} \mathbf{b}\cdot\delta\mathbf{u}dV - \int_{\partial\Omega_{0,\sigma}} \mathbf{t}\cdot\partial\mathbf{u}dS \\
&= \underbrace{\int_{\Omega_0} \frac{\partial\phi(\mathbf{F}(\mathbf{u}))}{\partial\nabla\mathbf{u}} : \nabla\delta\mathbf{u}dV}_{\delta\Pi^{int}} \underbrace{- \int_{\Omega_0} \mathbf{b}\cdot\delta\mathbf{u}dV - \int_{\partial\Omega_{0,\sigma}} \mathbf{t}\cdot\partial\mathbf{u}dS}_{\delta\Pi^{ext}} \\
&= 0
\end{aligned} \tag{4.8}$$

It is important to highlight that $\delta\Pi^{int} = \delta W^{int}$ and $\delta\Pi^{ext} = -\delta W^{ext}$. Consequently, the internal and external forces, denoted by f^{int} and f^{ext} respectively, can be determined using the relationship $\delta W = f\delta\mathbf{u}$, as presented in Equation 4.9. This equation represents the principle of virtual work, demonstrating the interchangeability of the principle of virtual work and the principle of minimum potential energy for hyperelastic materials. Finally, the stiffness can be calculated as depicted in Equation 4.10.

$$\delta\Pi(\mathbf{u}, \delta\mathbf{u}) = 0 = \delta W^{int} - \delta W^{ext} = (\mathbf{f}^{int} - \mathbf{f}^{ext})\delta u \tag{4.9}$$

$$\mathbf{K}(\delta\mathbf{u}) = \frac{\partial\mathbf{r}}{\partial\mathbf{u}} = \frac{\partial(\mathbf{f}^{int} - \mathbf{f}^{ext})}{\partial\mathbf{u}} \tag{4.10}$$

4.3. Solid mechanics formulation

The Lagrangian and Eulerian formulations are two widely used approaches to describe the governing equations that describe the behaviour of physical systems. The choice of the formulation is essential for accurately simulating the nonlinear analysis for large displacement (Belytschko et al. 2014). This section discusses four different formulations: the Total Lagrangian, the Updated Lagrangian, the Eulerian, and the Arbitrary Lagrangian-Eulerian (ALE) formulation. It is important to note that COMSOL uses the Total Lagrangian formulation by default.

In the Total Lagrangian formulation, the reference (undeformed) configuration remains fixed throughout the analysis. The displacement is described with respect to the initial configuration, and material particles are tracked in the reference configuration. In the Updated Lagrangian formulation, the reference configuration is initially fixed but is updated as the material deforms. Deformation is described with respect to the current (deformed) configuration, and material particles are tracked in the reference configuration as they move through space.

In the Eulerian formulation, the reference configuration remains fixed, and the observer is stationary in space. Deformation is described in a fixed coordinate system, with the observer tracking how material properties change at fixed spatial locations.

Figure 4.6 illustrates the distinctions between the obtained meshes from the Lagrangian and Eulerian formulations. A drawback of the Lagrangian formulation is that it often proves ineffective in managing problems with large deformation, as it can lead to element distortion, compromising accuracy and stability. Consequently, the Eulerian formulation is often preferred in such scenarios, where elements do not change shape since a fixed mesh is maintained. However, this requires a larger mesh to capture significant displacements (Belytschko et al. 2014).

An advantage of the Lagrangian formulation is that the material coordinates align with the mesh nodes, ensuring that boundary nodes always remain on the boundary. This alignment, however, is not applicable to the Eulerian formulation, leading to difficulties in addressing moving boundaries and interfaces (Belytschko et al. 2014).

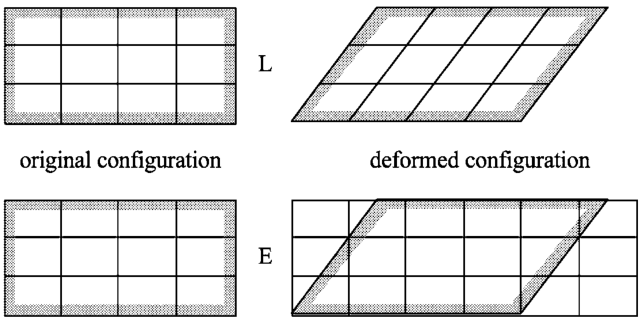

Figure 4.6: The difference between the obtained deformed mesh using a Total Lagrangian or Eulerian formulation. The upper meshes present the Total Lagrangian formulation (L), while the bottom meshes present the Eulerian formulation (E). This figure is obtained from Belytschko et al. (2014).

The fourth formulation is the ALE formulation, combining advantages from the Lagrangian and Eulerian formulations. The reference configuration is initially fixed in the ALE formulation but can be updated as the material deforms. The deformation and the material particles are described with the current (deformed) configuration (Stoker 1999).

Figure 4.7 illustrates the working principles of both the ALE and the Updated Lagrangian formulations. Figure 4.7a presents the initial setup of the analysis. Figure 4.7b shows the solution of the mesh when incorporating the Updated Lagrangian formulation. It is evident from this figure that, in the case of the Updated Lagrangian formulation, the mesh results in a distorted element mesh. Figure 4.7c demonstrates the results of incorporating the ALE formulation, where mesh distortion is effectively prevented.

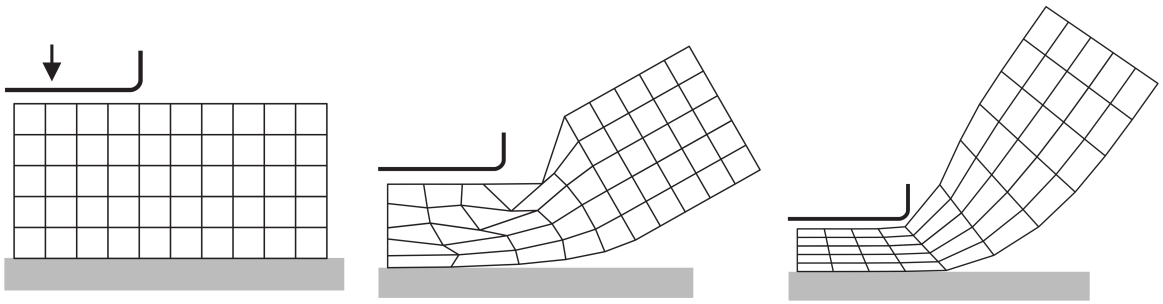

(a) The initial setup **(b)** The updated Lagrangian formulation **(c)** The ALE formulation

Figure 4.7: The difference between the deformed meshes obtained using the Updated Lagrangian and ALE formulations. This figure is obtained from Stoker (1999).

4.4. Nonlinear solvers

In many cases, finding exact solutions for nonlinear equations can be a challenging task. As a result, researchers have developed various solution methods, with the Newton-Raphson method being the most commonly used for solving nonlinear equations. Notably, the Newton-Raphson method is used by default in COMSOL, and a brief introduction to this method is provided here. For a comprehensive explanation of the Newton-Raphson method, readers are referred to the book of Belytschko et al. (2014), which also serves as the basis for this section.

The Newton-Raphson method is a numerical technique for finding the solution of a function. The method operates iteratively, beginning with an initial guess (x_0). At this point, the value $f(x_0)$ and the derivative $f'(x_0)$ of the function are evaluated. The subsequent step involves updating the initial guess using the formula $x_1 = x_0 - \frac{f(x_0)}{f'(x_0)}$. This process iterates until the difference between consecutive guesses is smaller than a specified tolerance.

Essentially, the Newton-Raphson method employs linear approximations of the function to guide the search for the solution, enhancing accuracy with each iteration. The formula implicitly incorporates a step size adjustment, where the ratio $\frac{f(x_0)}{f'(x_0)}$ determines the magnitude of the step size applied to the initial guess. This step size is crucial in guiding the search for the solution.

Despite its effectiveness, the Newton-Raphson method has some disadvantages. It can be sensitive to the initial guess, converging slowly or failing to converge if the guess is far from the actual solution. Furthermore, there exists a risk of convergence to local minima or maxima rather than the desired solution. The performance of the method is also influenced by the smoothness of the function, and noisy or irregular functions may lead to oscillations or divergence. Additionally, carefully considering the step size is essential, as excessively large or small steps can impact convergence.

In response to the limitations of the Newton-Raphson method, various optimisation techniques have been developed to enhance convergence and robustness. Notable among these are the Quasi-Newton Raphson and Double Dogleg methods (Nocedal et al. 1999). These methods are also based on iterative processes for finding the solution of a function but differentiate themselves through unique approaches in updating the guesses.

While the Quasi-Newton Raphson and Double Dogleg methods offer valuable advantages, it is essential to acknowledge their inherent limitations. In theory, the Double Dogleg method is expected to outperform the Newton-Raphson method, but this superiority is not consistently observed across all cases within COMSOL. In such instances, the Newton-Raphson method proves to be an effective alternative. Fine-tuning the parameters within the Double Dogleg method has the potential to enhance its performance and address the observed inconsistencies in different scenarios. However, this involves a cumbersome process and relies heavily on user skills. Choosing an optimisation algorithm requires a careful balance between the advantages and disadvantages inherent in each method.

5

Wang Method

Large displacements in mechanical systems can significantly alter the geometry of elements. As a result, the void elements may experience excessive distortion during the TO process. When elements in a finite element model experience excessive distortion, it can affect the convergence behaviour of the Newton-Raphson iterations. Consequently, this leads to numerical instabilities in the Newton-Raphson iterations (Wang, Lazarov, Sigmund, and Jensen 2014). Several approaches have been introduced to deal with these numerical instabilities. However, these approaches have incorporated the St. Venant-Kirchhoff material model. Unfortunately, this material model does not yield physically correct results for large displacements, especially in compression, as discussed in the paper of Klarbring et al. (2013).

Wang, Lazarov, Sigmund, and Jensen (2014) developed a method to address the numerical instabilities caused by the inversion of elements. The scheme operates by modelling void regions using linear theory and solid regions using nonlinear theory. An advantage of this method is that it works effectively with various hyperelastic material models.

In the FEA, the solid mechanics of the elements are interpolated between large and small displacement formulations. This technique allows for the consideration of void regions when large displacements occur. A linear model is applied explicitly to these regions to address numerical instabilities caused by the void regions. This means that the material behaviour in the solid and void regions is treated independently using different material models. This separation is crucial for achieving numerical stability since it ensures that the material properties in void regions exert a controlled and predictable influence on the solution due to the linear behaviour. This will contribute to a reliable and consistent solution when significant geometric changes occur (Wang, Lazarov, Sigmund, and Jensen 2014).

In this thesis, the interpolation method is referred to as the Wang method, where strain, stress, and SEDF are interpolated. It is important to note that in COMSOL, geometric nonlinearities are inherently considered in the solid mechanics when incorporating a Neo-Hookean material model. Therefore, when discussing the integration of the Neo-Hookean material model, geometric nonlinearities are already taken into account in the solid mechanics.

The aim of this chapter is to address the third subquestion mentioned in the introduction by investigating the potential extension of the range of maximum allowable pressure load applied to various structures and mechanisms. Furthermore, the correct method for interpolating kinematic parameters remains unclear based on the paper by Wang, Lazarov, Sigmund, and Jensen (2014). Therefore, it is necessary to examine the appropriate interpolation method.

This chapter is structured as follows: First, in Section 5.1, the kinematic parameters of the solid mechanics are interpolated. Second, Section 5.2 presents a case study where the Wang method is applied to a C-beam, the TO of a cantilever beam, and the TO of an inverter.

5.1. Interpolation of the kinematic parameters

The Wang method relies on interpolating between linear and nonlinear theories, necessitating the interpolation of three essential kinematic parameters: the SEDF, Green-Lagrange strain, and Second-Piola Kirchhoff stress tensor. It is crucial to interpolate all three components to ensure their compatibility with the solid mechanics. Compatibility, in this context, means ensuring that these parameters align smoothly with the principles of solid mechanics. If they are not compatible, the results may lack physical feasibility or fail to represent the mechanical behaviour of the system accurately.

Subsection 5.2.1 demonstrates that the Wang method operates most effectively when interpolating all three parameters. In this thesis, the Wang method employs the St. Venant-Kirchhoff material model during small displacements and the Neo-Hookean material model for large displacements. The SEDF is interpolated as expressed in Equation 5.1.

$$\phi = \phi_{HE}(\gamma_e \mathbf{u}) - \phi_{VK}(\gamma_e \mathbf{u}) + \phi_{VK}(\mathbf{u}) \tag{5.1}$$

Here, ϕ_{HE} represents the SEDF of a Neo-Hookean material model, as discussed in Subsection 4.1.2. Additionally, ϕ_{VK} is the SEDF of the St. Venant-Kirchhoff material model under the assumption of small deformations, as described in Section 2.3. Note that the ϕ_{VK} under the assumption of small deformation equivalent is to Hooke's law. The interpolation factor, γ_e, equals 0 for void elements and 1 for solid elements. Its expression is shown in Equation 5.2, where $\tilde{\rho}_e$ represents the projected design variable, as described in Subsection A.1.1, and p is the penalisation factor.

$$\gamma_e = \frac{tanh(\beta_1\eta_1) + tanh(\beta_1(\tilde{\rho}_e^p - \eta_1))}{tanh(\beta_1\eta_1) + tanh(\beta_1(1-\eta_1))} \tag{5.2}$$

The interpolation of the Second-Piola Kirchhoff stress tensor arises as a consequence of interpolating the SEDF since the stress is the derivative of the SEDF with respect to the Cauchy-Green deformation tensor $\mathbf{C}$, as expressed in Equation 5.3.

$$\mathbf{S} = \frac{\partial \phi}{\partial \mathbf{E}_{GL}} = 2\frac{\partial \phi}{\partial C} = 2\left(\frac{\partial \phi_{HE}(\gamma_e u)}{\partial C} - \frac{\partial \phi_{VK}(\gamma_e u)}{\partial C} + \frac{\partial \phi_{VK}(u)}{\partial C}\right) \tag{5.3}$$

The expressions for ϕ and $\mathbf{S}$ are lengthy; therefore, MATLAB is used to conduct these extensive calculations. The detailed formulations for ϕ and $\mathbf{S}$ are provided in the MATLAB code, presented in Section E.1.

The strain represents the third parameter requiring interpolation, which can be accomplished through the three methods enumerated below. In the COMSOL models, the plane strain assumption is used, meaning that all the z-components are zero.

1. **The first strain interpolation method**

   The first method involves interpolating the strain equivalent to the SEDF, expressed in Equation 5.4. Here, $\mathbf{E}_{GL}$ represents the Green-Lagrange strain, as defined in Equation 4.1, and $\boldsymbol{\epsilon}_L$ represents the linearised Green-Lagrange strain, as defined in Equation 2.3.

$$\begin{aligned} \mathbf{E}_{W,1} &= \mathbf{E}_{GL}(\gamma_e \mathbf{u}) - \boldsymbol{\epsilon}_L(\gamma_e \mathbf{u}) + \boldsymbol{\epsilon}_L(\mathbf{u}) \\ &= \begin{bmatrix} \frac{1}{2}(2u_{,X} + (u_{,X}^2 + v_{,X}^2)\gamma_e^2) & \frac{1}{2}(u_{,Y} + v_{,X} + (u_{,X}u_{,Y} + v_{,X}v_{,Y})\gamma_e^2) & 0 \\ \frac{1}{2}(u_{,Y} + v_{,X} + (u_{,X}u_{,Y} + v_{,X}v_{,Y})\gamma_e^2) & \frac{1}{2}(2v_{,Y} + (u_{,Y}^2 + v_{,Y}^2)\gamma_e^2) & 0 \\ 0 & 0 & 0 \end{bmatrix} \end{aligned} \tag{5.4}$$

2. **The second strain interpolation method**

   The second method involves directly interpolating the nonlinear component of the Green-Lagrange strain, as expressed in Equation 4.1, as shown in Equation 5.5.

$$\mathbf{E}_{W,2} = \begin{bmatrix} \frac{1}{2}(2u_{,X} + (u_{,X}^2 + v_{,X}^2)\gamma_e) & \frac{1}{2}(u_{,Y} + v_{,X} + (u_{,X}u_{,Y} + v_{,X}v_{,Y})\gamma_e) & 0 \\ \frac{1}{2}(u_{,Y} + v_{,X} + (u_{,X}u_{,Y} + v_{,X}v_{,Y})\gamma_e) & \frac{1}{2}(2v_Y + (u_Y^2 + v_Y^2)\gamma_e) & 0 \\ 0 & 0 & 0 \end{bmatrix} \tag{5.5}$$

3. **The third strain interpolation method**

   The third method involves interpolating the deformation gradient as expressed by $F = I + \gamma_e \nabla u$, a method based on the methodology presented by Dalklint et al. (2021). This approach results in the strain expressed in Equation 5.6. However, it is essential to note that when γ_e equals 0, the strain is 0, which can lead to numerical issues. It is anticipated that Dalklint et al. (2021) used an alternative strain interpolation method. Consequently, this option is not further considered in this thesis.

$$\mathbf{E}_{W,3} = \begin{bmatrix} \frac{1}{2}(2\gamma_e u_{,X} + (u_{,X}^2 + v_{,X}^2)\gamma_e^2) & \frac{1}{2}((u_{,Y} + v_{,X})\gamma_e + (u_{,X}u_{,Y} + v_{,X}v_{,Y})\gamma_e^2) & 0 \\ \frac{1}{2}((u_{,Y} + v_{,X})\gamma_e + (u_{,X}u_{,Y} + v_{,X}v_{,Y})\gamma_e^2) & \frac{1}{2}(2\gamma_e v_{,Y} + (u_{,Y}^2 + v_{,Y}^2)\gamma_e^2) & 0 \\ 0 & 0 & 0 \end{bmatrix} \tag{5.6}$$

The distinction between Equation 5.4 and Equation 5.5 lies in the scaling of the nonlinear part. In Equation 5.4, the nonlinear part is scaled with γ_e^2, while in Equation 5.5, it is scaled with γ_e. The effects of the first and second strain interpolation methods will be investigated in Subsection 5.2.1.

5.2. Case Study

The Wang method is applied to a case study based on three different problems to investigate the effectiveness. The initial case involves the analysis of a C-beam, as discussed in Subsection 5.2.1. This straightforward scenario is a preliminary test to validate the method's effectiveness. Subsequently, a study is conducted on the TO of a cantilever beam, explored in Subsection 5.2.2. The cantilever beam is chosen due to its simplicity and well-known TO shape. Lastly, the third case involves the TO of an inverter, presented in detail in Subsection 5.2.3.

The mesh employed in the models is the 'extra-fine-sized physics-controlled' mesh generated by COMSOL. Depending on the physics involved, COMSOL determines how to mesh the domain using triangular elements with a maximum element size. This maximum element size is problem-dependent.

5.2.1. C-beam

The paper by Yoon et al. (2005) initially introduced the C-beam test, emphasising that void elements exhibit distortion during large displacements, especially when accounting for geometric nonlinearities in the solid mechanics. Building upon this, Wang, Lazarov, Sigmund, and Jensen (2014) further demonstrated the effectiveness of this method by combining the C-beam test with the Wang method.

The schematic visualisation of the C-beam is presented in Figure 5.1. In this simulation, the solid beam is represented by the grey region where $\gamma_e = 1$, while the white region, where $\gamma_e = 0$, simulates the void region. Including the void region in the C-beam is crucial, as it allows us to demonstrate the effectiveness of the Wang method in handling void regions.

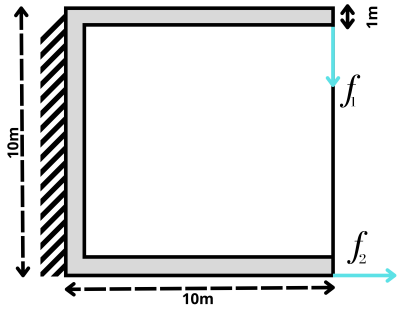

Figure 5.1: The schematic visualisation and corresponding boundary conditions of the C-beam, where the grey part ($\gamma_e = 1$) signifies a solid region, while the white part ($\gamma_e = 0$) mimics the void regions. This figure is based on the paper of Yoon et al. (2005)

The C-beam incorporating the Neo-Hookean material is simulated in COMSOL, where the notation and values assigned to various parameters can be found in Table 5.1. The meshes of the results obtained from the analysis are illustrated in Figure 5.2. In Figure 5.2a, the maximum deformation achievable for the C-beam is shown, corresponding to a maximum applied load of $(f_1, f_2) = (0.0009\text{ N}, 0.0099\text{ N})$. Exceeding this load would lead to the mesh shown in Figure 5.2b, with distorted elements causing numerical instabilities and resulting in infeasible designs.

Parameter	Notation	Value
Maximum element size	-	0.37 m
Young's modulus solid region	E_1	1 N m^{-2}
Young's modulus void region	E_0	1×10^{-9} N m^{-2}
Out-of-plane thickness	t	1 m
Poisson ratio	ν	0.3

Table 5.1: The notation and value for various parameters used to simulate the C-beam in COMSOL.

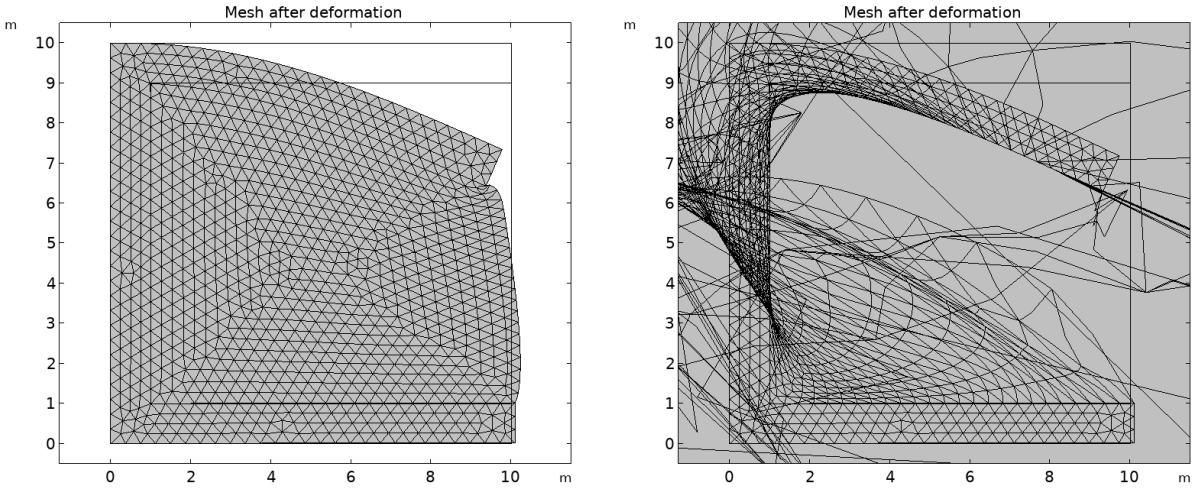

(a) The mesh for $(f_1, f_2) = (0.0009, 0.0099)$

(b) The mesh for $(f_1, f_2) = (0.001, 0.01)$

Figure 5.2: The results obtained from the analysis of the C-beam are presented in (a) for the maximum allowable applied load and in (b) for conditions exceeding the maximum allowable applied load. The analysis incorporates a Neo-Hookean material model.

Why is it necessary to interpolate the Green-Lagrange strain, the SEDF, and the Second Piola-Kirchhoff stress? The answer to this question is provided in Figure 5.3. Figure 5.3a illustrates the C-beam with a Neo-Hookean material model, thus without interpolation. Figure 5.3b illustrates the effect of interpolating just the SEDF. Figure 5.3c illustrates the effect of the combination of interpolating the SEDF and strain ($\mathbf{E}_{W,1}$) but not the Second Piola-Kirchhoff stress. Figure 5.3d illustrates the effect of interpolating the combination of the SEDF, strain ($\mathbf{E}_{W,1}$), and the Second Piola-Kirchhoff stress (Wang method). The maximum applied load for all models is listed in Table 5.2.

Material model	f_1 (N)	f_2 (N)
Neo-Hookean material model	0.0009	0.0099
Interpolation of the SEDF	0.0008	0.0018
Interpolation of the SEDF and $\mathbf{E}_{W,1}$	0.0055	0.0145
Interpolation of the SEDF, $\mathbf{E}_{W,1}$, and the Second Piola-Kirchhoff stress (Wang method)	0.0055	0.0145

Table 5.2: The maximum values of the applied loads f_1 and f_2 for the different material models of a C-beam.

Figure 5.3 illustrates the successful implementation of the Wang method for the analysis of the C-beam. Clearly, the maximum allowable displacement is optimised in both Figure 5.3c and Figure 5.3d. However, the latter exhibits a higher capability at handling distorted elements. Hence, if effective management of distorted elements management is required, the Wang method is recommended.

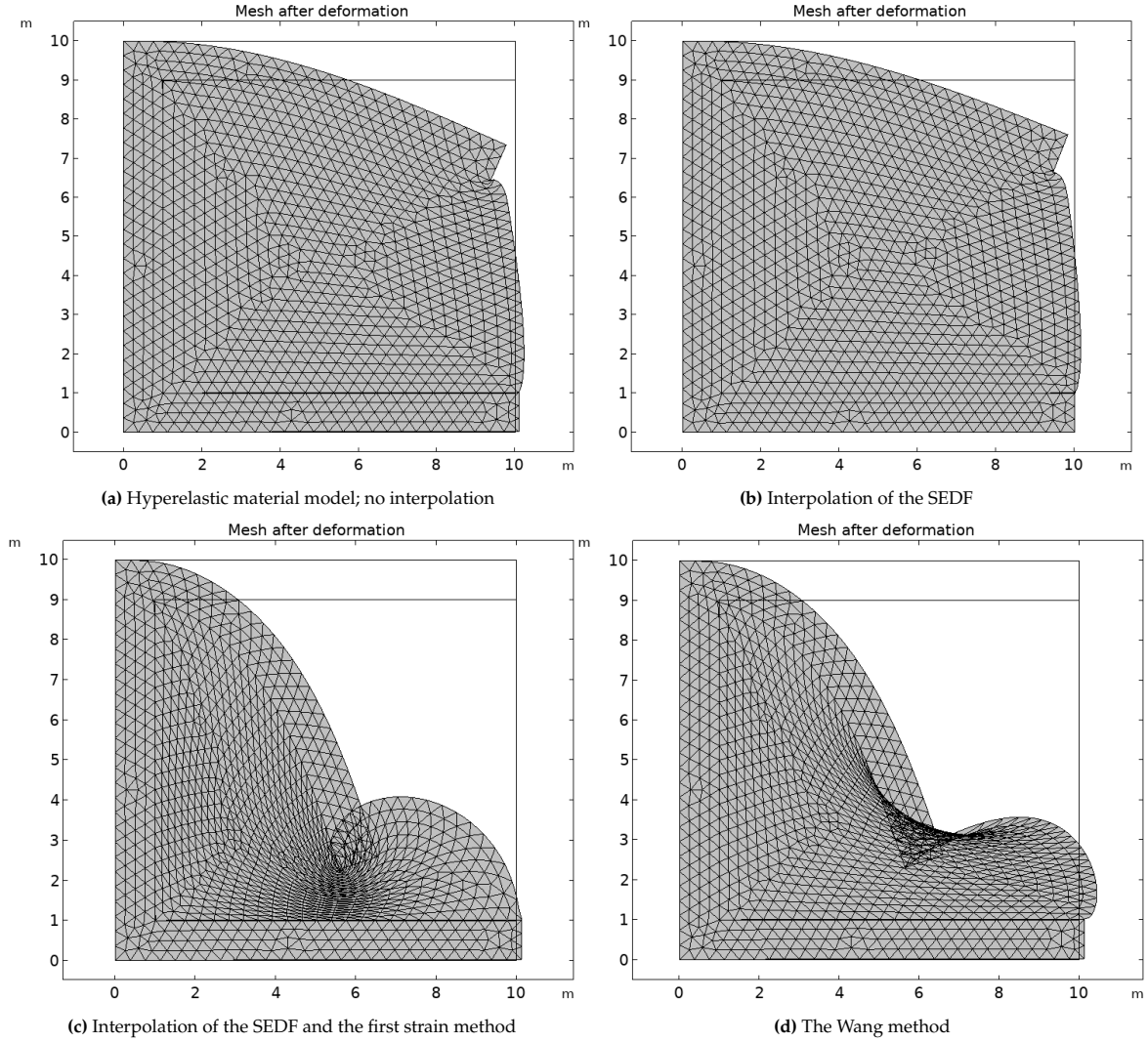

(a) Hyperelastic material model; no interpolation

(b) Interpolation of the SEDF

(c) Interpolation of the SEDF and the first strain method

(d) The Wang method

Figure 5.3: The analysis results of a C-beam using different approaches: (a) Neo-Hookean material model, (b) interpolation of only the SEDF, (c) interpolation of SEDF and the first strain method, excluding the Second Piola-Kirchhoff stress, and (d) the Wang method.

It can be concluded that no difference is observed in the results between the Wang method using $\mathbf{E}_{W,1}$ or $\mathbf{E}_{W,2}$. In Figure 5.4, the results of the C-beam analysis using two variations of the Wang method are depicted. Specifically, Figure 5.4a illustrates the outcome of the Wang method with $\mathbf{E}_{W,1}$, while Figure 5.4b presents the results for the Wang method incorporating $\mathbf{E}_{W,2}$. Both strain methods yield equivalent results and maximum allowable applied loads for the C-beam, specifically $(f_1, f_2) = (0.0103, 0.0193)$.

The C-beam is constrained to values of either 0 or 1 for γ_e. However, a difference in the results will become visible for intermediate values for γ_e, which can occur during TO. A study examines the impact of the intermediate values, which is detailed in Appendix C. Nevertheless, the differences in the results obtained from the TO of structures or CMs are marginal. Henceforth, the focus will solely be on $\mathbf{E}_{W,1}$. This choice ensures a consistent interpolation method for the SEDF, strain and Second Piola-Kirchhoff stress.

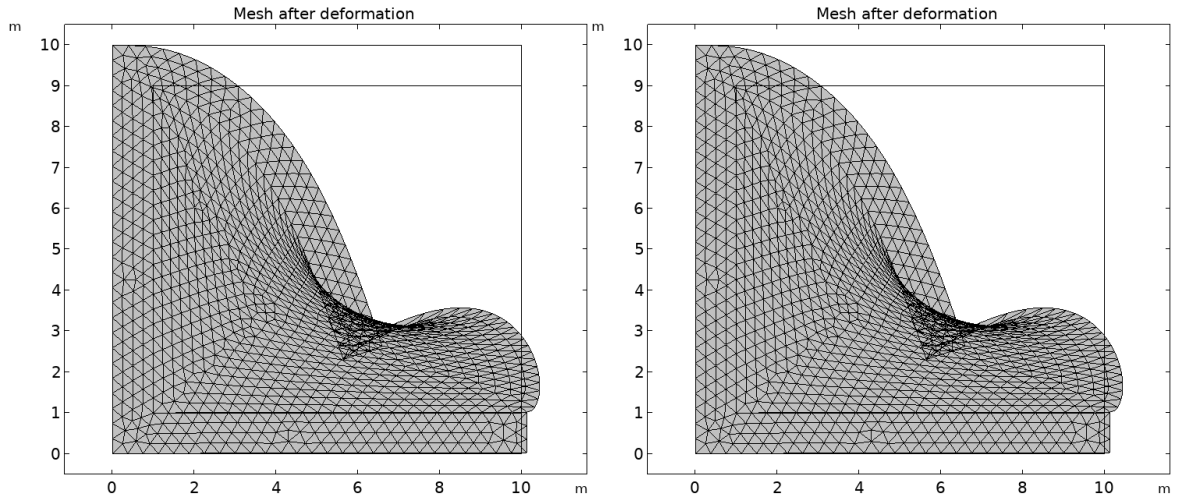

(a) Wang method with $\mathbf{E}_{W,1}$ **(b)** Wang method with $\mathbf{E}_{W,2}$

Figure 5.4: Mesh of the maximum deformation obtained from the analysis of the C-beam with the Wang Method using $\mathbf{E}_{W,1}$ (a) and $\mathbf{E}_{W,2}$ (b).

5.2.2. Topology optimisation of a cantilever beam

This subsection presents results obtained from the TO with the Wang method incorporated into the solid mechanics of a cantilever beam. The cantilever beam, chosen for its simplicity and well-known TO shape, is schematically visualised in Figure 5.5 with associated boundary conditions. The notation and value assigned to various parameters used in the COMSOL model can be found in Table 5.3. The results are derived from fifty iterations of the Global Convergent Method of Moving Asymptotes (GCMMA) algorithm, indicating that the TO likely reached convergence. The GCMMA is explained in Subsection A.4. Additionally, the TO formulation aligns with the formulation stated in Subsection 2.4.1

Parameter	Notation	Value
Maximum element size	-	0.01 m
Volume fraction	volfrac	0.5
Young's modulus solid region	E_1	3×10^9 N m^{-2}
Young's modulus void region	E_0	3×10^3 N m^{-2}
Out-of-plane thickness	t	0.1 m
Poisson ratio	ν	0.4

Table 5.3: The notation and value for various parameters used to design the cantilever beam in COMSOL.

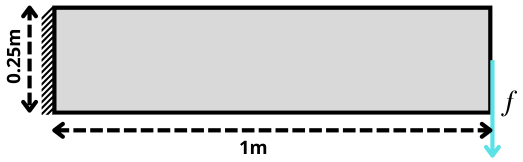

Figure 5.5: The schematic visualisation and the associated boundary conditions of a cantilever beam.

In this section, the COMSOL model excludes a Helmholtz density filter or a projection on the design variables. Integrating a Helmholtz density filter with the Wang method posed challenges, resulting in unsolvable problems, which are investigated in Section D.1. Additionally, a parameter study on the γ_e values was conducted to determine optimal settings, outlined in Appendix D. This study also explored the use of a projection on the design variables, detailed in section D.5. However, implementing a projection on the design variables led to significantly increased computational times, prompting the decision to forego the use of a filter.

The subsections are structured as follows: Initially, details on the TO with a linear elastic and Neo-Hookean material model of a cantilever beam are presented, which serve as a reference for validating the implementation of the Wang method. Finally, the Wang method is incorporated into the solid mechanics of the TO process.

Linear topology optimisation

To establish a reference for the results obtained from the TO with the Wang method, the outcomes of the linear model are first analysed, as illustrated in Figure 5.6. Specifically, this figure depicts the material distribution obtained from the linear TO under an applied load of 400 kN. It is crucial to highlight that in the linear TO, the results are load-independent. This figure serves the dual purpose of validating and verifying the implemented numerical model in COMSOL, as it produces results identical to those obtained with the 88-line MATLAB code outlined in the paper by Andreassen et al. (2011)

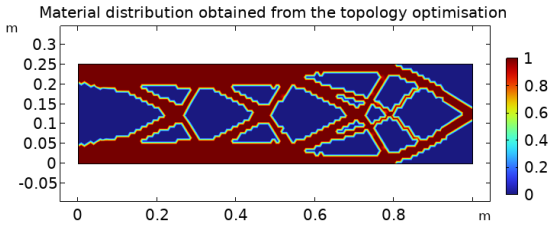

Figure 5.6: The material distribution obtained from the linear TO of a cantilever beam.

Topology optimisation with a Neo-Hookean material model

In this subsection, the Neo-Hookean material model is integrated into the TO process, and the results are presented in Figure 5.7. Understanding these results is crucial for comparing the Wang method with just a Neo-Hookean material model. The purpose is to assess the impact of the Wang method, which should minimally influence the shape of the results when combined with a Neo-Hookean material model. Therefore, Figure 5.7 serves as a reference to validate the correct implementation of the Wang method in the TO of a cantilever beam.

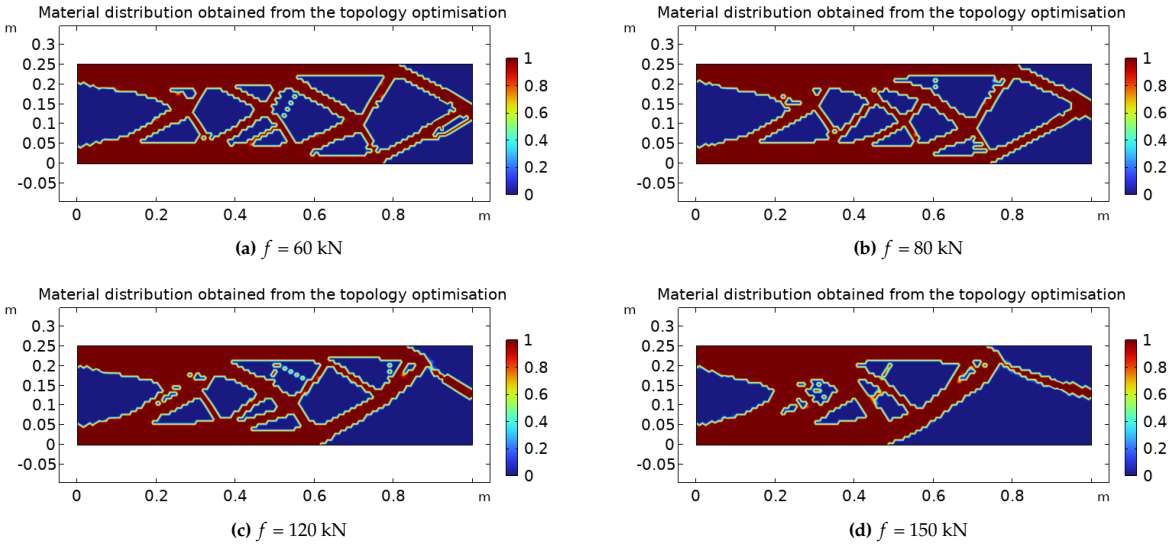

(a) $f = 60$ kN **(b)** $f = 80$ kN

(c) $f = 120$ kN **(d)** $f = 150$ kN

Figure 5.7: The material distribution obtained from the TO with a Neo-Hookean material model of a cantilever beam under various values of the applied load.

The maximum applied load achievable during the TO of the cantilever beam is 150 kN, where the obtained result is depicted in Figure 5.7d. The designs obtained from the TO are similar to those reported in the literature, particularly in the work by Wang, Lazarov, Sigmund, and Jensen (2014). The obtained design shown in Figure 5.7c and Figure 5.7d may be peculiar for readers unfamiliar with the nonlinear TO of a cantilever beam. However, when the applied load is large, the optimisation process creates a beam dangling from the truss structure. This dangling beam is a strategic response to overcome the significant displacements and loads applied to the structure and will become longer for an increasing applied load.

For clarity, Figure 5.8 illustrates the deformed shape resulting from the TO with a Neo-Hookean material model of a cantilever beam under an applied load of 150 kN. This figure contributes to developing an intuitive understanding of the results obtained from the nonlinear TO and the corresponding displacements. It is important to note that the design presented in Figure 5.8 is a filtered design shown in Figure 5.7d, where design variables are thresholded at 0.5. Consequently, values of design variables lower than 0.5 are removed.

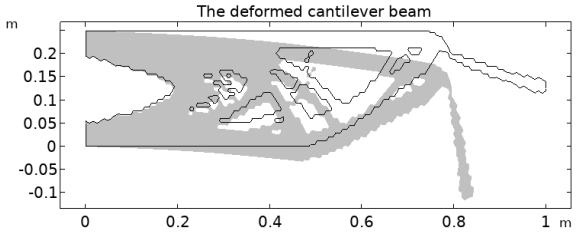

Figure 5.8: The deformed shape of the obtained design from the TO with a Neo-Hookean material model of a cantilever beam under an applied load of 150 kN. The displacements are not scaled.

Topology optimisation with the Wang method

As explained, γ_e interpolates the solid mechanics between linear and nonlinear theory. However, when γ_e is set to 0 for all elements of the domain, the model is equivalent to the linear elastic material model. On the other hand, when γ_e is set to 1 for all elements of the domain, it corresponds to a model incorporating the Neo-Hookean material model. These two comparisons are crucial for validating the implementation of the Wang method. If either of these tests fails, it indicates an issue with the Wang method implementation. It is important to note that when γ_e is set to 0 or 1 for all elements in the domain, no interpolation occurs.

Consistent alignment is obtained between the Wang method, with γ_e set to 0 and 1, and the TO employing linear elastic and Neo-Hookean material model, respectively, confirming the correct implementation of the Wang method.

In Figure 5.9, the comparison is made between results obtained from the linear TO and the TO with the Wang method where γ_e is set to 0 for all elements in the domain. This comparison illustrates the equivalence of Figure 5.9a and Figure 5.9b. Additionally, the objective functions obtained for each TO iteration are identical for both models.

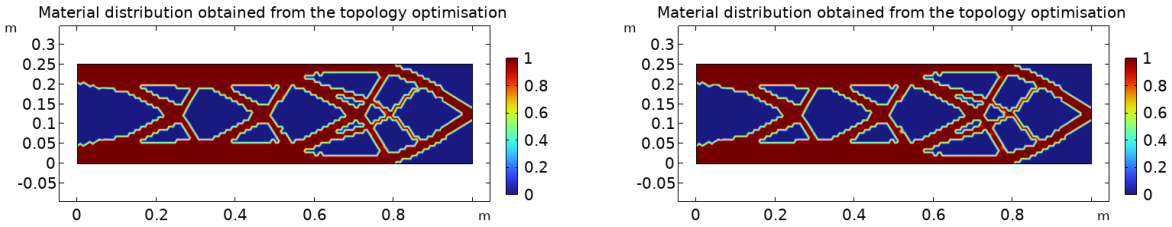

(a) TO with a linear elastic material model

(b) TO with the Wang method where $\gamma_e = 0$

Figure 5.9: The comparison between the results of the (a) linear TO and (b) TO with the Wang method where γ_e is set to 0 for all elements for a cantilever beam under an applied load of 80 kN.

Furthermore, Figure 5.10 demonstrates the comparison between the results of the TO with the Neo-Hookean material model and the Wang method where γ_e is set to 1 for all elements in the domain. This figure demonstrates the equivalence of the two subfigures. Moreover, the objective functions obtained for each TO iteration are identical for both models.

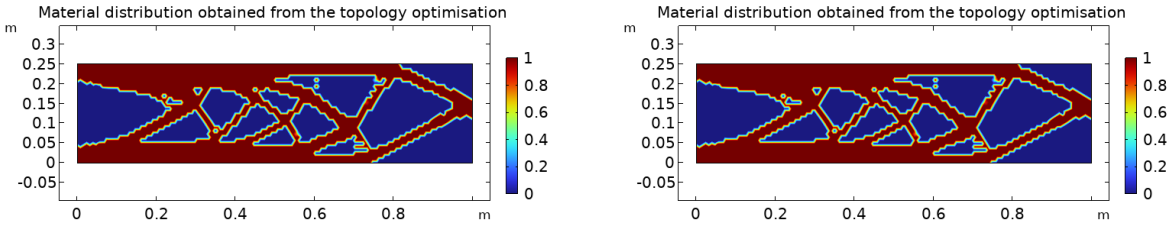

(a) TO with the Neo-Hookean material model

(b) TO with the Wang method with $\gamma_e = 1$

Figure 5.10: The comparison between the results of a TO of a cantilever beam with a Neo-Hookean material model (a) and the Wang method where the interpolation factor γ_e is equal to 1 (b) of a cantilever beam under an applied load of 80 kN

It should be noted that γ_e has returned to its original definition, as given in Equation 5.2, enabling interpolation between linear and nonlinear theories. The parameters β_1, η_1, and p for γ_e are set to 100, 0.001, and 3, respectively. The TO results with the Wang method for the cantilever beam under various applied loads are depicted in Figure 5.11, with additional results provided in section D.6. This figure illustrates that the little beam dangling from the truss structure elongates under increasing applied loads. The maximum applied load is 250 kN, which represents an increase of 100 kN compared to the results obtained with the Neo-Hookean material model in Figure 5.7. In Figure 5.12, the deformed shape resulting from the TO with the Wang method under an applied load of 250 kN is illustrated.

The comparison between the results presented in Figure 5.11a and Figure 5.11b and those in Figure 5.7b and Figure 5.7d, similarities in shape are evident. This underscores the capability of the Wang method to generate designs that resemble those obtained from the TO with a Neo-Hookean material model.

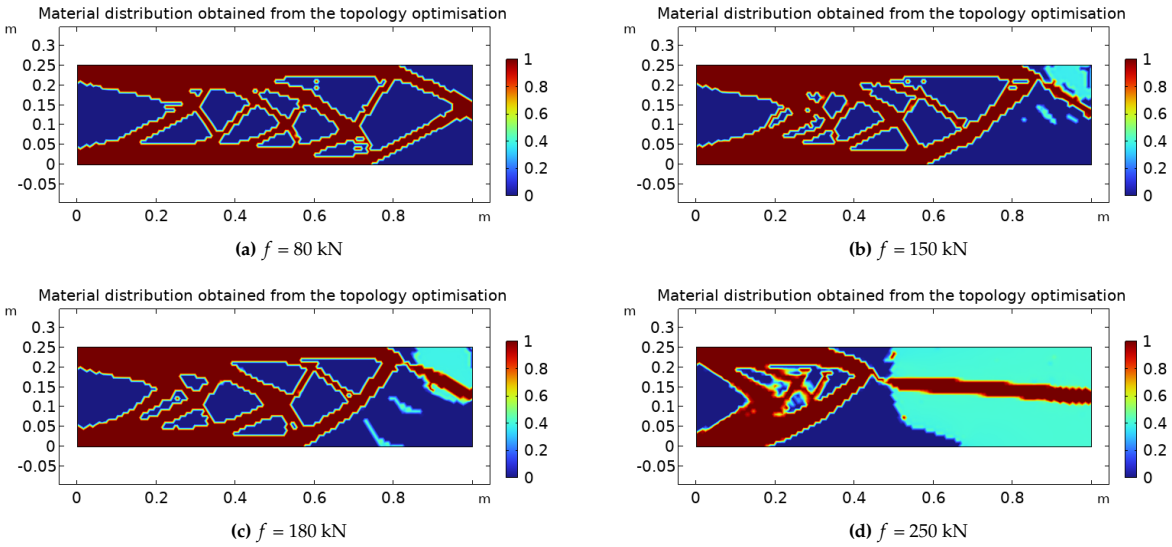

(a) $f = 80$ kN

(b) $f = 150$ kN

(c) $f = 180$ kN

(d) $f = 250$ kN

Figure 5.11: The material distribution obtained from the TO with the Wang method of a cantilever beam under various values of the applied load.

Moreover, the material distributions show more intermediate values than those obtained from the TO with the Neo-Hookean material model. However, this has only a 4% impact on the objective function under a 150 kN load, whereas the TO with the Wang method has the better objective function. Hence, it can be asserted that these intermediate values do not significantly affect the achieved objective function.

The reason for these intermediate values remains uncertain and warrants further investigation. While adjusting the model settings may reduce the intermediate value, it is beyond the thesis scope. However, it is crucial to emphasise that the purpose of this study was to investigate whether the Wang method effectively enhances the maximum applied load.

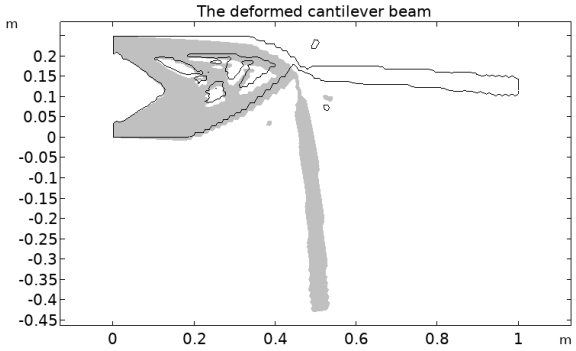

Figure 5.12: The deformed shape of the filtered design obtained from the TO with the Wang method of a cantilever beam under an applied load of 250 kN. The displacement is not scaled

5.2.3. Topology optimisation of an inverter

The results of the TO with the incorporation of the Wang method in the solid mechanics of an inverter are discussed in this subsection. The schematic visualisation and the corresponding boundary conditions are provided in Figure 5.13. The notation and values for various parameters used in COMSOL are detailed in Table 5.4. Furthermore, each result is based on one hundred iterations using the GCMMA algorithm, indicating that the TO has likely reached convergence. Additionally, the TO formulation for the inverter aligns with the formulation stated in Subsection 2.4.2, where the objective function aims to maximise the displacement Δ in the horizontal direction.

Parameter	Notation	Value
Maximum element size	-	3 μm
Volume fraction	volfrac	0.2
Young's modulus solid region	E_1	3×10^9 N m^{-2}
Young's modulus void region	E_0	3×10^3 N m^{-2}
Out-of-plane thickness	t	7 μm
Poisson ratio	ν	0.3
Stiffness left spring	k_{in}	4000 Nm^{-1}
Stiffness right spring	k_{out}	40 Nm^{-1}

Table 5.4: The notation and value for various parameters used to design the inverter in COMSOL.

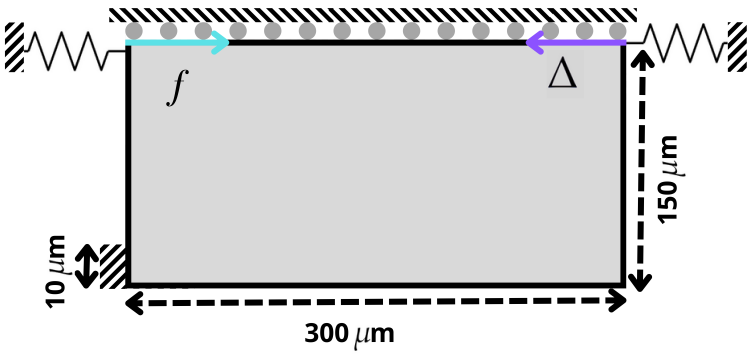

Figure 5.13: The schematic visualisation and the corresponding boundary conditions of the inverter.

Similar to the TO of a cantilever beam discussed in subsection 5.2.2, this chapter initially presents the results obtained from the linear TO and the TO with a Neo-Hookean material model of an inverter. The aim is to establish a reference for validating the implementation of the Wang method. Subsequently, the Wang method is incorporated into the solid mechanics of the TO process of the inverter.

Topology optimisation with a linear elastic material model
As mentioned earlier, the results of the linear TO serve to validate the correct implementation of the model in COMSOL and act as a reference for the results obtained from the TO with the Wang method of the inverter. Figure 5.14 represents the material distribution obtained from the TO of the inverter under an applied load of 0.02 N. The obtained shape is similar to those reported in the literature, particularly in the work by Wang, Lazarov, Sigmund, and Jensen (2014). Additionally, Figure 5.15 illustrates the filtered design of the results obtained from the linear TO, where the design variables are thresholded at 0.5. This figure validates the working principle of an inverter.

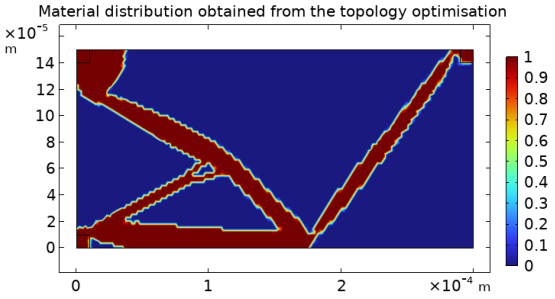

Figure 5.14: The material distribution obtained from the linear TO of an inverter under an applied load of 0.02 N.

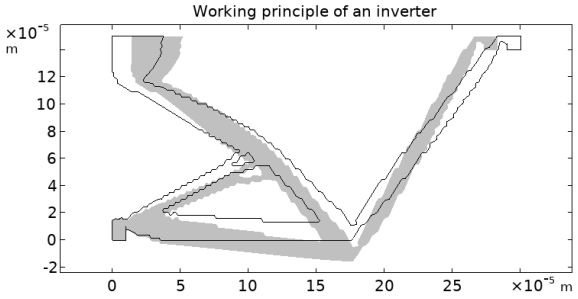

Figure 5.15: The displacement is illustrated, which validates the working principle of an inverter.

Topology optimisation including a Neo-Hookean material model
The results obtained from the TO with a Neo-Hookean material model for an inverter are shown in Figure 5.16. This figure illustrates the material distribution under various applied loads, with a maximum of 0.4 N. It can be observed that the obtained designs for the input load of 0.02N contain one distinction rotation point in the upper-right corner, while for input loads of 0.1N and 0.2 N, there exist two. These distinct rotation points function similarly to a revolute joint and these three cases show similarities with the linear case. However, for an input load of 0.4 N, it can be observed that these distinction joints changed in a somewhat more distributed deformation pattern.

It is expected that these differences can be explained by an underlying concept. Various formulations of TO exist for designing CMs. In cases where linear TO is employed with the objective of maximising energy transfer, the designs become sensitive to achieving specific rotation points (Wang and Chen 2009; Yin et al. 2003). However, challenges arise when geometric nonlinearities manifest due to large deformations. The distinct rotation points in these lumped designs tend to drift in such scenarios, attributed to the stiffness becoming deformation-dependent through geometric nonlinearities (Trease et al. 2004; Clark et al. 2016; Xu 2014). These studies offer solutions to counteract this drift. Notably, the drifting behaviour of the rotation point is not inherently problematic; nevertheless, it is prone to occur when left unmitigated.

Moreover, it is conjectured that introducing nonlinearities into the TO process results in a shift towards a distributed deformation pattern rather than a lumped design, which is attributed to the drifting of the rotation points [S. Koppen, personal communication, January 13, 2024].

This concept can potentially contribute to the distinctions observed in Figure 5.16. Especilly, since the expected deformation obtained from the TO are large. The deformed shape of the 0.4 N design is depicted in Figure 5.17, offering valuable insight into displacement magnitude and illustrating the response of the cantilever beam to the applied load.

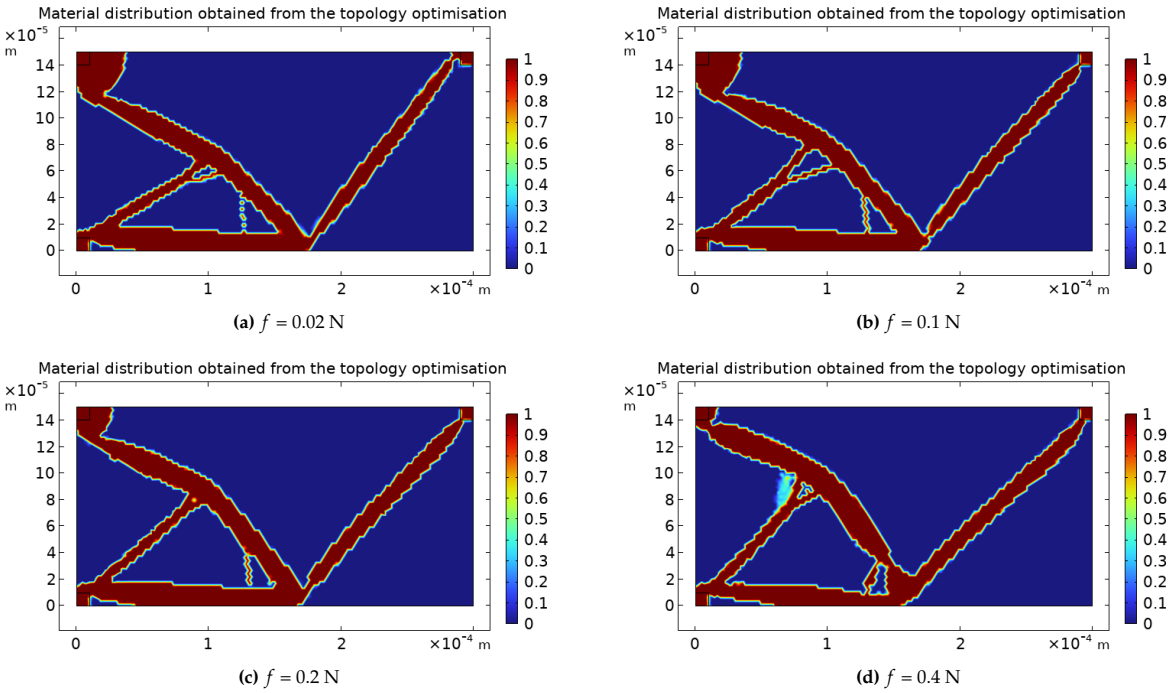

(a) $f = 0.02$ N **(b)** $f = 0.1$ N

(c) $f = 0.2$ N **(d)** $f = 0.4$ N

Figure 5.16: The material distribution obtained from the TO with a Neo-Hookean material model of an inverter under various values of the applied load

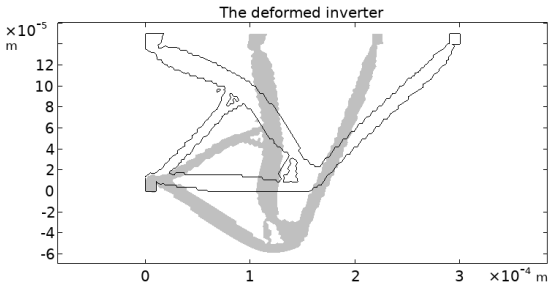

Figure 5.17: The deformed shape of the obtained design from the TO with the Wang method of a cantilever beam under an applied load of 0.4 N. The displacement is not scaled.

Topology optimisation including the Wang method

The correct implementation of the Wang method in this model is confirmed through the examination of the results obtained from the TO with the Wang method, where γ_e is set to 0 and 1. Although detailed results are not provided here, it is noteworthy that when γ_e is set to 0 and 1, the design and objective function align with the linear TO and TO with the Neo-Hookean material model, respectively.

It should be noted that γ_e has returned to its original definition, as given in Equation 5.2, enabling interpolation between linear and nonlinear theories. The parameters β_1, η_1, and p for γ_e are set to 100, 0.001, and 3, respectively.

In contrast to the findings in the cantilever beam case discussed in Subsection 5.2.2, the study concludes that there is no increase in the maximum applied load for the TO of an inverter when employing the Wang method. The results presented in Figure 5.18 illustrate the results obtained from the TO with the Wang method for applied loads of 0.02 N and 0.4 N. Notably, the maximum applied load achieved with the Wang method is 0.4 N, equivalent to the TO results obtained by solely incorporating the Neo-Hookean material model.

A parameter study explored the influence of modifying β_1, η_1, and p on the maximum applied load. Unfortunately, these modifications did not yield a higher maximum applied load. Notably, the Wang method was implemented across various types of compliant mechanisms, including PACM; however, it consistently failed to extend the range of maximum allowable applied load in COMSOL.

Additionally, shapes obtained from the TO using the Wang method exhibit similarities to those achieved with the Neo-Hookean material model. However, distinct differences between the two obtained designs exist. Nevertheless, the two designs show an insignificant difference in the objective function, with the Wang method outperforming and yielding only a 4% improvement. The most significant conclusion of this study is that the Wang method is ineffective in extending the range of the maximum allowable load.

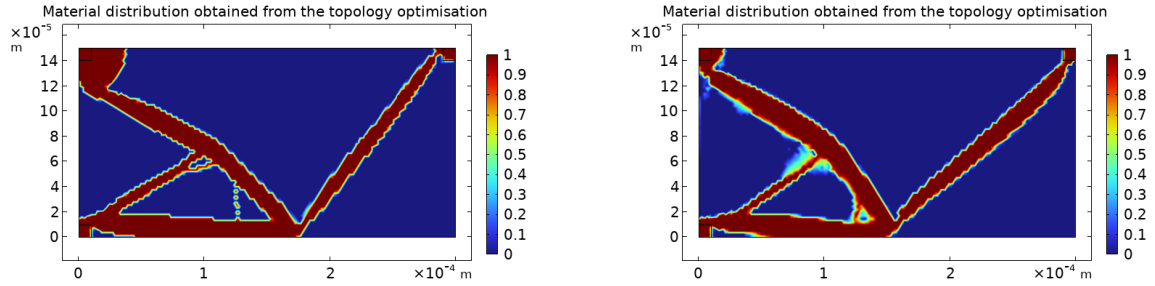

(a) $f = 0.02$ N **(b)** $f = 0.4$ N

Figure 5.18: The material distribution obtained from the TO with the Wang method of a cantilever beam under an applied load of 0.02 N (a) and 0.4 N (b).

6

Case study nonlinear topology optimisation pressure-actuated compliant mechanism

This section presents the design and analysis of several PACMs, illustrating the impact of incorporating geometric nonlinearities and a Neo-Hookean material model in conjunction with the Darcy method. The goal is to observe how nonlinearities can be incorporated into PA soft robots using the Darcy method for pressure boundary identification in COMSOL. In the COMSOL models, the plane strain assumption is used, meaning all the z-components are zero. Note that PA soft robots and PACMs are considered equivalent in this thesis. Table 6.1 provides values and notation for various parameters used in the COMSOL models, which remain consistent across all examples unless otherwise stated. The TO formulation used for the PACMs in this chapter is similar to the formulation stated in section 3.2.

Parameter	Notation	Value
Poisson ratio	ν	0.4
Out-of-plane thickness	t	0.001 m
Penalisation factor	p	3
External move limit	$\Delta\boldsymbol{\rho}$	0.1 per iteration
$K(\rho_e)$ step location	η_k	0.3
$K(\rho_e)$ slope of the step	β_k	10
$D(\rho_e)$ step location	η_h	0.2
$D(\rho_e)$ slope of the step	β_h	10
Flow coefficient of the void element	k_v	$1\ \mathrm{m^4N^{-1}s^{-1}}$
Flow coefficient of the solid element	k_s	$k_v \times 10^{-7}\mathrm{m^4N^{-1}s^{-1}}$
Ratio input pressure to the pressure at Δs	r	0.1
The penetration depth	Δs	0.002 m
Volume fraction	volfrac	0.2
Stiffness of the output spring	k_{ss}	$1 \times 10^4\mathrm{Nm^{-1}}$
Output pressure	$\boldsymbol{p}_{out}$	0 Pa

Table 6.1: The notation and value for various parameters used in the COMSOL models.

The mesh employed in the models is the 'extra-fine-sized physics-controlled' mesh generated by COMSOL. Depending on the physics involved, COMSOL determines how to mesh the domain, employing triangular elements with a maximum element size. For the PA inverter, compliant gripper, and multi-material compliant gripper, the maximum element size is set to 0.004m. In contrast, for the member of a pneumatic network, it is set to 0.003m. It is an option in COMSOL to determine the mesh manually; however, a user-defined mesh tends to be more sensitive to numerical instabilities.

In this chapter, the 'linear model' refers to the model with the TO with a linear elastic material model integrated into the solid mechanics. The 'nonlinear model' refers to the model with the TO with geometric nonlinearities and a linear elastic material model integrated into the solid mechanics. The 'Neo-Hookean model' refers to the model with the TO with geometric nonlinearities and a Neo-Hookean material model integrated into the solid mechanics.

For all cases, this chapter presents the results of the TO with different material models. Subsequent to the TO, the obtained material distribution undergoes thresholding of design variables at 0.5, as illustrated in Figure 6.1. This thresholding involves the removal of design variable values below 0.5. These designs are referred to as 'the filtered designs' [1]. The analysis will then concentrate on the resulting designs after remeshing.

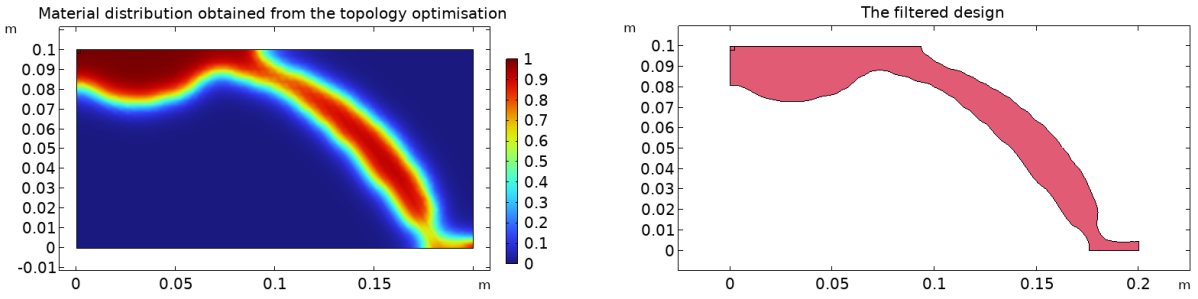

(a) The material distribution obtained from the TO of a PA inverter

(b) The filtered design with the design variables thresholded at 0.5

Figure 6.1: An example of the filtering design obtained from the TO, where the design variables are thresholded at 0.5. (a) illustrates the material distribution obtained from the TO of a PA inverter. (b) shows the filtered design used in the analyses.

In this study, two analyses are conducted subsequent to the TO. The first analysis utilises the Darcy method to determine the pressure field, following a similar approach to the TO. The second analysis applies a direct pressure load to the relevant boundary. In COMSOL, an applied pressure load is converted into a follower force when integrating a Neo-Hookean material model in the solid mechanics. It is crucial to note that the pressure is independent of the deformation in the first analysis, while in the second analysis, the pressure is deformation-dependent. The Neo-Hookean material model is integrated into the solid mechanics of both analyses. For clarity in this thesis, the first analysis is referred to as the deformation-independent load analysis, and the second analysis is denoted as the follower force analysis. The deformation-independent load analysis is conducted to compare the linear model with the Neo-Hookean model to observe the influence of a Neo-Hookean material model. A follower force analysis is conducted for comparison with the deformation-independent load analysis, aiming to observe the effect of a deformation-dependent pressure load on the model.

This chapter is structured as follows: Section 6.1 discusses the PA inverter results. Section 6.2 discusses the results of the PA compliant gripper. Section 6.3 illustrates the results of a member of a Pneumatic network (Pneunets). Section 6.4 presents the results of a multi-material PA compliant gripper.

6.1. Pressure-actuated inverter

This section presents the results obtained from the TO of a PA inverter. The schematic visualisation is shown in Figure 6.2, representing the symmetric half of the design domain and its boundary conditions. The Young's modulus E_1 for the solid material is $3 \times 10^9 \mathrm{N/m^2}$, while the Young's modulus for the void regions $E_0 = E_1 \times 10^{-6} \mathrm{N/m^2}$. Furthermore, each result is derived from fifty iterations using the GCMMA, indicating that the TO has likely reached convergence. The objective function focused on minimising Δ divided by the total strain energy. Here, Δ represents the displacement in the x-direction in the bottom-right corner.

[1] It is crucial for the reader to distinguish between the filtered design obtained after the TO and the filtering process in the TO process. When referred to as 'the filtered design,' the term signifies the extracted design from the material distribution obtained from the TO.

Figure 6.3 illustrates the designs obtained from the linear model for input pressure loads of 1×10^6 Pa and 1×10^7 Pa. Similarly, Figure 6.4 presents the designs obtained from the Neo-Hookean model for the same input pressure loads. These figures depict the values of the design variable for each element in the obtained results of the TO of a PA inverter under different values for the input pressure load. In other words, they represent the material distribution for different pressure load values.

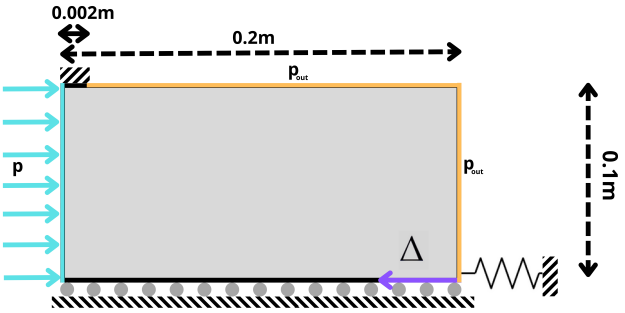

Figure 6.2: The schematic visualisation and the corresponding boundary conditions of PA inverter.

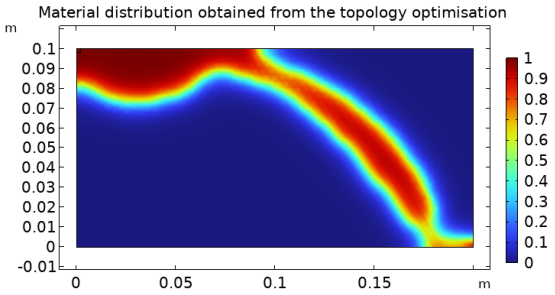

(a) p = 1×10^6 Pa

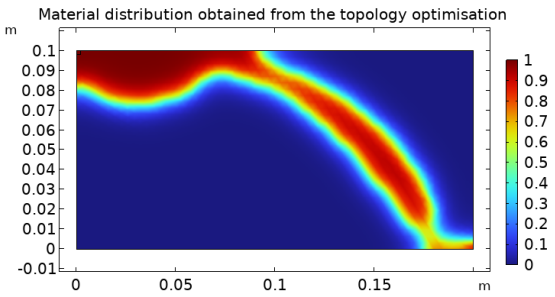

(b) p = 1×10^7 Pa

Figure 6.3: The material distribution obtained from the linear model of a PA inverter under two different input pressure load values.

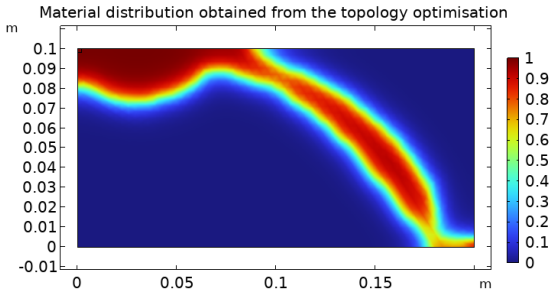

(a) p = 1×10^6 Pa

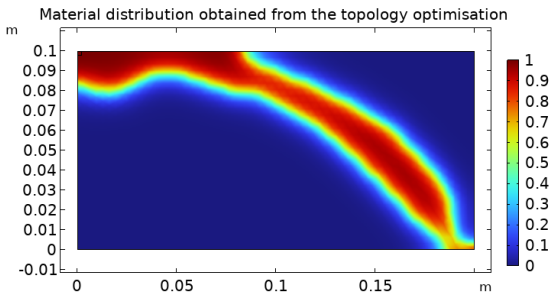

(b) p = 1×10^7 Pa

Figure 6.4: The material distribution obtained from the Neo-Hookean model for a PA inverter under two different input pressure load values.

The results of the nonlinear models are omitted in this thesis since they show no significant difference compared to the linear and Neo-Hookean models. The nonlinear model produces results only up to an input pressure load of 5×10^5 Pa, which is very low compared to the maximum input pressure load of the Neo-Hookean model. Remarkably, the differences between the design obtained from the nonlinear and linear models are negligible.

In contrast, incorporating the Neo-Hookean material model allows for a maximum input pressure load of 1×10^7Pa during the TO. Exceeding this pressure load is impossible since the simulation will result in a not-converge error, shown in Figure 6.5. The error occurs because of the excessive displacement obtained in the analysis of the first TO iteration, shown in Figure 6.6. These excessive displacements are causing numerical issues and making the model unsolvable. In Figure 6.6, it should be noted that the square in the top-left corner represents the undeformed design domain, while the blue area corresponds to a part of the deformed design domain.

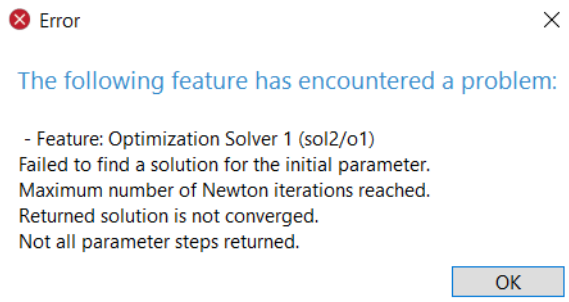

Figure 6.5: The error obtained when exceeding the maximum pressure load of 1×10^7Pa for the Neo-Hookean model

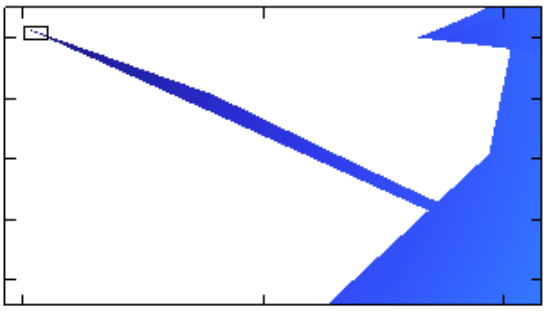

Figure 6.6: The displacement in the analysis of the first TO iteration of the Neo-Hookean model for an input pressure load of 5×10^7 Pa

For the Neo-Hookean model, deformations remain small for input pressure loads up to 1×10^6 Pa, yielding outcomes similar to the linear model. However, large displacements occur when the input pressure load exceeds this input pressure load. The design output from the Neo-Hookean model under an input pressure load of 1×10^7 Pa is visualised in Figure 6.4b. High input pressure loads large displacements, challenging the accuracy of the linear model in describing the behaviour of the system. Consequently, differences emerge between the designs obtained from the linear and Neo-Hookean models.

To accentuate the distinctions under high pressure load, a visual comparison between the linear and Neo-Hookean models is presented in Figure 6.7. In this figure, the red design signifies the filtered design of the linear model, while the grey design represents the filtered design of the Neo-Hookean model. Furthermore, Figure 6.8 illustrates the working principle of the design obtained from the linear model under an applied load of 1×10^6 Pa of a PA inverter.

The concept introduced in Subsection 5.2.3, specifically addressing TO with the Neo-Hookean material model, potentially accounts for the observed differences in the two designs in this case. However, the distinct rotation point is not visible in the designs obtained from the linear TO; hence, this remains a matter of speculation.

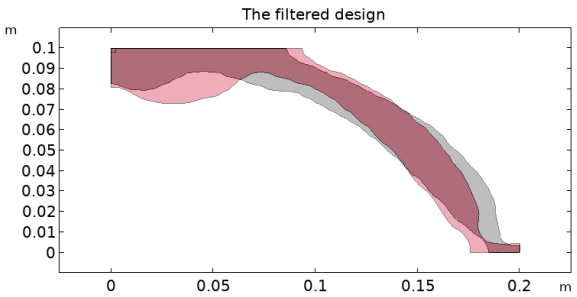

Figure 6.7: The difference between the obtained designs of the linear (red) and Neo-Hookean (grey) model of the PA inverter under an input pressure load of 1×10^7 Pa.

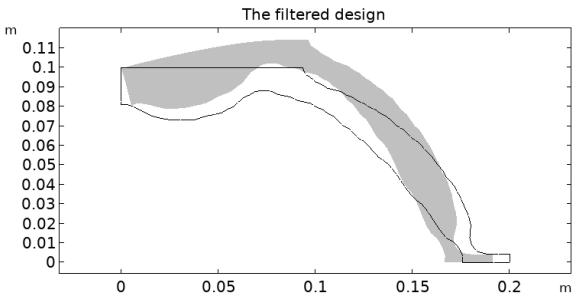

Figure 6.8: The deformed design obtained from the linear model under an applied pressure load of 1×10^6 Pa serves to validate the working principle of a PA inverter. The displacement is scaled by a factor of 8.

In Figure 6.9, the correct implementation of the Darcy method is demonstrated, and pressure leakages are absent. The figure illustrates the pressure field for the results obtained from both the linear model, as shown in Figure 6.9a, and a Neo-Hookean material model, as demonstrated in Figure 6.9b. The black line within the subfigures corresponds to the contour line of the filtered design presented in Figure 6.7, offering insights into how pressure load varies within the designs depicted in Figure 6.3 and Figure 6.4. It can be observed from Figure 6.9, Figure 6.3, and Figure 6.4 that the pressure load drops at the boundary where the design variables are approximately 0.6 or higher. This observation aligns with the findings presented in Subsection B.5.

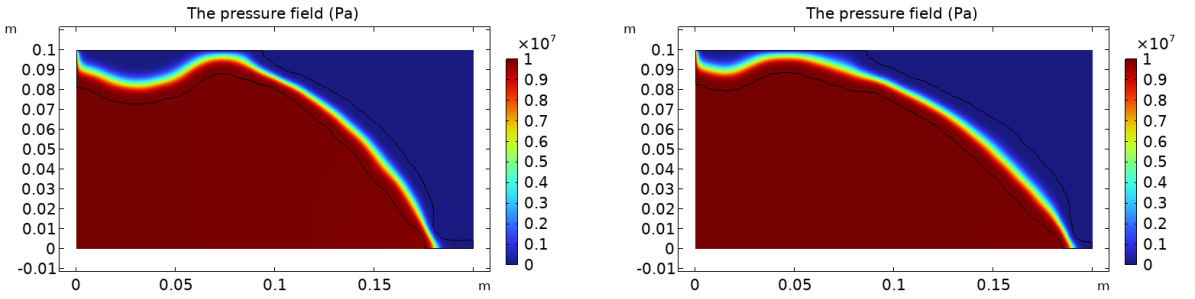

(a) The linear model

(b) The Neo-Hookean model

Figure 6.9: The pressure field of the obtained result of the linear (a) and Neo-Hookean (b) model of an PA inverter under an input pressure load of 1×10^7 Pa

6.1.1. The deformation-independent load analysis

In this case, the displacements obtained from the deformation-independent load analysis are larger for the design obtained from the analysis of the Neo-Hookean model, especially under input pressure loads higher than 1×10^6 Pa, compared to the linear model. Moreover, the difference between the expected displacements obtained from the Neo-Hookean model and the displacements from the analysis is smaller than the linear material model. This suggests that the Neo-Hookean model offers a more reliable prediction of displacements, particularly under high input pressure loads.

To visually illustrate these findings, Figure 6.10 presents the displacements obtained from the deformation-independent load analysis and the expected displacements obtained from both the linear and Neo-Hookean model under various values of the applied load. It is evident from this figure that up to an input pressure load of 1×10^6Pa, the displacements obtained from the deformation-independent load analysis for the linear and Neo-Hookean models are similar. However, at higher pressure loads, the Neo-Hookean model exhibits larger displacements. Specifically, for an input pressure load of 5×10^6 Pa, the displacement obtained from the Neo-Hookean model analysis is 20% larger than that of the linear model and for an input pressure load of 1×10^7 Pa, this difference increases to 30%.

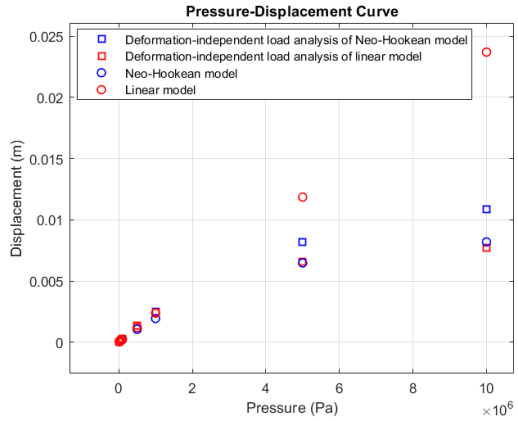

Figure 6.10: The displacements obtained from the deformation-independent load analysis and the expected displacements from the linear and Neo-Hookean model under different input pressure loads values for a PA inverter.

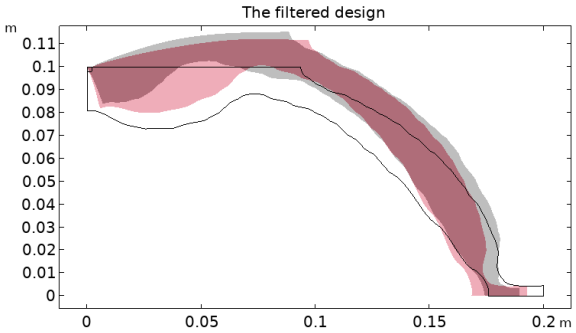

Figure 6.11: The difference between the displacements obtained from the deformation-independent load analysis of the linear (red) and a Neo-Hookean (grey) model under an input pressure load is 1×10^7Pa.

In Figure 6.11, the deformed designs resulting from an input pressure load of 1×10^7 Pa are depicted for both the linear (red) and Neo-Hookean (grey) models. It becomes clear that the deformation for the analysis of the Neo-Hookean model is larger than the linear model for this specific input pressure load. This figure aims to provide an intuition of the displacement expected in the mechanism under this pressure load and the magnitude of the obtained displacements.

Surprisingly, the displacements obtained from the deformation-independent load analysis of the linear model exhibit a better alignment than expected with those derived from the Neo-Hookean model. However, a substantial difference emerges between the expected displacement from the linear model and the actual displacement obtained in the deformation-independent load analysis. This difference is illustrated in Figure 6.10, where the red circle represents the expected displacement of the linear model, and the red square represents the displacement obtained from the deformation-independent load analysis under a specific input pressure load. As the input pressure load increases, the gap widens between the red square and circle, indicating that the predictive accuracy of the linear model decreases with a higher input pressure load.

In contrast, the difference between the expected displacement of the Neo-Hookean model (depicted by the blue circle) and the displacement observed in the deformation-independent load analysis (represented by the blue square) shows better behaviour. While the gap between the blue circle and square does increase with higher loads, it is noteworthy that the Neo-Hookean model demonstrates a more gradual change. In contrast to the linear model, the Neo-Hookean model exhibits a significantly smaller change in the gap, suggesting that it maintains its predictive accuracy better as the input pressure load increases. This highlights its enhanced performance in predicting displacements compared to the linear model.

6.1.2. The follower force analysis

In the follower force analysis, the pressure load is directly applied to the relevant boundary of the filtered design obtained from the TO. Within COMSOL, an applied pressure load becomes deformation-dependent when integrating a Neo-Hookean material model in solid mechanics. This is in contrast to the deformation-independent load analysis, where applied pressure loads are considered independent of the deformation. The findings indicate that adding such a pressure load does not significantly influence the obtained displacements. Moreover, incorporating the Neo-Hookean model has a considerably more significant impact than the follower pressure load. These conclusions hold for the specific case with the chosen parameters.

To illustrate, Figure 6.12 presents a comparison between the displacements obtained from the follower force analysis and the deformation-independent load analysis of both the linear and Neo-Hookean models. It can be observed from this figure that the displacements obtained from the deformation-independent load analysis are slightly larger compared to the displacements obtained from the follower force analysis for both the linear and Neo-Hookean models.

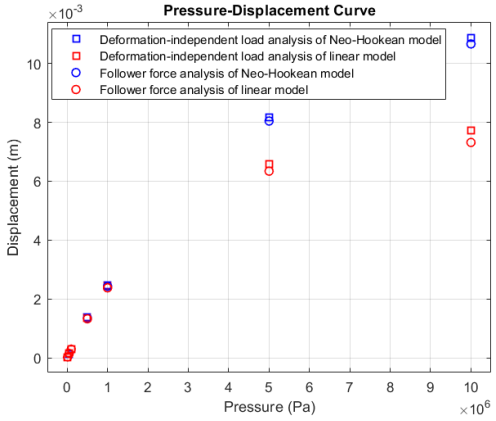

Figure 6.12: The displacements obtained from the follower force analysis and the deformation-independent load analysis of the linear and Neo-Hookean model under different input pressure load values for a PA inverter.

6.2. Pressure-actuated compliant gripper

The results of the TO of a PA compliant gripper are presented in this section, and the schematic visualisation is illustrated in Figure 6.13. This figure shows the symmetric half of the design domain and its boundary conditions. The Young's modulus for the solid and void regions are similar to Section 6.1. Notably, each set of results is derived from one hundred iterations using GCMMA, indicating that the TO has likely reached convergence. The objective function is the minimisation of the ratio of Δ to total strain energy. Here, Δ represents the displacement in the y-direction, as shown in Figure 6.13.

The results of a PA compliant gripper under input pressure loads of 1×10^6 Pa and 1×10^7 Pa are depicted in two figures. Figure 6.3 illustrates the outcomes based on the linear model, while Figure 6.4 presents the results from the Neo-Hookean model. These figures visually represent the material distribution in the gripper obtained through the TO.

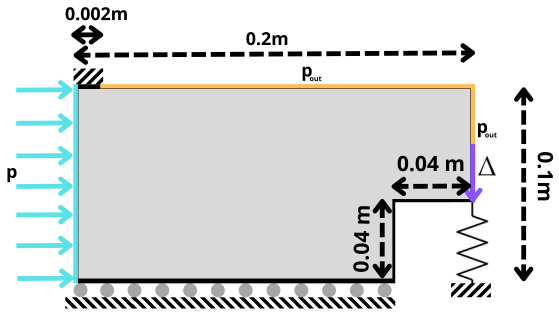

Figure 6.13: The schematic visualisation and the corresponding boundary condition of a PA compliant gripper.

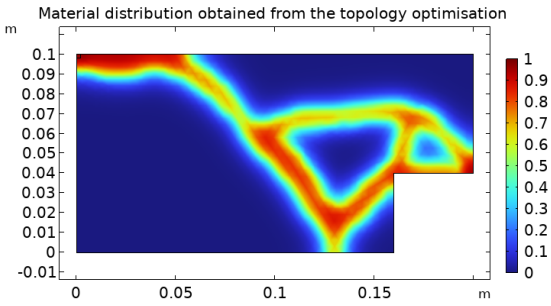

(a) Input pressure load of 1×10^6 Pa

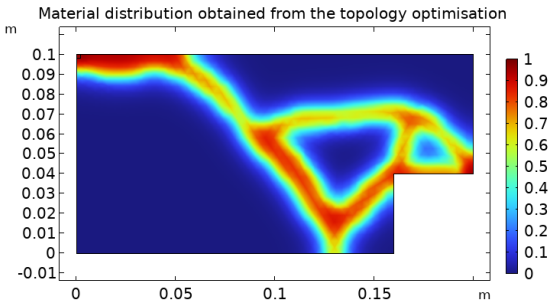

(b) Input pressure load of 1×10^7 Pa

Figure 6.14: The material distribution obtained from the linear model of a PA compliant gripper under two different input pressure load values.

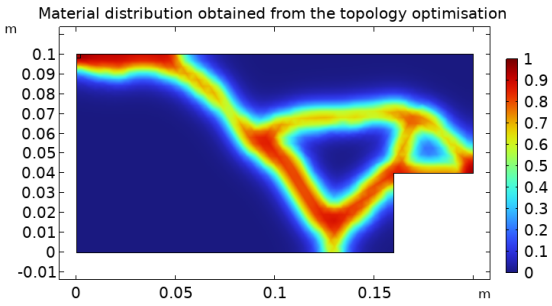

(a) Input pressure load of 1×10^6 Pa

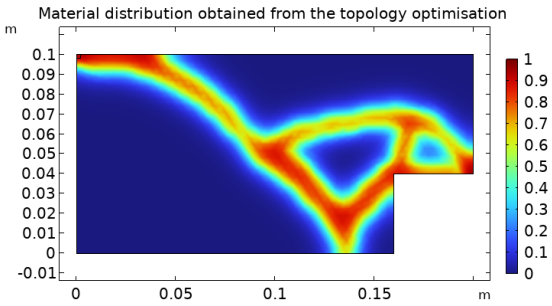

(b) Input pressure load of 1×10^7 Pa

Figure 6.15: The material distribution obtained from the Neo-Hookean model of a PA compliant gripper under two different input pressure load values.

For the Neo-Hookean model of a PA compliant gripper, the allowable input pressure load is 1×10^7 Pa; convergence cannot be achieved beyond this threshold. As illustrated in Figure 6.5, a similar error occurs, and its cause is explained in Section 6.1.

A comparable behaviour is observed in comparison to the PA inverter. Input pressure loads equal to or below 1×10^6 Pa induce small deformations, leading to outcomes similar to those of the linear model, as depicted in Figure 6.14a and Figure 6.15a. However, for input pressure loads higher than 1×10^6 Pa, the design changes due to the occurrence of large displacements, as shown in Figure 6.15b. The comparison between the linear and Neo-Hookean models is highlighted in Figure 6.16 at a maximum input pressure load of 1×10^7 Pa. Figure 6.17 illustrates the working principle of the design obtained from the Neo-Hookean model under an applied pressure load of 1×10^6 Pa of PA compliant gripper.

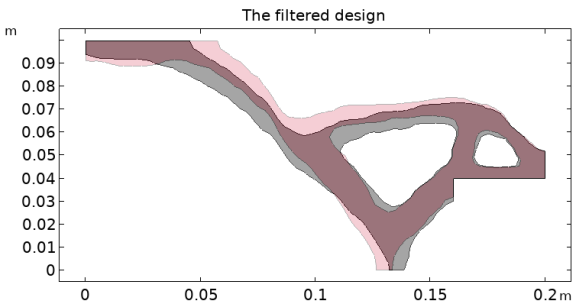

Figure 6.16: The difference between the obtained designs of the linear (red) and Neo-Hookean (grey) models of a PA compliant gripper under an input pressure load of 1×10^7 Pa.

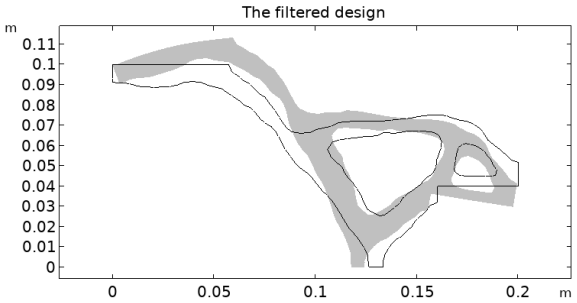

Figure 6.17: The deformed design obtained from the linear model under an applied pressure load of 1×10^6 Pa to validate the working principle of a PA compliant gripper. The displacement is scaled by a factor of 5.

In Figure 6.18, the correct implementation of the Darcy method is demonstrated; however, pressure leakage occurs in the bottom-right corner (the light red area) of the subfigures. The figure illustrates the pressure field for results obtained from both the linear model, as shown in Figure 6.18a, and a Neo-Hookean material model, as demonstrated in Figure 6.18b.

The black line within Figure 6.9 corresponds to the contour line of the filtered design presented in Figure 6.16, offering insights into how pressure load varies within the designs depicted in Figure 6.14 and Figure 6.15. Observations from Figure 6.18, Figure 6.14, and Figure 6.15 reveal that the pressure load drops at the boundary where the design variables are around 0.6 and higher, consistent with the findings of Subsection B.5.

However, a pressure leakage is observed at the bottom where the design variables have a value of 0.5. The slow pressure drop, associated with the design variable at 0.5, eventually leads to leakage. An interesting observation is made in Figure 6.19, where two spots circled in black have similar values for the design variables. Surprisingly, pressure leakage occurs only at the lower circle and not at the top circle, deviating from the expected behaviour.

The drainage term, expressed in Equation 3.3, regulates the prevention of pressure penetration into the material. A parameter study was conducted to explore the impact of η_h and β_h, the parameters of the drainage equation. Unfortunately, altering these values did not resolve the leakage problem. Additionally, the number of iterations was increased from 100 to 400, resulting in similar results as observed in Figure 6.18.

Furthermore, the mesh was refined into smaller elements, as illustrated in Figure 6.20. This figure shows a slight improvement in pressure leakage with the decreasing mesh size but does not completely resolve the issue. However, the computational time increased from around 15 to approximately 70 minutes. The investigation to find a solution for the pressure leakage is left to the recommendations.

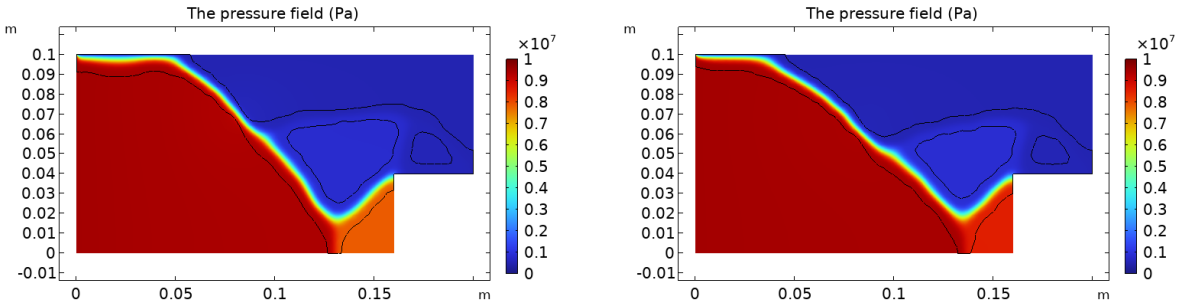

(a) The the linear model

(b) The Neo-Hookean model

Figure 6.18: The pressure field of the result of the linear (a) and a Neo-Hookean (b) model of a PA compliant gripper under an applied force of 1×10^7 Pa

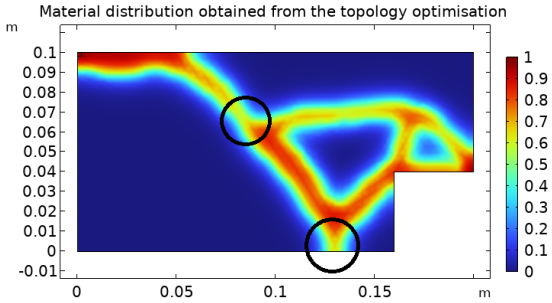

Figure 6.19: The material distribution obtained from a Neo-Hookean model of a PA compliant gripper under an input pressure load of 1×10^7Pa with two areas circled. These circled areas illustrate areas with similar values for the design variables.

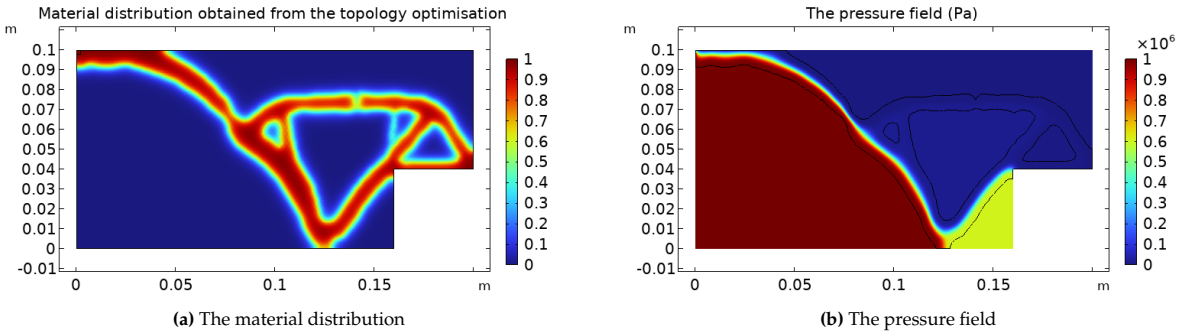

(a) The material distribution

(b) The pressure field

Figure 6.20: (a) The material distribution of the linear model of PA compliant gripper under an input pressure load of 1×10^7 Pa with a mesh containing a maximum element size of 0.002 m. (b) The corresponding pressure field.

6.2.1. The deformation-independent load analysis

Incorporating the Neo-Hookean material model in the solid mechanics of the TO results in larger displacements in the deformation-independent load analysis for the given parameters. Despite pressure leakage, this leads to a more optimised objective function. This behaviour implies that the influence of pressure leakage is negligible in this case. Additionally, the Neo-Hookean model provides reliable predictions of displacements, particularly under high input pressure loads, compared to the linear model.

These findings are visualised in Figure 6.21, illustrating displacements obtained from the deformation-independent load analysis and the expected displacements from both the linear and Neo-Hookean models under various values of the applied load. Similar to Figure 6.10, the displacements obtained from the deformation-independent load analysis of the linear and Neo-Hookean model are comparable for input pressure loads equal to or lower than 1×10^6 Pa. However, the Neo-Hookean model outperforms the linear model for higher input pressure loads. Specifically, for an input pressure load of 4×10^6 Pa, the displacement obtained from the Neo-Hookean model analysis is 17% larger than the linear model. In contrast, for an input pressure load of 1×10^7 Pa, this difference increases to 30%.

In Figure 6.22, the results of the deformation-independent load analysis of the linear (red) and Neo-Hookean (grey) models of the PA compliant gripper under an input pressure load of 1×10^7 Pa are shown. This visual representation aims to give the reader an intuition of the displacement magnitudes and highlight the differences between the linear and Neo-Hookean models.

Furthermore, the displacements obtained from the deformation-independent load analysis of the linear model align better than expected with those from the analysis of the Neo-Hookean model. Nevertheless, the difference between the displacement obtained from the deformation-independent load analysis of the linear model (the red square) and the expected displacement of the linear model (the red circle) increases with the increasing pressure load. This behaviour indicates that, in this case, the linear model cannot accurately predict displacements for high loads.

What is remarkable is the almost perfect alignment between the displacements obtained from the deformation-independent load analysis and the expected displacements from the results of the Neo-Hookean model. Note that there is still a marginal difference between the two displacements. These findings highlight that, despite the pressure leakage in the design, the Neo-Hookean model accurately predicts displacements, suggesting the influence of pressure leakage is minimal.

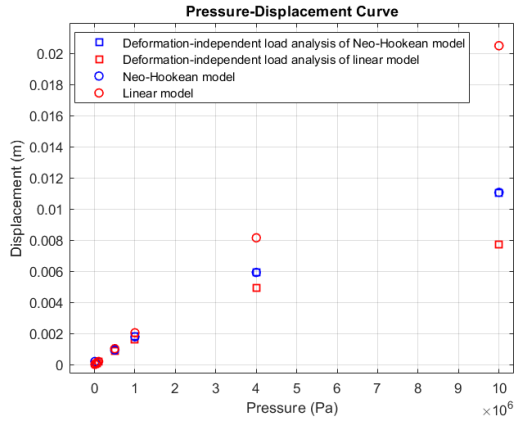

Figure 6.21: The displacements obtained from the deformation-independent load analysis and the expected displacements from the linear and Neo-Hookean model of a PA compliant gripper under different input pressure load values.

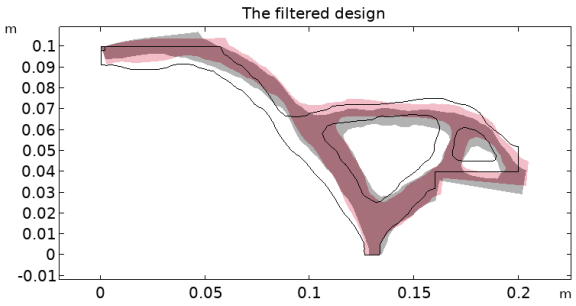

Figure 6.22: The difference between the displacements obtained from the deformation-independent load analysis of the linear (red) and a Neo-Hookean (grey) model under an input pressure load is 1×10^7Pa.

6.2.2. The follower force analysis

In this scenario, applying a pressure load which is dependent on the deformation does not significantly alter the obtained displacements with the specified parameters. In contrast, integrating the Neo-Hookean material model has a more significantly effect on the objective function. This conclusion aligns with the findings presented in Subsection 6.1.2 and is evident from Figure 6.23. The figure illustrates that the displacements from the follower force analysis show slight differences compared to the deformation-independent load analysis of the linear and Neo-Hookean models.

6.3. A member of the pneumatic networks

This section presents the design of a member of the PneuNets, which is an extension of the work of Kumar (2023). A PneuNets is a soft actuator consisting of a series of chambers that achieve motion through pressurised fluid flows (Liu et al. 2020). An illustrative example of a PneuNets member is shown in Figure 1.1 of the introduction, where pressurised fluid flows through the chambers, enabling tasks such as picking up an egg.

The investigation into PneuNets is motivated by the pressure load they exhibit, differing from traditional PA inverters and compliant grippers. Unlike the latter, where pressure load is typically applied from the outside, a member of the PneuNets experiences an internal pressure load. This section aims to understand how PACMs respond to internal pressure loads in conjunction with geometric nonlinearities and a Neo-Hookean material model, providing deeper insights into the design of PA soft robots.

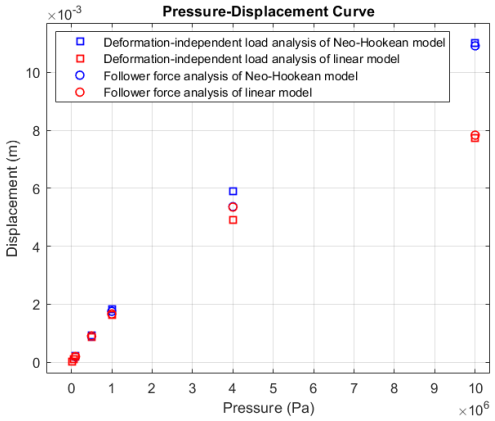

Figure 6.23: The displacements obtained from the follower force analysis and the deformation-independent load analysis of the linear and Neo-Hookean model under different input pressure load values for a PA compliant gripper.

The schematic visualisation of a PneuNets member is provided in Figure 6.24. The Young's modulus for solid regions E_1 equals $100 \times 10^6 \mathrm{N/m^2}$, while the Young's modulus for void regions E_0 equals $E_1 \times 10^{-6}$. In this model, parameters η_k and η_h are set to 0.2 and 0.3, respectively. The optimisation process involves fifty iterations using GCMMA, suggesting that the TO has likely reached convergence. The objective function aims to minimise the ratio of Δ to the total strain energy, where Δ represents the displacement in the y-direction, as illustrated in Figure 6.24.

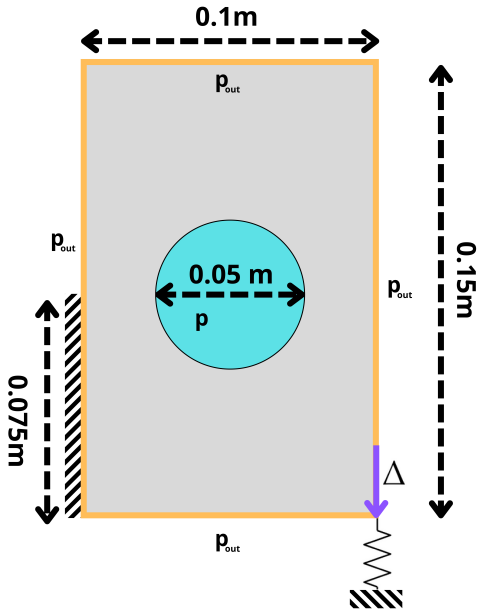

Figure 6.24: The schematic visualisation of a member of a PneuNets

From this study, it can be concluded that modelling a PneuNets member with the Neo-Hookean model in COMSOL is feasible. However, limitations restricting the maximum input pressure load have resulted in small deformations, preventing conclusions regarding the influence of the Neo-Hookean model.

Figure 6.25a and Figure 6.25b illustrate the material distribution and pressure field obtained from the Neo-Hookean model under an input pressure load of 1×10^5 Pa. The latter figure validates the correct implementation of the Darcy method and confirms the absence of pressure leakage. An input pressure load of 1×10^5 Pa is the maximum input pressure load achievable for this case. The black line in Figure 6.25b corresponds to the contour line of the filtered design shown in Figure 6.26a. This line serves the same purpose and draws the same conclusion as discussed in Section 6.1 and Section 6.2.

The difference between the designs obtained from the linear and Neo-Hookean models is subtle and insignificant; therefore, the results obtained from the linear model are omitted. The marginal difference can be attributed to the low input pressure load, resulting in small displacements. As discussed in Section 6.1, the linear model is accurate enough to design and describe the behaviour of the PneuNets member for this specific input pressure load.

The limitation of the low maximum input pressure load arises from the excessive deformation observed in the analysis of the initial iterations of the TO, leading to the error depicted in Figure 6.5. A detailed explanation of this behaviour is provided in the discussion (Chapter 7).

Lastly, Figure 6.26a illustrates the working principle of a component obtained from the Neo-Hookean model under an input pressure load of 1×10^5 Pa of a member of the Pneunets system. The figure reveals that the system undergoes relatively large deformation to achieve minimal displacement in the y-direction at the bottom-right corner, contrary to expectations. This unexpected behaviour prompted an investigation to identify its cause. The investigation revealed that the stiffness of the output spring k_{ss} was a limiting factor, hindering the desired deformation in that specific direction. In Figure 6.26b, the displacement of the modified design with k_{ss} set to 1×10^3 N/m is presented, resulting in the desired displacement in the y-direction. However, determining the correct value for k_{ss} depends on the application. Such a study is beyond the scope of this thesis, and further investigation is required to identify the stiffness necessary for the application.

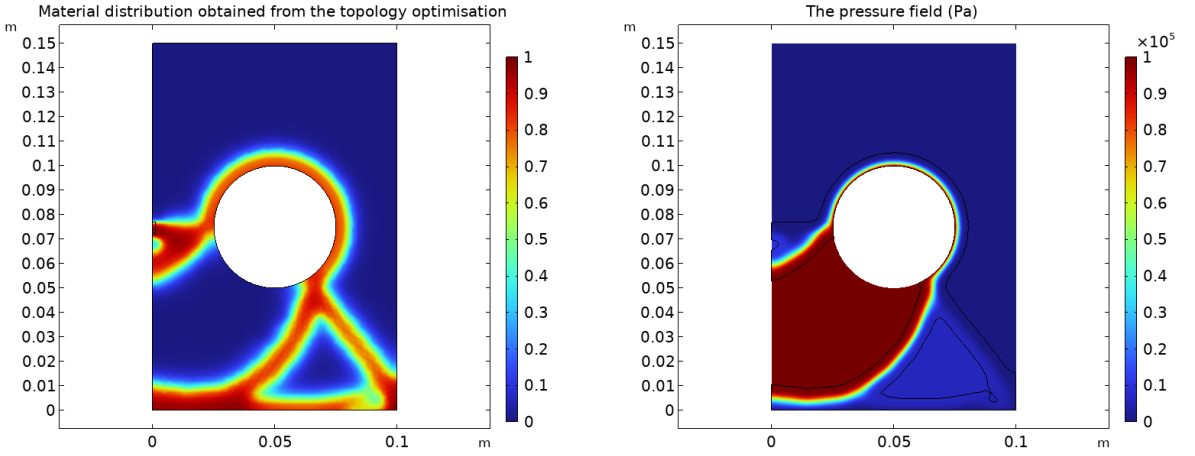

(a) The material distribution

(b) The pressure field

Figure 6.25: The material distribution (a) and pressure field (b) obtained from the Neo-Hookean model of a member of the PneuNets under an input pressure load of 1×10^5 Pa

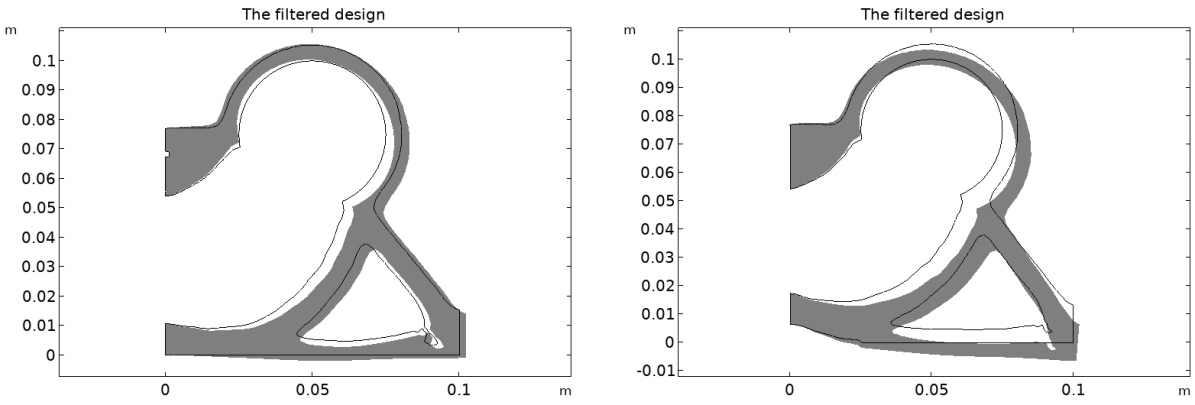

(a) $k_{ss} = 1 \times 10^4$ N/m. The displacement is scaled by a factor of 3.

(b) $k_{ss} = 1 \times 10^3$ N/m. The displacement is scaled by a factor of 3

Figure 6.26: The deformed design obtained from the Neo-Hookean model under an input pressure load of 1×10^5 Pa with different values for k_{ss}

6.4. Multi-material pressure-actuated compliant gripper

This section demonstrates the results of the multi-material PA compliant gripper. The schematic visualisation and its boundary condition are identical to Figure 6.13. However, the modified SIMP formulation for the two-material case is used in this model and can be expressed as shown in Equation 6.1, which is obtained from Sigmund and Torquato (1997).

$$E = (1 - \bar{\rho}_{i1}^{p}) * E_0 + \bar{\rho}_{i1}^{p}[(1 - \bar{\rho}_{i2}^{p})E_1 + \bar{\rho}_{i2}^{p}E_2] \tag{6.1}$$

In this equation, the variable $\bar{\rho}i1$ represents the local density determining whether an element becomes void ($\bar{\rho}_{i1} = 0$) or solid ($\bar{\rho}_{i1} = 1$). The variable $\bar{\rho}_{i2}$ is the 'mixture coefficient,' where $\bar{\rho}_{i2} = 0$ indicates pure material 1, and $\bar{\rho}_{i2} = 1$ indicates pure material 2.

Material properties include a Young's modulus E_1 of 3×10^8 N/m^2 for the first material, E_2 of 3×10^9 N/m^2 for the second material, and E_0 of $E_1 \times 10^{-6}$ N/m^2 for void regions. The TO involved four hundred iterations using GCMMA, suggesting that the TO has likely reached convergence. The objective function aims to minimise the ratio of Δ to the total strain energy.

This section excludes the nonlinear model results due to poor performance, discussed in Section 6.1. Figure 6.27 shows the results obtained from the linear model of a multi-material PA compliant gripper. Figure 6.27a and Figure 6.27b illustrate the material distribution represented by $\bar{\rho}_{i1}$ and $\bar{\rho}_{i2}$, respectively. Similarly, Figure 6.28 depicts Neo-Hookean model results, with Figure 6.28a and Figure 6.28b showing $\bar{\rho}_{i1}$ and $\bar{\rho}_{i2}$ values, respectively.

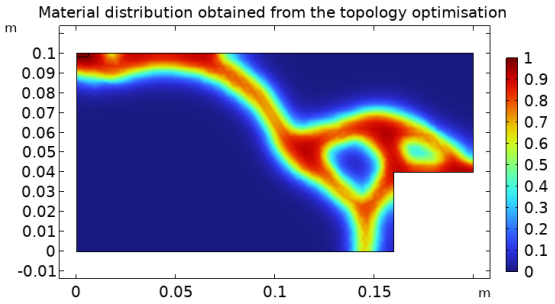

(a) The values for $\bar{\rho}_{i1}$

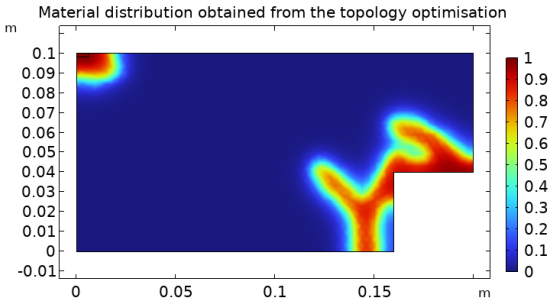

(b) The values for $\bar{\rho}_{i2}$

Figure 6.27: The obtained values for the design variables $\bar{\rho}_{i1}$ i.e. the material distribution (a) and $\bar{\rho}_{i2}$ (b) for the linear model of a multi-material PA compliant gripper under an applied pressure load of 5×10^5 Pa.

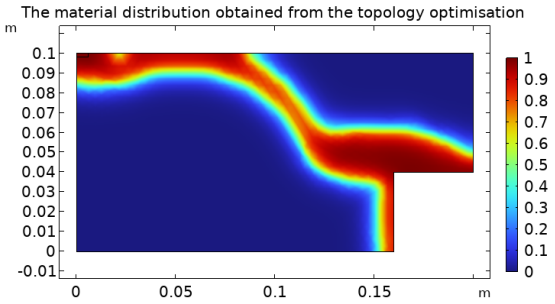

(a) The values for $\bar{\rho}_{i1}$

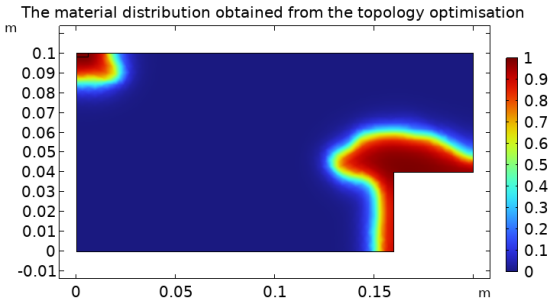

(b) The values for $\bar{\rho}_{i2}$

Figure 6.28: The obtained values for the design variables $\bar{\rho}_{i1}$ i.e. the material distribution (a) and $\bar{\rho}_{i2}$ (b) for the Neo-Hookean model of a multi-material PA compliant gripper under an applied pressure load of 5×10^5 Pa.

The conclusion regarding the multi-material PA compliant gripper aligns with that drawn for the PneuNets member. Incorporating the Neo-Hookean material model in the solid mechanics of the TO process in COMSOL is feasible. However, the allowable input pressure load is small, resulting in relatively moderate deformations. Moreover, the designs obtained between the linear and Neo-Hookean models exhibit significant differences. The correlation between the expected displacements obtained from the models and the significant distinctions between the obtained designs is expected to stem from the low stiffness of the materials with a Young's modulus E_1.

The results indicate that the Neo-Hookean model for a multi-material PA compliant gripper reaches its maximum load at 5×10^5 Pa. However, exceeding this limit results in a non-converge error, as depicted in Figure 6.5. The expected displacements for the linear and Neo-Hookean models are 0.002 m and 0.0023 m, respectively. This 16% difference is noteworthy, particularly when compared to the marginal difference observed in the (single-material) PA compliant gripper under the same input pressure.

This discrepancy is attributed to the lower stiffness in the solid regions compared to the single-material PA compliant gripper. In this scenario, the Neo-Hookean material model plays a more crucial role in accurately describing the behaviour of these softer materials, emphasising its substantial influence on the results obtained from the topology optimisation.

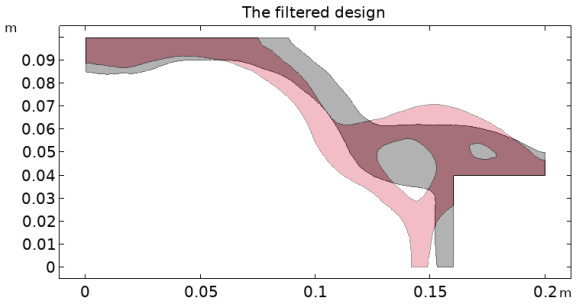

Figure 6.29: The difference between the obtained designs of the linear (green) and the hyperelastic (grey) model of a multi-material PA compliant gripper under an input pressure load of 5×10^5 Pa.

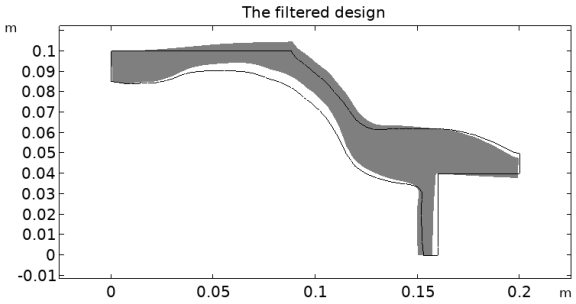

Figure 6.30: The deformed design obtained from the linear model under an applied pressure load of 5×10^5 Pa to validate the working principle of a multi-material PA compliant gripper. The displacement is not scaled

Pressure fields for the linear and Neo-Hookean models are presented in Figure 6.31a and Figure 6.31b, respectively. The black lines in Figure 6.31 correspond to contour lines of the filtered designs from Figure 6.29, serving the same purpose and drawing the same conclusion as discussed in Section 6.1 and Section 6.2. Similar to the PA compliant gripper, pressure leakages occur; however, for the linear model, the leakage is significantly larger than for the Neo-Hookean model. This difference can be attributed to differences in the designs. Additionally, the same investigation on pressure leakage has been conducted similarly to section 6.2, without success. The investigation to find a solution for the pressure leakage is left to the recommendations.

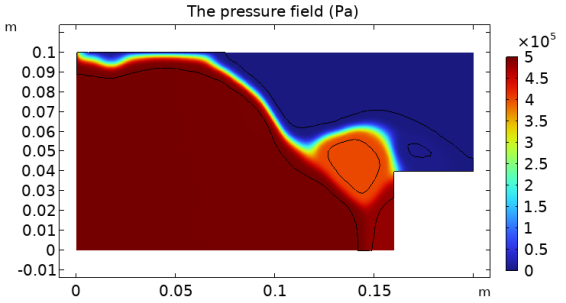

(a) The linear model

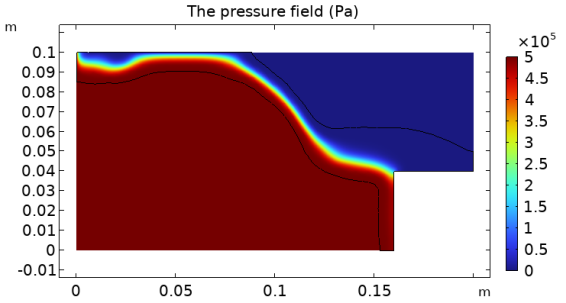

(b) The Neo-Hookean material

Figure 6.31: The pressure field obtained from the linear (a) and Neo-Hookean (b) model of multi-material PA compliant gripper under an input pressure of 5×10^5 Pa

7

Discussion

In Chapter 5, the Wang method is extensively discussed, which is tested in various cases by incorporating this interpolation method. The results presented in Chapter 6 extend and build upon the research conducted by Kumar, Frouws, et al. (2020), Kumar and Langelaar (2022), Pinskier, Kumar, et al. (2023), and Kumar (2023). Kumar, Frouws, et al. (2020) focused on the TO of PA structures and PACMs using the Darcy method. Similarly, Kumar and Langelaar (2022) developed a robust method for the TO of a PA inverter and PA gripper. Pinskier, Kumar, et al. (2023) investigated the TO of a multi-material PA compliant gripper, while Kumar (2023) designed a member of the PneuNets using TO. However, these papers do not account for nonlinearities. In contrast, our thesis extends these works by incorporating geometric nonlinearities and the Neo-Hookean material model in the solid mechanics of the TO process. In this chapter, the results and behaviour of both methods are discussed and put in perspective.

The Wang method
In our numerical experiments with our chosen parameters, we found that the Wang method effectively broadens the range of the maximum allowable applied load during the TO of a cantilever beam in COMSOL. However, this outcome is not replicated in the TO of CMs. These findings align with the conclusions drawn by Wang, Lazarov, Sigmund, and Jensen (2014), which primarily focused on the TO of solid structures. Unfortunately, their study does not provide any conclusive insights into the impact of the Wang method on the TO of CMs. Consequently, direct comparisons between our observations and their findings regarding the TO of CMs are limited.

Nevertheless, despite this alignment, differences exist between the results obtained from the TO of a cantilever beam in our study and those reported in the referenced paper. Specifically, incorporating a Neo-Hookean material model in our experiments limits the maximum applied load to 150 kN, whereas the Wang method permits a higher load of 250 kN. In contrast, the cited paper indicates that incorporating a Neo-Hookean material model limits the maximum applied load to 240 kN, while the Wang method allows for a higher load of 500 kN. We further investigated the root of these differences.

The difference between the results obtained in this thesis and the referenced paper can be partly explained by the absence of a density filter and projection on the design variables, along with a constant β_1 and penalisation factor p. Note that β_1 represents the steepness of the Heaviside function in the interpolation factor, signifying the transition between linear and nonlinear theory.

A problem occurs when incorporating the Helmholtz density filter with the Wang method in COMSOL. Attempts to combine this filter with the Wang method caused the optimiser to stall and subsequently stop. However, the model produced feasible results without the Helmholtz density filter. Furthermore, implementing a projection on the design variables led to a significant increase in computational time than the absence of the projection. As a result, the decision was made not to incorporate the projection on the design variables. The absence of the density filter and projection on the design variables contrasts with the model in the reference paper, where a linear density filter and projection were incorporated.

Moreover, in contrast to the model in the referenced paper, where β_1 and the penalisation factor p change throughout the iterations, in COMSOL, this is infeasible since implementing it is impossible. Consequently, β_1 and p remain constant throughout our model. While there are differences between our model and the referenced paper, these variations are not expected to solely account for the lower maximum applied loads observed in our results. The source of the remaining difference is still uncertain.

Additionally, the Wang method did not increase the maximum allowable applied load during the TO of an inverter. To investigate whether the Wang method was case-dependent, it was applied to various scenarios, including the TO of a compliant gripper, PA inverter, PA-compliant gripper, and PA member of the PneuNets. This examination aimed to observe its influence in different scenarios. Surprisingly, no improvement in the maximum applied load was observed with the Wang method in any of these cases, and the exact reason for this observation remains unknown.

It is peculiar that the Wang method effectively increased the maximum allowable input load for a structure while it showed ineffectiveness for CMs. The distinction between structures and CMs lies in the objective function. However, it is expected that this difference is not the cause for the ineffectiveness of the Wang method in our numerical experiments with CMs. This behaviour requires further investigation to identify the source. Future investigations may delve into integrating the Wang method with CMs, potentially expanding the range of applied loads. An effective Wang method could allow for the TO of CMs and PACMs under high-pressure loads.

The nonlinear topology optimisation of pressure-actuated compliant mechanisms
The findings of Chapter 6 show that implementing a Neo-Hookean material model in the solid mechanics of the TO process resulted in better values for the objective function compared to the linear elastic material model. These findings align with the expectations and confirm the findings of the paper of Kumar and Langelaar (2022). They performed an analysis incorporating geometric nonlinearities, a Neo-Hookean material model and follower force on the obtained design from the linear TO. They stated that it is crucial to incorporate the full nonlinear solid mechanics.

To explore the impact of applied pressure loads on the designs of the PA inverter and the PA compliant gripper, we examined the results obtained from the linear and Neo-Hookean models[1]. As expected, the displacements obtained from the deformation-independent load analyses exhibit similarities at low-pressure loads and start diverging as a higher-pressure load is applied. This deviation in results arises from the superior accuracy of the Neo-Hookean model when dealing with large deformations, especially under high loads.

It is noteworthy that in this study, the degree of deviation between both models remains relatively moderate. The application of higher pressure loads would have induced more large displacements, thereby providing a more pronounced illustration of the significant advantages associated with integrating the Neo-Hookean model as opposed to the linear model.

Another compelling contrast between the models emerges when comparing their expected and actual displacements obtained via the design-independent load analysis. Significantly smaller differences are observed in the Neo-Hookean model, underscoring again its enhanced predictive accuracy.

Furthermore, the similarities in displacements observed during both follower load and deformation-independent analyses across both models underscore the distinctive influence of incorporating the Neo-Hookean material model in the TO process. This observation implies that incorporating the follower force does not exert the anticipated substantial influence. Readers may contend that the observed displacements are not large enough to yield a significant difference. Therefore, as discussed earlier, higher pressure loads would have induced more large displacements, offering a clearer illustration of the advantages of integrating a deformation-dependent pressure load.

[1]The reader should note that referring to the Neo-Hookean model signifies the model with the Neo-Hookean material model and geometric nonlinearities incorporated into the solid mechanics of the TO process. This also holds for the linear model, where a linear elastic material model is incorporated into the solid mechanics of the TO process.

The Neo-Hookean model in COMSOL presents notable challenges, particularly when subjected to high-pressure loads during the TO process. Difficulties arise beyond a specific pressure load threshold, leading to excessive displacements and, consequently, a failed analysis. This limitation on input pressure loads is attributed to the inherently low Young's modulus resulting from the initial values of the design variables during the initial TO iterations. The consequence of this low Young's modulus is the excessive deformation of the mechanism under high-pressure loads, introducing complexities that, at this point, remain unspecified.

Figure 7.1 illustrates an example of excessive displacements during the TO of a member of the PneuNets under an input pressure load of 5×10^5 Pa. Normally, displacements are large in the first iterations and gradually reduce as more material is added, as illustrated in Figure 7.2. However, when the displacements become excessive, their reduction becomes challenging, leading to the failure of the analysis.

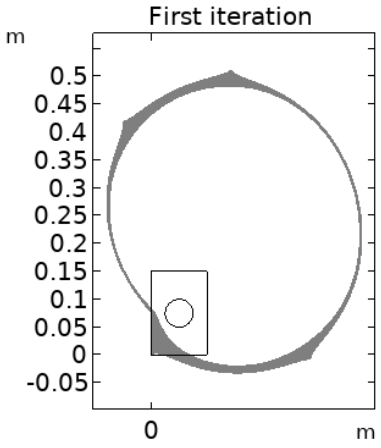

Figure 7.1: The displacement of the analysis before the first TO iteration of the Neo-Hookean model for a member of the Pneunets under a pressure load of 5×10^5 Pa

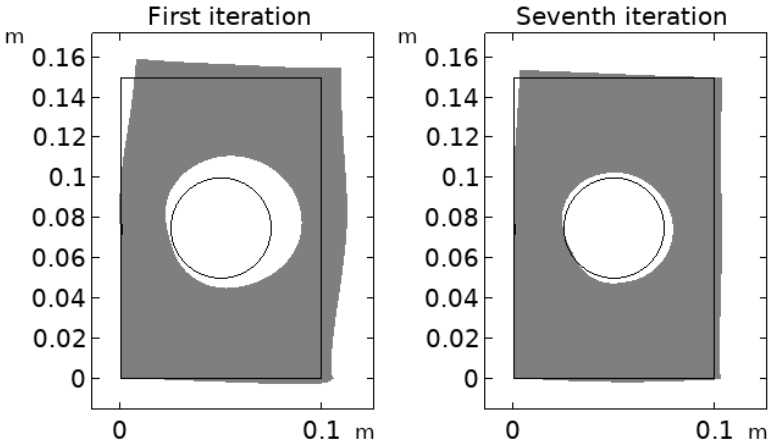

(a) The displacement of the first TO iteration **(b)** The displacement of the seventh TO iteration

Figure 7.2: The displacement of the analysis for the first (a) and seventh (b) TO iteration of the Neo-Hookean model for a member of the PneuNets under a pressure load equal to 1×10^5 Pa.

Changing the initial values assigned to the design variables does not resolve the issue. The values of the design variable in the first TO iterations converge to a value close to the volume fraction for all elements. Upon reaching this value, the design process of the CM is initiated. However, extensive displacements are already obtained before this design process can start, and the analysis will fail.

Constraints within COMSOL impose several limitations on the results, particularly in applying high-pressure loads to the designs. One notable constraint is the absence of force continuation throughout all TO iterations. Force continuation should be distinguished from load ramping, where the load is incrementally increased, to find a solution for the nonlinear solver.

Excessive deformation can be prevented by implementing force continuation over the entire TO iteration, which can potentially extend the range of maximum applied pressure loads. In the initial TO iterations, structures experience relatively low-pressure loads. This phase allows the optimiser to establish a material distribution with $0/1$ values for the design variables. Subsequently, when the complete load is applied, the design showcases improved resistance to high loads due to the already evolved material distribution. Additionally, these continuations have been employed in existing literature, as seen in Wang, Lazarov, Sigmund, and Jensen (2014) and Kumar, Frouws, et al. (2020). Therefore, implementing them addresses the limitations and makes it easier to compare with existing research.

8

Conclusions and recommendations

Thesis aim and research questions
This thesis aims to resolve the discrepancy observed when employing a linear model for designing PA soft robots by introducing methods to account for nonlinearities. The linear models lack accuracy in representing the behaviour of PA soft robots due to large deformations, low-stiffness materials, and deformation-dependent pressure loads. When describing the behaviour of PA soft robots using a linear model, the results may differ from the actual behaviour. Minimising this difference effectively reduces the identified gap between model results and empirical behaviour.

Geometric nonlinearities and a Neo-Hookean material model are incorporated to reduce this gap. In this thesis, three research questions are formulated: **1)** To what extent can geometric nonlinearities and a hyperelastic material model be incorporated into the solid mechanics of the topology optimisation process for design-dependent pressure-actuated soft robots in COMSOL? **2)** How does integrating geometric nonlinearities and a hyperelastic material model influence the design and behaviour of design-dependent pressure-actuated soft robots in COMSOL? **3)** What techniques can be employed to improve the range of maximum applied pressure load for the topology optimisation for design-dependent pressure-actuated soft robots, incorporating geometric nonlinearities and a hyperelastic material model in the solid mechanics?

Conclusions
1) This study concludes that the combination of the Darcy method with geometric nonlinearities and the Neo-Hookean material model has been successfully implemented, as demonstrated with the PA inverter and PA compliant gripper. The PA PneuNets member and multi-material PA compliant gripper also successfully implemented geometric nonlinearities and a Neo-Hookean material model; however, these cases are limited to low-input pressure loads. Nevertheless, there are limitations on the range of the maximum allowable pressure load that can be applied. These limitations arise from the excessive displacements obtained in the initial TO iterations, leading to a failed analysis. The maximum applied pressure load for the PA inverter is 1×10^7 Pa, similar to the PA compliant gripper. For the PA Member of the PneuNets, this pressure load is 1×10^5 Pa, while for the multi-material PA compliant gripper, it is 5×10^5 Pa.

2) The designs obtained from the Neo-Hookean model of the PA inverter and the PA compliant gripper exhibit significant differences under high-pressure loads. Under low-pressure loads, the designs are similar to those from the linear model. Due to pressure load limitations for the PneuNets member, the design obtained from the Neo-Hookean model shows insignificant differences compared to the design obtained from the linear model. In contrast, the multi-material PA compliant gripper, subjected to low-pressure loads, exhibits a significant difference between the designs obtained from the Neo-Hookean and linear models.

Additionally, the Neo-Hookean model yields a better objective function than the linear model, especially under high-pressure loads for the PA inverter and PA compliant gripper. Due to the significant pressure load limitations for the PA member of the PneuNets and the multi-material PA compliant gripper, no definitive conclusions can be drawn for these two cases.

3) The Wang method, introduced in the paper of Wang, Lazarov, Sigmund, and Jensen (2014), proves ineffective in increasing the maximum allowable pressure load when combined with the TO of a CM for the specific case with the chosen parameters in COMSOL. The initial aim of implementing the Wang method was to extend the maximum applied load, allowing for larger displacements, as the Wang method addresses the distortion of the void elements. Combining the Wang method with the TO of structures results in a higher maximum applied load. However, this increased load is not observed when implementing the Wang method with the TO of a CM.

Recommendations
Building upon the advancements in this study, several possibilities present themselves for future work for further optimisation of PA soft robots. These recommendations are discussed here.

The first recommendation involves introducing a Helmholtz filter and a projection on the design variables. In the considered COMSOL environment, the Wang method is found effective for increasing the maximum allowable load exclusively for the TO of structures without a Helmholtz density filter and a projection. However, their implementation poses significant challenges, resulting in warnings that cause the analysis to stall and eventually stop. The challenges encountered during implementation suggest a potential connection to the diverging behaviour of the Newton-Raphson method, indicated by warnings urging a reduction in the step size. While the cause of these problems remains unknown, a thorough investigation is recommended to identify a solution.

As a solution, a segregated approach was employed instead of a fully coupled approach to investigate the impact, but no improvements were observed. Additionally, different nonlinear solvers, specifically the Quasi-Newton Raphson and Double Dogleg methods, were employed, yet this also did not lead to improvements. Although fine-tuning the Double-Dogleg solver holds the potential for better results, this remains a recommendation for future exploration. In parallel, as an alternative solution, the potential utilisation of a Helmholtz filter as a PDE in COMSOL was considered. However, this approach proved infeasible due to required changes in the interface of the TO module. Consequently, further investigation is crucial for addressing the challenges that result in a stalling analysis and for enabling the integration of a Helmholtz filter and a projection into the method, thereby enhancing the efficacy of the Wang method.

Despite the absence of the Helmholtz filter and the projection on the design variables, implementing the Wang method is still recommended for designing structures under high applied loads using TO. It significantly increases the range of applied pressure loads for structures. While its effectiveness for CMs is currently limited, the anticipated enhancement in the applied pressure load range is hindered by the diverging behaviour of the Newton-Raphson method. Further research is recommended to address this limitation and enable the compatibility of the Wang method with the TO of CMs, potentially unlocking a broader range of applied pressure loads.

The second recommendation involves the implementation of the deformation-dependent pressure loads (follower forces) and boundary nonlinearities in the solid mechanics of the TO process for PACMs. While minor differences exist between the displacements obtained in the deformation-independent load and follower force analyses, the incorporation of a deformation-dependent pressure load in the solid mechanics of the TO process is anticipated to yield significant differences, particularly under high-pressure loads. Therefore, accounting for these nonlinearities in the TO formulation is essential, as emphasised by Kumar and Langelaar (2022). It is recommended to start incorporating the follower force, given its universal importance, while boundary nonlinearities play a crucial role in specific cases. It is noteworthy that in COMSOL, the pressure loads that arise with nonlinearities are treated as follower forces; however, these pressure loads are not design-dependent during the TO. Therefore, it is imperative to investigate and find a solution to incorporate design-dependent deformation-dependent pressure loads during the TO.

The third recommendation involves addressing the challenge of excessive displacements during the initial TO iterations under high-pressure loads. Two approaches could be considered to tackle this issue. The first approach involves the implementation of continuation. Currently, COMSOL does not support the implementation of continuation over the iterations, imposing limitations on numerical experiments.

As an alternative, the COMSOL-MATLAB LiveLink offers a solution where continuation is feasible. Within this LiveLink, the TO is executed in MATLAB, while solid mechanics and sensitivities are computed in COMSOL. Additionally, this LiveLink allows the combination of the Wang method with a linear density filter. It is important to note that users need a solid understanding of the MMA solver in MATLAB and the link between COMSOL and MATLAB. Despite the drawback of increased computational time for obtaining results, this approach is an alternative.

For future research, exploring this possibility could potentially resolve the excessive displacement observed in the initial TO iterations, allowing for larger input pressure loads. If successful, users are encouraged to use the COMSOL-MATLAB LiveLink.

The second approach involves assigning initial values to the design variables with an increased prevalence of $0/1$ values. The application of this approach is visualised in Figure 8.1, where Figure 8.1a displays the original initial values for the design variables used in the TO of a PA compliant gripper, and Figure 8.1b presents the alternative initial values. Although this method was tested in COMSOL, the optimiser encountered stalling issues, resulting in a diverging error. Further research on this approach is necessary to resolve these problems and investigate whether it can effectively prevent excessive deformation in the initial TO iterations.

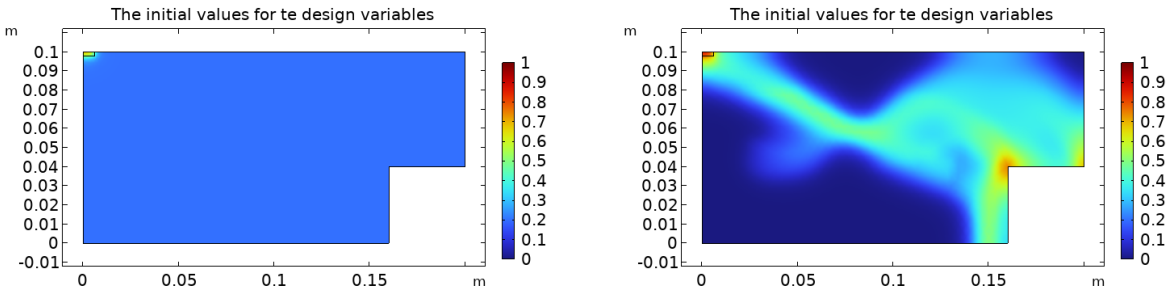

(a) The original initial values

(b) The alternative initial values

Figure 8.1: (a) the original initial values and (b) the alternative initial values for the design variables of the TO of a PA compliant gripper.

The fourth recommendation involves the exploration of alternative solid mechanics formulations in COMSOL. While the default method is the total Lagrangian formulation, the literature suggests that Eulerian and ALE formulations are more suitable when dealing with large displacements, as they exhibit better capabilities in handling mesh distortions. This can potentially lead to an increase in the maximum allowable pressure load during the TO of PACMs. Hence, it is advisable to delve into the implementation of both Eulerian and ALE formulations to assess their effectiveness and impact on the TO of PACMs.

The recommendation is to begin by investigating the Eulerian formulation, which is anticipated to be less complex than ALE formulations. This stepwise approach allows for a systematic evaluation of the benefits and complexities of each formulation, aiding in selecting the most appropriate method for addressing large deformation in the TO of PACMs.

The fifth recommendation involves considering COMSOL. It is especially recommended for readers unfamiliar with the topic due to its user-friendly interface, requiring only basic knowledge. COMSOL makes it easy to incorporate complex solid mechanics and physics, allowing for the straightforward implementation of geometric nonlinearities and a Neo-Hookean material model in all cases. Despite the potential limitation of a low maximum applied pressure load in certain scenarios, readers can still easily gain an intuition about the obtained designs.

An alternative program is suggested for more advanced readers familiar with the topic, given that COMSOL has limitations not present in programs like MATLAB. However, the drawback of using programs like MATLAB is their reliance on the skills and knowledge of the user.

Lastly, the sixth recommendation involves validating and extending this research. The results obtained in this thesis are numerically generated with computational models; therefore, it is essential to validate these results experimentally. By comparing the numerical experiments with experimental data, we can assess their accuracy. Furthermore, the models in this thesis are expected to be easily extended to three dimensions, opening opportunities for broader applications and insights.

In conclusion, this thesis successfully achieved the goals of incorporating geometric nonlinearities and a Neo-Hookean material model in the solid mechanics of the TO process for the design of PACMS. This was done in conjunction with the Darcy method for both single- and multi-material problems, paving the way for the future research discussed in this section.

References

Andreassen, E., A. Clausen, M. Schevenels, B.S. Lazarov, and O. Sigmund (2011). Efficient topology optimization in MATLAB using 88 lines of code. *Structural and Multidisciplinary Optimization* 43, 1–16.

Belytschko, T., W.K. Liu, B. Moran, and K.I. Elkhodary (2014). *Nonlinear finite elements for continua and structures*. 2nd ed. John Wiley & Sons.

Bendøe, M.P. and O. Sigmund (2003). *Topology optimization: Theory, Methods and Applications*. Springer Science & Business Media.

Bendsøe, M.P. and N. Kikuchi (1988). Generating optimal topologies in structural design using a homogenization method. *Computer Methods In Applied Mechanics And Engineering* 71(2), 197–224.

Bendsøe, M.P. and O. Sigmund (1999). Material interpolation schemes in topology optimization. *Archive of Applied Mechanics* 69, 635–654.

Bhavikatti, S. S. (2004). *Finite element analysis*. New Age International Ltd.

Bourdin, B. (2001). Filters in topology optimization. *International journal for numerical methods in engineering* 50(9), 2143–2158.

Bruns, T.E. and D.A. Tortorelli (2001). Topology optimization of non-linear elastic structures and compliant mechanisms. *Computer methods in applied mechanics and engineering* 190(26-27), 3443–3459.

Caasenbrood, B., A. Pogromsky, and H. Nijmeijer (2020). A computational design framework for pressure-driven soft robots through nonlinear topology optimization. *In 2020 3rd IEEE international conference on soft robotics (RoboSoft)*. IEEE, 633–638.

Chen, F. and M.Y. Wang (2020). Design optimization of soft robots: a review of the state of the art. *IEEE Robotics & Automation Magazine* 27(4), 27–43.

Clark, L., B. Shirinzadeh, Y. Zhong, Y. Tian, and D. Zhang (2016). Design and analysis of a compact flexure-based precision pure rotation stage without actuator redundancy. *Mechanism and Machine Theory* 105, 129–144.

COMSOL (2023). Bracket Topology Optimization. URL: `https://www.comsol.com/model/bracket-8212-topology-optimization-69891` (visited on 08/10/2023).

Conlan-Smith, C., A. Bhattacharyya, and K.A. James (2018). Optimal design of compliant mechanisms using functionally graded materials. *Structural and Multidisciplinary Optimization* 57, 197–212.

Cook, R.D., D.S. Malkus, M.E. Plesha, and R.J. Witt (2002). *Concepts and applications of finite element analysis*. 4th ed. John Wiley & Sons.

Dalklint, A., M. Wallin, and D.A. Tortorelli (2021). Structural stability and artificial buckling modes in topology optimization. *Structural and Multidisciplinary Optimization* 64(4), 1751–1763.

Dou, W., G. Zhong, J. Yang, and J. Shen (2023). Design and Modeling of a Hybrid Soft Robotic Manipulator With Compliant Mechanism. *IEEE Robotics and Automation Letters* 8(4), 2301–2308.

Frecker, M.I., G.K. Ananthasuresh, S. Nishiwaki, N. Kikuchi, and S. Kota (1997). Topological synthesis of compliant mechanisms using multi-criteria optimization. *Journal of Mechanical Design* 119(2), 238–245.

Gould, P.L. (2013). *Introduction to linear elasticity*. 3rd ed. Saint Louis, Missouri: Springer.

Guest, J., J. Prévost, and T. Belytschko (2004). Achieving minimum length scale in topology optimization using nodal design variables and projection functions. *International journal for numerical methods in engineering* 61(2), 238–254.

Holzapfel, G.A. (2000). *Nonlinear solid mechanics: A continuum approach for engineering*. Chichester, England: John Wiley & Sons.

Howell, L.L. (2001). *Compliant Mechanisms*. John Wiley & Sons.

Kim, N. (2015). *Introduction to Nonlinear Finite Element Analysis*. Springer.

Klarbring, A. and N. Strömberg (2013). Topology optimization of hyperelastic bodies including non-zero prescribed displacements. *Structural and Multidisciplinary Optimization* 47(1), 37–48.

Kumar, P. (2023). Towards topology optimization of pressure-driven soft robots. *Conference on Microactuators and Micromechanisms, Springer*, 19–30.

Kumar, P., J.S. Frouws, and M. Langelaar (2020). Topology optimization of fluidic pressure-loaded structures and compliant mechanisms using the Darcy method. *Structural and Multidisciplinary Optimization* 61(4), 1637–1655.

Kumar, P. and M. Langelaar (2021). On topology optimization of design-dependent pressure-loaded three-dimensional structures and compliant mechanisms. *International Journal for Numerical Methods in Engineering* 122(9), 123–456.

– (2022). Topological syntehsis of fluidic pressure-actuated robust compliant mechanisms. *Mechanism and Machine Theory* 174.

Lazarov, B.S. and O. Sigmund (2010). Filters in topology optimization based on Helmholtz-type differential equations. *International journal for numerical methods in engineering* 86, 765–781.

Liu, Z., F. Wang, S. Liu, Y. Tian, and D. Zhang (2020). Modeling and Analysis of Soft Pneumatic Network Bending Actuators. *IEEE/ASME Transactions on Mechatronics* 26(4), 2195–2203.

Nocedal, J. and S. J. Wright (1999). *Numerical optimization*. Springer.

Pinskier, J. and D. Howard (2022). From Bioinspiration to Computer Generation: Developments in Autonomous Soft Robot Design. *Advanced Intelligent Systems* 4(1), 2100086.

Pinskier, J., P. Kumar, D. Howard, and M. Langelaar (2023). Automated design of pneumatic soft grippers through design-dependent multi-material topology optimization. *2023 IEEE International Conference on Soft Robotics (RoboSoft)*. IEEE, 1–7.

Shintake, J., V. Cacucciolo, D. Floreano, and H. Shea (2018). Soft Robotic Grippers. *Advanced materials* 30(29), 1707035.

Sigmund, O. (2007). Morphology-based black and white filters for topology optimization. *Structural and Multidisciplinary Optimization* 33, 401–424.

Sigmund, O. and P.M. Clausen (2007). Topology optimization using mixed formulation: An alternative way to solve pressure load problems. *Computer Method in Applied Mechanics and Engineering* 196(13 - 16), 1874–1889.

Sigmund, O. and K. Maute (2013). Topology optimization approaches: A comparative review. *Structural and Multidisciplinary Optimization* 48(6), 1031–1055.

Sigmund, O. and S. Torquato (1997). Design of materials with extreme thermal expansion using a three-phase topology optimization method. *Journal of the Mechanics and Physics of Solids* 45(6), 1037–1067.

Stoker, C. (1999). Developments of the Arbitrary Lagrangian-Eulerian method in non-linear solid mechanics. *HC Stoker Enschedel, the Netherlands* 7.

Svanberg, K. (1987). The method of moving asymptotes - a new method for structural optimization. *International journal for numerical methods in engineering* 24(2), 359–373.

Trease, B.P., Y.M. Moon, and S. Kota (2004). Design of Large-Displacement Compliant Joints. *Journal of Mechanical Design* 127(4), 788–798.

Wang, F., B.S. Lazarov, and O. Sigmund (2011). On projection methods, convergence and robust formulations in topology optimization. *Structural and Multidisciplinary Optimization* 43(6), 767–784.

Wang, F., B.S. Lazarov, O. Sigmund, and J.S. Jensen (2014). Interpolation scheme for fictitious domain techniques and topology optimization of finite strain elastic problems. *Computer Methods in Applied Mechanics and Engineering* 276(6), 453–472.

Wang, M. Y. and S. Chen (2009). Compliant Mechanism Optimization: Analysis and Design with Intrinsic Characteristic Stiffness. *Mechanics Based Design of Structures and Machines* 37(2), 183–200.

Xu, Q. (2014). Design and Development of a Compact Flexure-Based XY Precision Positioning System With Centimeter Range. *IEEE Transactions on Industrial Electronics* 61(2), 893–903.

Yin, L. and G.K. Ananthasuresh (2003). Design of distributed compliant mechanisms. *Mechanics based design of structures and machines* 31(2), 151–179.

Yoon, G.H. and Y.Y. Kim (2005). Element connectivity parameterization for topology optimization of geometrically nonlinear structures. *International Journal of Solids and Structures* 42(7), 1983–2009.

Zillober, C. (1993). A globally convergent version of the method of moving asymptotes. *Structural Optimization* 6, 166–174.

A

Topology optimisation process

The TO of mechanisms occurs in predefined steps. These process steps are shown in Figure A.1. First, the design problem is determined using the FEM, which includes creating the mesh, defining material properties, and specifying boundary conditions, all under the assumption of homogeneous material distribution. Then, the iterative part of the process begins with the design parameterisation, where the design variables are chosen and specified. Then, the Finite Element Analysis (FEA) is conducted, which computes the resulting displacements, strains, and other parameters. After the FEA, the sensitivity analysis is performed. Finally, the objective function and constraints are calculated. If the difference is marginal compared to the last iteration, the mechanism is considered converged, and the iteration stops, and the TO process is completed (Bendøe et al. 2003). The specific steps of the TO process are explained in detail in Appendix A.

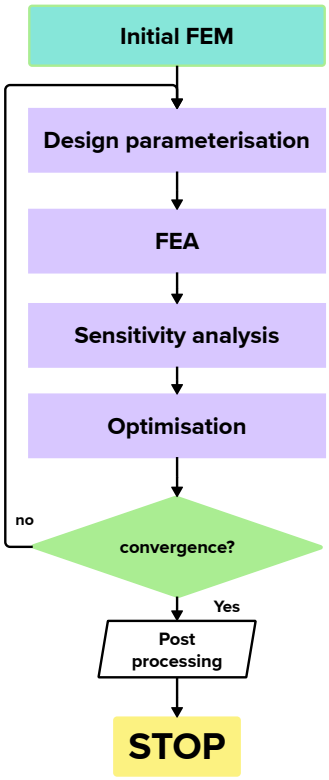

Figure A.1: The topology optimisation process

These steps are explained in detail in this appendix. The design parameterisation is discussed in Section A.1. Section A.2 presents the FEA, while Section A.3 explains the sensitivity analysis. Finally, the optimisation is detailed in Section A.4.

A.1. Design parameterisation

The initial step of the iterative part of the TO process, known as design parameterisation, involves selecting and representing design variables that control the material distribution within the domain. Techniques such as filtering and projection are employed to enhance the TO process. Details on filtering and its advantages are explained in subsection A.1.1, while subsection A.1.2 discusses the projection method and its benefits.

A.1.1. Filtering

As described in section A.2, TO involves discretising the domain into smaller finite elements. Each element is assigned a design variable, ranging from 0 (void) to 1 (solid). However, optimising without filtering can lead to checkerboard patterns in the final design, as illustrated in Figure A.2a (Bourdin 2001).

Filtering is an important step in the TO process to address the checkerboard patterns. Filtering methods aim to smooth and regularise the material distribution within the mesh, as shown in Figure A.2b (Bourdin 2001). Various filters exist; however, this subsection focuses on the density and Helmholtz density filters.

(a) TO of a cantilever beam without filtering.

(b) TO of a cantilever beam with (density) filtering.

Figure A.2: Comparison of the designs obtained from the TO of a cantilever beam without (a) and with (b) filtering. These figures were generated using the 88-line code provided in the paper by Andreassen et al. (2011).

Density filtering

Bourdin (2001) proved the existence of solutions for the density filter method for TO, introduced by Bruns et al. (2001). This approach creates a smooth transition between different material densities to avoid sudden changes in material properties. The filter helps to stabilise the optimisation process and ensures meaningful solutions for the topology design problem can be found. A convolution of the design densities and a filter function are used to filter, which can be expressed as Equation A.1 (Bourdin 2001).

$$\tilde{\rho}(\mathbf{x}) = (F * \rho)(\mathbf{x}) = \int_{\mathbb{B}_R} F(\mathbf{x} - \mathbf{y})\rho(\mathbf{y})d\mathbf{y} \tag{A.1}$$

$\tilde{\rho}$ is the filtered density variable, which is the weighted average of the density of each point in the neighbourhood, where the influence of each point is defined by the filter function F. F determines how much influence each point in the neighbourhood has on $\tilde{\rho}$ at a given position. The convolution $*$ is used to update the densities of each element based on the influence of neighbouring elements (Bourdin 2001). $\mathbb{B}_R$ is a 2D circle or a 3D sphere around $\mathbf{x}$. It is a requirement that Equation A.2 holds, which ensures that the filter function does not introduce or remove material during the convolution process (Lazarov et al. 2010).

$$\int_{\mathbb{B}_R} F dx = 1 \tag{A.2}$$

Equation A.1 can be discretised for the FEA into Equation A.3.

$$\tilde{\rho}_j = \frac{\sum_{i \in \mathbb{N}_{e,j}} w(\mathbf{x}_i) v_i \rho_i}{\sum_{i \in \mathbb{N}_{e,j}} w(\mathbf{x}_i) v_i} \tag{A.3}$$

This method enforces a high-density value at the edge of the domain, which is desired (Bourdin 2001). An example of $w(\mathbf{x}_i)$ is shown in Equation A.4. Here, (x, y) represents the coordinates of the fixed element, while (x_i, y_i) denotes the coordinates of neighbouring elements. The fixed filter radius is denoted as 'r' (Bruns et al. 2001).

$$w(\mathbf{x}_i) = max(1 - \frac{(x_i - x)^2 + (y_i - y)^2}{r}, 0) \tag{A.4}$$

Helmholtz density filtering
The filter expressed in Equation A.1 can be reformulated as a Helmholtz PDE, as demonstrated by Equation A.5. The associated homogeneous Neumann boundary condition is presented in Equation A.6. This boundary condition is equivalent to Equation A.2 and ensures that the filter function does not introduce or remove material during the filtering process (Lazarov et al. 2010).

$$-r^2\nabla^2\tilde{\rho} + \tilde{\rho} = \rho \tag{A.5}$$

$$\frac{\partial\tilde{\rho}}{\partial\mathbf{n}} = 0 \tag{A.6}$$

When the length scale is poorly defined, especially in complex structures, traditional discretisation filtering methods can encounter challenges, such as mesh-dependent results. The Helmholtz PDE can be applied as a density filter, which can handle problems without a precise length scale (Lazarov et al. 2010). It is worth noting that Equation A.1 can be written into Equation A.5, where the density function is Green's function. Furthermore, COMSOL uses the Helmholtz filter by default.

A.1.2. Non-linear Projection techniques

A drawback of the filtering approach is the fading effect at the boundaries of the models. This effect causes a gradual transition from solid to void, resulting in unwanted intermediate values that can lead to instabilities (Guest et al. 2004). Furthermore, the filtered solutions may be meaningless, especially for complex objective functions such as CMs. Non-linear projection methods are introduced to transform the filtered design variables into distinct void/solid regions (Wang, Lazarov, and Sigmund 2011).

The threshold projection, given by Equation A.7, is a combination of the projection methods introduced by Guest et al. (2004) and Sigmund (2007). In this equation, η represents the threshold determining the location of the transition between density values, and β determines the steepness of the transition between solid and void. Furthermore, a η value close to 0.5 shows smooth convergence (Wang, Lazarov, and Sigmund 2011). It should be noted that $\bar{\rho}_i \approx 0$, when $\tilde{\rho}$ is smaller than η and β is large enough and $\bar{\rho}_i \approx 1$, when $\tilde{\rho}$ is larger than η and β is large enough.

$$\bar{\rho}_i = \frac{tanh(\beta\eta) + tanh(\beta(\tilde{\rho} - \eta))}{tanh(\beta\eta) + tanh(\beta(1 - \eta))} \tag{A.7}$$

A.2. Finite element analysis

Finding the analytical solution of a model can be extremely challenging when the model becomes very complex. Model complexity often arises when it includes complex geometries, nonlinear behaviour, or highly coupled equations. The FEM is a numerical technique used to approximate field variables in partial differential equations (PDEs) and integrals in a wide range of engineering applications. An example of a field variable is the displacement field in solid mechanics. In the FEM, the fundamental concept entails subdividing the model into discrete finite elements characterised by simple geometries, as shown in Figure A.3. It is important to note that these elements are non-overlapping and connected by nodes, represented as yellow dots in Figure A.3. In FEM, the field variables of the elements can be calculated using the nodal field variables, which are the DOFs of the element. The overall solution for the field variables of the model can be calculated by interpolating the nodal field variable of each element. The arrangement of all the elements in the body is called the mesh (Cook et al. 2002).

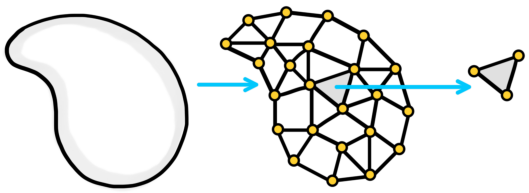

Figure A.3: The main concept of FEM

The FEA consists of several steps, partly visualised in Figure A.6.

1. **Step 1: Discretising the model**

   The first step is to discretise the model, subdividing it into elements, as shown in Figure A.3 and Figure A.6a.

2. **Step 2: Selecting the shape functions**

   The second step involves the selection of an appropriate shape function, denoted as **N**, which determines the field variable within the element as a function of the field variables at each node within that element. **N** maps the deformation of the real domain (x, y) into a standard element (ξ, η), as visualised in Figure A.4. The matrix representation of the mapping is provided in Equation A.8, where $\mathbf{x}_n^e$ are the nodal coordinates of the physical elements, and $\mathbf{x}^e$ is the coordinates of the standard element. Note that $-1 \leq \xi \leq 1$ and $-1 \leq \eta \leq 1$.

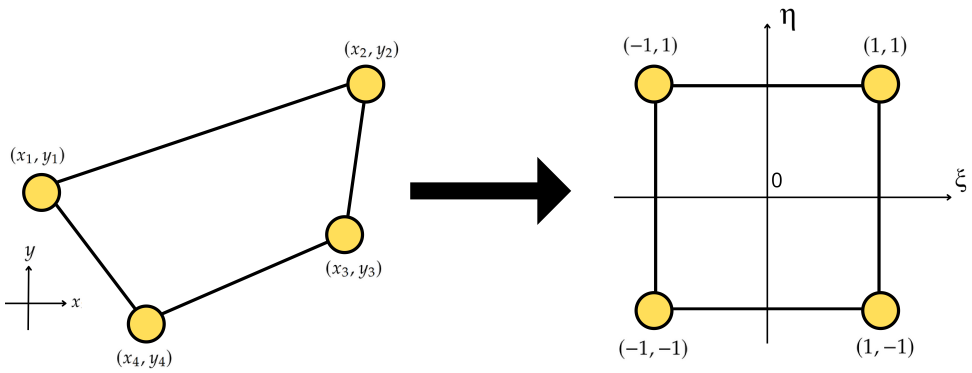

Figure A.4: The mapping from the physical domain (x,y) into the standard element (ξ, η)

$$\mathbf{N}(\xi,\eta)\mathbf{x}_n^e(x,y) = \begin{bmatrix} N1 & 0 & N2 & 0 & N3 & 0 & N4 & 0 \\ 0 & N1 & 0 & N2 & 0 & N3 & 0 & N4 \end{bmatrix} \begin{bmatrix} x_1 \\ y_1 \\ x_2 \\ y_2 \\ x_3 \\ y_3 \\ x_4 \\ y_4 \end{bmatrix} \rightarrow \mathbf{x}^e(\xi,\eta) \tag{A.8}$$

3. **Step 3: Defining the element properties**

   The third step is to find the element properties. For the typical element shown in Figure A.5, the displacements u and v at any point in the element can be calculated using Equation A.9 and Equation A.10, respectively. Other element properties can be determined similarly.

$$u = \Sigma N_i u_i = N_1 u_1 + N_2 u_2 + N_3 u_3 + N_4 u_4 \tag{A.9}$$

$$v = \Sigma N_i v_i = N_1 v_1 + N_2 v_2 + N_3 v_3 + N_4 v_4 \tag{A.10}$$

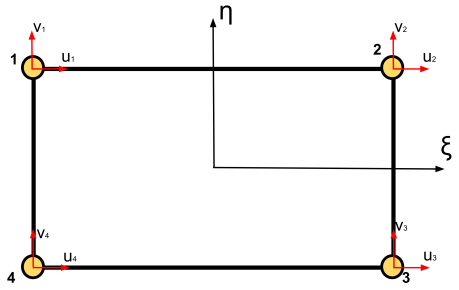

Figure A.5: a typical element

4. **Step 4: Assembly**

   In the fourth step, element properties are assembled to determine the global properties of the model, as depicted in Figure A.6b.

5. **Step 5: Solving the system of equations**

   The fifth step includes applying boundary conditions and solving the system of equations within the model, as shown in Figure A.6c (Bhavikatti 2004). For details on deriving the interpolation function and a better understanding of FEA, refer to Cook et al. (2002) and Bhavikatti (2004).

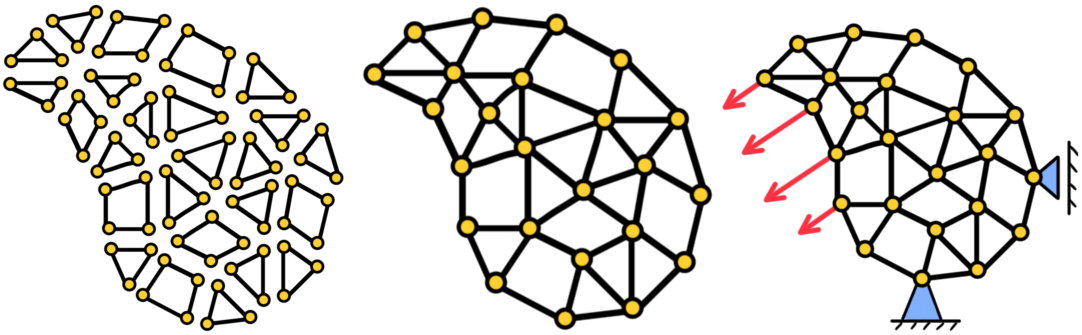

(a) Discretise the model **(b)** Assembly of the elements **(c)** Solving the system of equation

Figure A.6: Part of the FEM process is presented: (a) discretisation of the model, (b) Assembly of the elements after calculating the field variables of each element, (c) Boundary conditions are applied, and the system of equation is solved.

A.3. Sensitivity analysis

It is essential for the Moving Methods of Asymptotes (discussed in section A.4) to determine the gradients of the objective function and the constraint with respect to the design variables, also called sensitivities, (Svanberg 1987).

The adjoint method is the most common and efficient technique for calculating the sensitivities in the context of TO. An augmented function, structured like the Lagrangian $\mathcal{L}$, must be determined to compute sensitivities. This augmented function depends on the objective function and the constraints.

Calculating the sensitivities for compliance optimisation problem is demonstrated in subsection A.3.1. Additionally, sensitivity analyses for a CM is presented in subsection A.3.2.

A.3.1. Sensitivity analysis of structures

It demonstrates how the sensitivities are calculated using an example. In Equation A.11 presents a general formulation for a compliance problem. The meaning, notation and the units for the parameter used in Equation A.11 are presented in Table A.1. The augmented function ($\mathcal{L}$) is presented in Equation A.12, where λ_1^T is the Lagrange multiplier. Subsequently, the sensitivities can be obtained by taking the derivative of $\mathcal{L}$ with respect to ρ, as shown in Equation A.13. The choice of λ_1^T is made to ensure that the 'MultiplierTerm' vanishes. When 'MultiplierTerm' equals zero, it results in the vanishing of $\frac{\partial u}{\partial \rho}$ as well.

Parameter	Notation	unit
The objective function	f_0	-
Design variables vector	$\boldsymbol{\rho}$	-
Load vector	$\mathbf{f}$	N
Material volume	V	m^3
Maximum material volume	$V*$	m^3

Table A.1: The meaning, notation and the units for the parameters used in Equation A.11.

The calculation of $\frac{\partial u}{\partial \rho}$ is performed through a back substitution process, presented as $\mathbf{Ku} = \mathbf{f}$, and this calculation needs to be carried out for each design variable. The advantage of the adjoint method is that the back substitutions used in the obtained sensitivities are not dependent on the design variables, simplifying the sensitivity analysis. The equation for λ_1^T is obtained in Equation A.14, and as a consequence, the sensitivity is obtained in Equation A.15.

$$\left.\begin{aligned} \min_{\rho} \quad & f_0(\mathbf{u},\boldsymbol{\rho}) = u(\boldsymbol{\rho})^T K(\boldsymbol{\rho}) u(\boldsymbol{\rho}) \\ \text{such that} \quad & \mathbf{K}(\boldsymbol{\rho})\mathbf{u}(\boldsymbol{\rho}) = \mathbf{F} \\ & \frac{V(\boldsymbol{\rho})}{V^*} - 1 \leq 0 \\ & \mathbf{0} \leq \boldsymbol{\rho} \leq \mathbf{1} \end{aligned}\right\} \tag{A.11}$$

$$\mathcal{L} = f_0(\boldsymbol{\rho}) + \lambda_1^T(\mathbf{Ku} - \mathbf{F}) \tag{A.12}$$

$$\frac{d\mathcal{L}}{d\boldsymbol{\rho}} = \frac{\partial f_0}{\partial \boldsymbol{\rho}} + \underbrace{(\frac{\partial f_0}{\partial \mathbf{u}} + \lambda_1^T K)}_{\text{MultiplierTerm}} \frac{\partial \mathbf{u}}{\partial \boldsymbol{\rho}} + \lambda_1^T \frac{\partial \mathbf{K}}{\partial \boldsymbol{\rho}}\mathbf{u} \tag{A.13}$$

$$\lambda_1^T = -\frac{\partial f_0}{\partial u} K^{-1} \tag{A.14}$$

$$\frac{d\mathcal{L}}{d\boldsymbol{\rho}} = \frac{df_0}{d\boldsymbol{\rho}} = \frac{\partial f_0}{\partial \boldsymbol{\rho}} + \lambda_1^T \frac{\partial \mathbf{K}}{\partial \boldsymbol{\rho}}\mathbf{u} \tag{A.15}$$

A.3.2. Sensitivity analysis of compliant mechanism

The multi-criteria formulation for a CM is provided in Equation A.16, while the corresponding sensitivity analysis is detailed from Equation A.17 to Equation A.21. The augmented function ($\mathcal{L}$) and the derivative with respect to $\boldsymbol{\rho}$ are given in Equation A.17 and Equation A.18. Where λ_1^T and λ_2^T are the Lagrange multipliers, which are chosen such that the terms $\frac{\partial \mathbf{u}}{\partial \boldsymbol{\rho}}$ and $\frac{\partial \mathbf{v}}{\partial \boldsymbol{\rho}}$ vanishes. They can be expressed as Equation A.19 and Equation A.20.

$$\left.\begin{aligned} \min_{\rho} \quad & f_0(\mathbf{u},\boldsymbol{\rho}) = -\frac{MSE(\mathbf{u},\mathbf{v},\boldsymbol{\rho})}{2SE(\mathbf{u},\boldsymbol{\rho})} = -\frac{\mathbf{v}^T\mathbf{Ku}}{\mathbf{u}^T\mathbf{Ku}} \\ \text{such that} \quad & \mathbf{K}(\boldsymbol{\rho})\mathbf{u}(\boldsymbol{\rho}) = \mathbf{F} \\ & \mathbf{K}(\boldsymbol{\rho})\mathbf{v}(\boldsymbol{\rho}) = \mathbf{F}_d \\ & \frac{V(\boldsymbol{\rho})}{V^*} - 1 \leq 0 \\ & \mathbf{0} \leq \boldsymbol{\rho} \leq \mathbf{1} \end{aligned}\right\} \tag{A.16}$$

$$\mathcal{L} = f_0(\boldsymbol{\rho}) + \lambda_1^T(\mathbf{Ku} - \mathbf{F}) + \lambda_2^T(\mathbf{Kv} - \mathbf{F}_d) \tag{A.17}$$

$$\frac{d\mathcal{L}}{d\boldsymbol{\rho}} = \frac{\partial f_0}{\partial \boldsymbol{\rho}} + (\frac{\partial f_0}{\partial u} + \lambda_1^T \mathbf{K})\frac{\partial u}{\partial \boldsymbol{\rho}} + (\frac{\partial f_0}{\partial v} + \lambda_2^T \mathbf{K})\frac{\partial v}{\partial \boldsymbol{\rho}} + \lambda_1^T \frac{\partial \mathbf{K}}{\partial \boldsymbol{\rho}}\mathbf{u} + \lambda_2^T \frac{\partial \mathbf{K}}{\partial \boldsymbol{\rho}}\mathbf{v} \tag{A.18}$$

$$\lambda_1^T = -\frac{\partial f_0}{\partial u}\mathbf{K}^{-1} \tag{A.19}$$

$$\lambda_2^T = -\frac{\partial f_0}{\partial v}\mathbf{K}^{-1} \tag{A.20}$$

Equation A.19 and Equation A.20 can be used to determine the sensitivities as expressed in Equation A.21.

$$\frac{d\mathcal{L}}{d\boldsymbol{\rho}} = \frac{\partial f_0}{\partial \boldsymbol{\rho}} + \lambda_1^T \frac{\partial \mathbf{K}}{\partial \boldsymbol{\rho}}\mathbf{u} + \lambda_2^T \frac{\partial \mathbf{K}}{\partial \boldsymbol{\rho}}\mathbf{v} \tag{A.21}$$

A.4. Optimisation

In the TO, the SIMP and the level set-based methods are the most common approaches to optimise the material distribution within a design domain to achieve specific performance objectives while simultaneously considering constraints. This thesis considers the SIMP approach, which initially seems counterintuitive compared to the level-set method, where boundaries are explicitly defined. Explicit boundaries can be an advantage, especially in scenarios involving pressure loads. However, the decision to consider SIMP over the level-set method, even though the latter may seem the more obvious choice, is based on the practicality of SIMP. SIMP is widely implemented in commercial software such as COMSOL, whereas the level-set method is not.

In the SIMP method, each element is assigned a specific density ρ_e, satisfying the condition $0 \leq \rho_e \leq 1$. Subsequently, the Young's modulus for individual element e can be computed. Two variants of the SIMP approach exist: the original SIMP and the modified SIMP. The original SIMP method was initially introduced by Bendsøe and Sigmund (1999), as demonstrated in Equation A.22. p represents the penalisation parameter, and E_0 represents the Young's modulus of the solid material. However, this approach can lead to a singular stiffness matrix (Sigmund and Clausen 2007). Consequently, Sigmund and Clausen (2007) developed the modified SIMP, as shown in Equation A.23. Here, E_{void} represents the Young's modulus of the void and serves as the lower bound for the Young's modulus ($0 < E_{void} << E_0$).

$$E(\rho_e) = \rho_e^p E_0 \tag{A.22}$$

$$E(\rho_e) = E_{void} + \rho_e^p (E_0 - E_{void}) \tag{A.23}$$

Effective convergence is achieved by setting the penalisation parameter p to 3. When p is too small, it generates a large grey scale. Conversely, when p is set to a high value, it results in fast convergence to a potential local minimum, as discussed in more detail by Sigmund and Maute (2013).

As mentioned earlier, the SIMP approach involves assigning specific densities to each element within the design domain, and these densities are iterative optimised to achieve the optimal material distribution. Several TO algorithms exist to solve the optimising problem. The MMA is the most common algorithm, a gradient-based optimisation technique for solving complex engineering and mathematical optimisation problems. Due to the gradient-based optimisation, it is crucial to determine the sensitivities. It was developed by Svanberg (1987) and has since gained popularity for its effectiveness. Due to the effectiveness of the MMA, it will be used in this thesis.

The disadvantage of the normal MMA is that the algorithm does not guarantee convergence, leading to unwanted results (Zillober 1993). Zillober (1993) develop the so-called global convergent MMA (GCMMA), which guarantees global convergence. Global convergence refers to the property of an algorithm to converge to the global minimum of the objective function, regardless of the initial guess or starting point. GCMMA makes use of a line search, which improves the behaviour of the optimisation. This method is used by default in COMSOL.

B

The validation of the Darcy method

A case study is conducted to validate the correct implementation of the Darcy method in COMSOL, involving the analysis of five different scenarios. In COMSOL, various options are available for modelling the Darcy method. This thesis explores two options: the heat flow module, as demonstrated in the paper by Pinskier, Kumar, et al. (2023), and a PDE. While the heat flow module is similar to the Darcy method, it uses temperature instead of pressure. Despite this difference, the underlying mathematical frameworks are equivalent. It should be noted that when referring to pressure in the context of the Heat Flow Module, it is, in fact, temperature. In contrast, the PDE straightforwardly implements the Darcy method.

The description, notation, and values for various parameters utilised in the COMSOL models in this section are listed in Table B.1. The plane strain assumption is applied, signifying that all z-components are zero. Furthermore, the model employing the Heat Flow Module is referred to as the HFM model, while the model utilising the PDE is referred to as the PDE model.

Parameter	Notation	Value
Width	W	0.2m
Height	H	0.1m
Young's modulus solid regions	E_1	$1 \times 10^6 \mathrm{N/m^2}$
Young's modulus void regions	E_0	$E_1 \times 1 \times 10^6 \mathrm{N/m^2}$
Out-of-plane thickness	t	0.002 m
$K(\rho_e)$ step location	η_k	0.3
$K(\rho_e)$ slope of the step	β_k	10
$D(\rho_e)$ step location	η_h	0.2
$D(\rho_e)$ slope of the step	β_h	10
Flow coefficient of the void element	k_v	1 $m^4/(Ns)$
Flow coefficient of the solid element	k_s	$k_v \times 10^{-7} m^4 N^{-1} s^{-1}$
Ratio input pressure to the pressure at Δs	r	0.1
The penetration depth	Δs	0.002 m

Table B.1: The description, notation, and value for various parameters used in the models in this section

B.1. Completely solid Beam

The schematic visualisation of the first scenario is presented in Figure B.1. In the HFM model, the temperature on the 'pressure' boundary is set at 293.15 K, whereas in the PDE model, a pressure load of 1×10^4 Pa is applied. The beam is completely solid, and the pressure load is applied on the right side. The remaining edges have a pressure of 0 Pa or a temperature of 0 K. It can be observed from Figure B.2a and Figure B.3a that an immediate pressure drop on the pressure boundary occurs. Figure B.12 illustrates the results of the HFM model and Figure B.13 presents the results of the PDE model. Moreover, Figure B.2b and Figure B.3b result in the body loads as expected.

However, unlike the PDE model, a notable difference arises in the HFM model, where the body loads on the bottom and upper edge are not horizontal. The sensitivity of the HFM model to sharp edges, a limitation not present in the PDE model, can explain the observed difference in body load orientations on the bottom and upper edges. Nevertheless, the obtained results in Figure B.2 and Figure B.3 validate that the Darcy method correctly functions for this specific scenario.

Additionally, an investigation is conducted to observe the impact of integrating the Neo-Hookean material model in the solid mechanics. Incorporating the Neo-Hookean material model exhibits no influence on the results. This observation aligns with the expectations, as determining the pressure field and the corresponding body loads are independent of the Neo-Hookean material model.

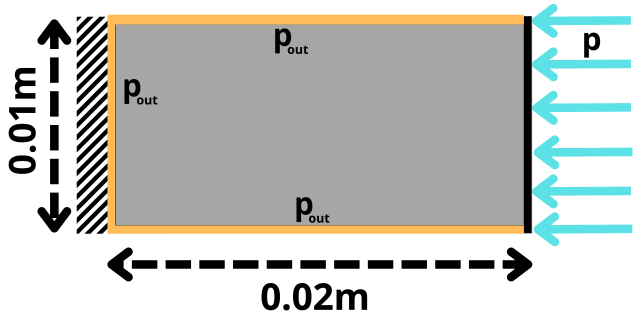

Figure B.1: The schematic visualisation of the first scenario and its boundary conditions.

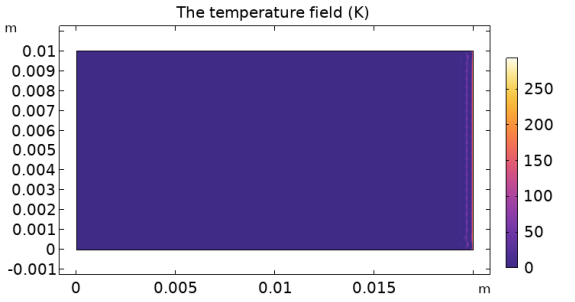

(a) The temperature field

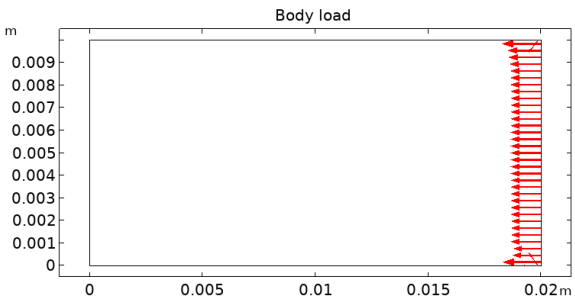

(b) The body load with a scaling factor of 2×10^{-10}

Figure B.2: The obtained temperature field (a) and body load (a) from the analysis of the first scenario of the HFM model.

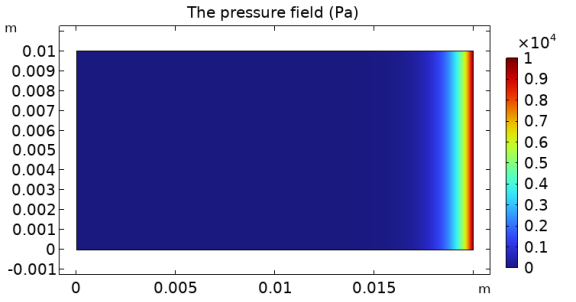

(a) The pressure field

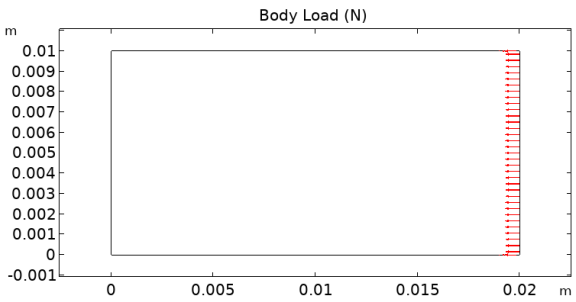

(b) The body load for $\gamma = 1.0$ with a scaling factor of 9.6×10^{-11}

Figure B.3: The obtained pressure field (a) and body load (b) from the analysis of the first scenario of the PDE model.

B.2. Beam with solid and void halves

The schematic visualisation of the second scenario is presented in Figure B.4, depicting a beam divided into solid (dark grey) and void (light grey) halves. Figure B.12 illustrates the results of the HFM model and Figure B.13 presents the results of the PDE model. The pressure or temperature drop occurs precisely at the solid-void boundary for both models, aligning with the expectations. Additionally, in this scenario, the body loads along the bottom and upper edges in the HFM model are non-horizontal, which is again a consequence of the sharp edges.

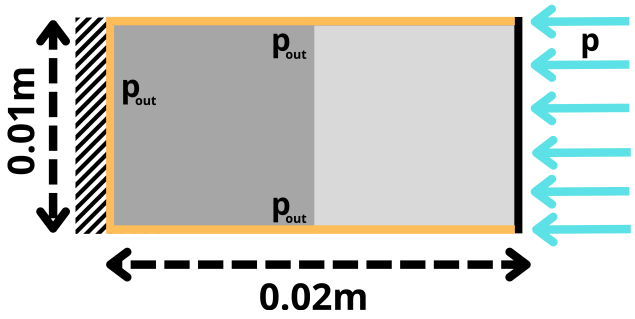

Figure B.4: The schematic visualisation of the second scenario and its boundary conditions.

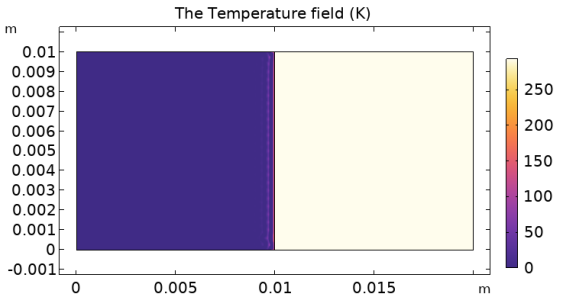

(a) The temperature field

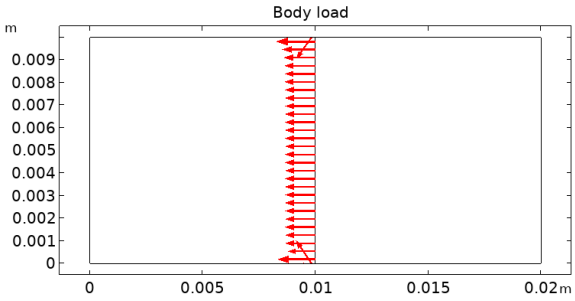

(b) The body load with a scaling factor of 8×10^{-10}

Figure B.5: The obtained temperature field (a) and body loads (b) from the analysis of the second scenario of the HFM model.

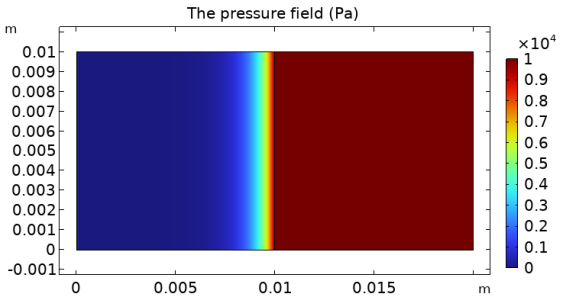

(a) The pressure field

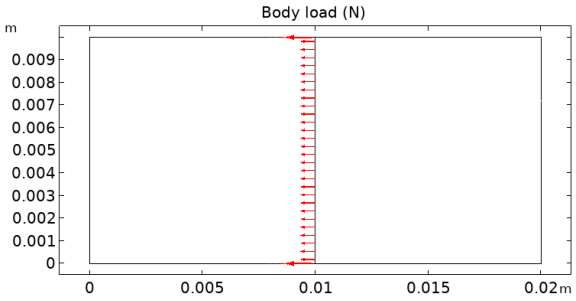

(b) The body load with a scaling factor of 1.2×10^{-10}

Figure B.6: The obtained pressure field (a) and body loads (a) from the analysis of the second scenario of the PDE model

B.3. Beam with solid semicircle

The schematic visualisation of the third scenario is presented in Figure B.4, illustrating a solid (dark grey) semicircle with the remaining part of the beam as void (light grey). The results of the analyses are depicted in Figure B.8 and Figure B.9. Once again, the pressure drop is immediate at the solid-void interfaces. However, the HFM model shows a significant increase in body load in the upper- and bottom-left corners compared to the PDE model.

This behaviour is associated with the presence of a sharp edge. The diameter of the semicircle is reduced to investigate the influence of this sharp edge on the left corners. Figure B.10 presents the resulting body load for the smaller semicircle, showing the absence of large body loads in this scenario. This observation confirms that the significant loads obtained on the left corners in Figure B.8b are attributed to the presence of sharp edges. Although the large body load is eliminated, the resulting body load distribution remains non-uniform, a consequence of the non-uniform temperature within the semicircle. This phenomenon deviates from the anticipated uniformity expected over the pressure boundary and requires further investigation to elucidate the underlying causes.

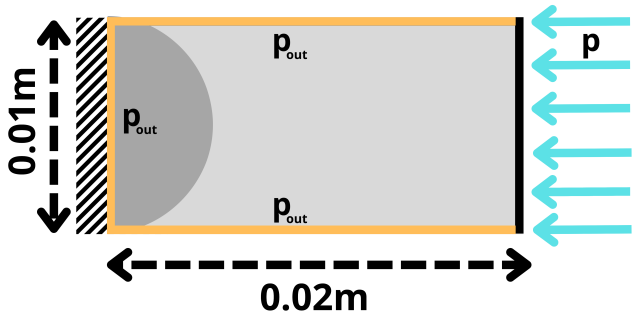

Figure B.7: The schematic visualisation of the third scenario and its boundary conditions.

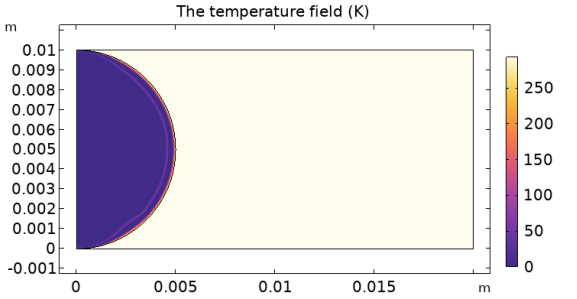

(a) The temperature field.

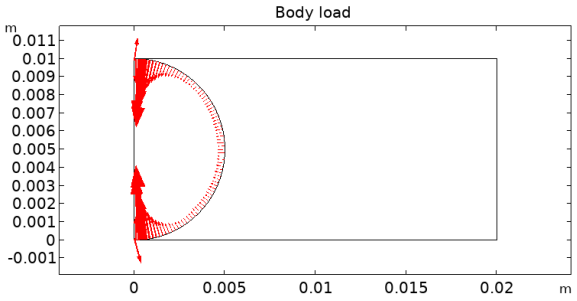

(b) The body load with a scaling factor of 3×10^{-10}

Figure B.8: The obtained temperature field (a) and body load (b) from the analysis of the third scenario of the HFM model.

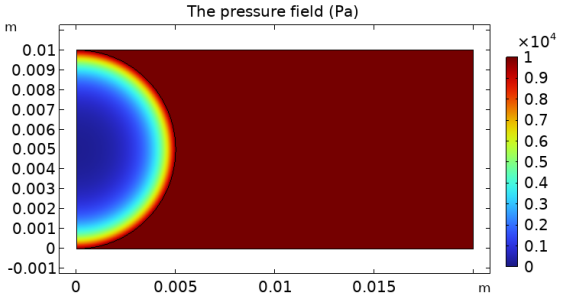

(a) The pressure field.

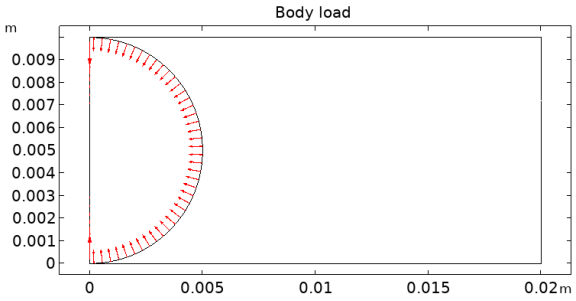

(b) The body load with a scaling factor of 1.2×10^{-10}

Figure B.9: The obtained pressure field (a) and body load (b) from the analysis of the third scenario of the PDE model

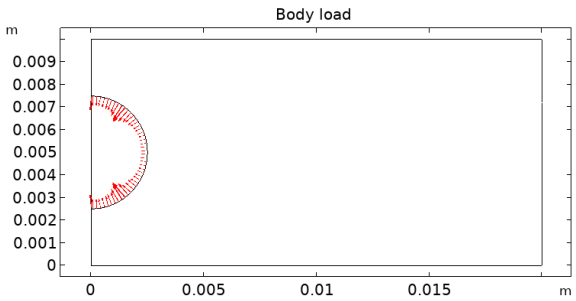

Figure B.10: The obtained body load from the analysis of the third scenario with a smaller circle of the HFM model. The scaling factor is 3×10^{-10}

B.4. Beam with gradual transition from solid to void

The schematic visualisation of the fourth scenario is presented in Figure B.11, illustrating a gradual transition from solid on the left edge to void on the right edge. Figure B.12 illustrates the results of the HFM model and Figure B.13 presents the results of the PDE model. The additional black lines in the figures serve to illustrate body loads. As depicted in Figure B.13, the pressure gradually decreases with increased solidity of the beam, consistent with the obtained body loads illustrated in Figure B.13b. The body loads are located on the right side of the beam, where the pressure is the highest, as expected.

In contrast, within the HFM model, the temperature undergoes a marginal decrease as the material becomes more solid, resulting in correspondingly insignificant body loads. These body loads are present on the left side, which is peculiar since they are expected on the right side. The observed small body loads on the left side can be attributed to their insignificance; given their small values, numerical errors may contribute to their presence on the left side.

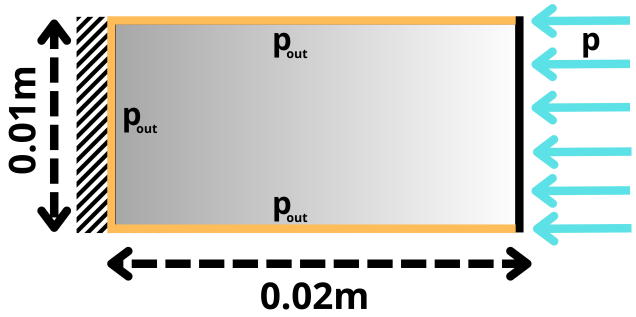

Figure B.11: The schematic visualisation of the fourth scenario and its boundary conditions.

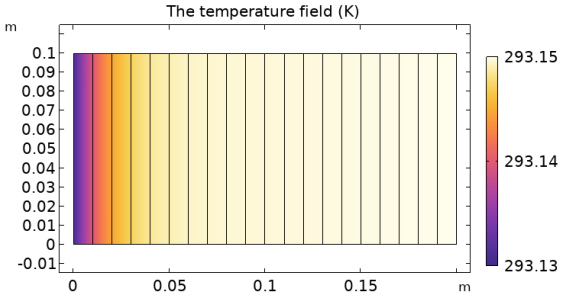

(a) The temperature field.

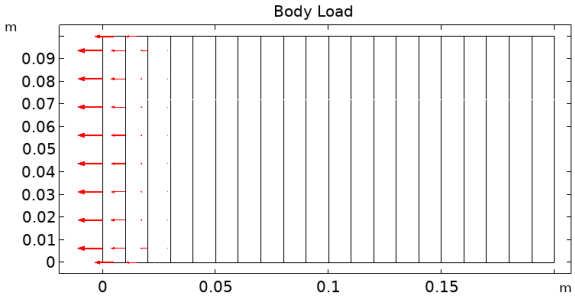

(b) The body load with a scaling factor of 0.01

Figure B.12: The obtained temperature field (a) and body load (b) from the analysis of the fourth scenario of the HFM model.

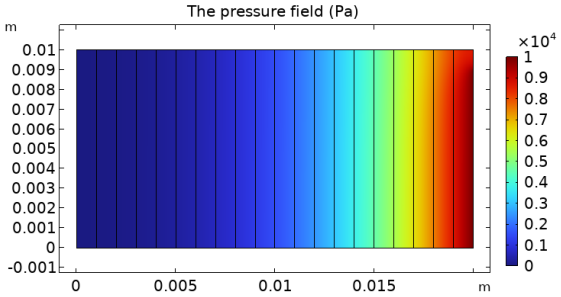

(a) The pressure field.

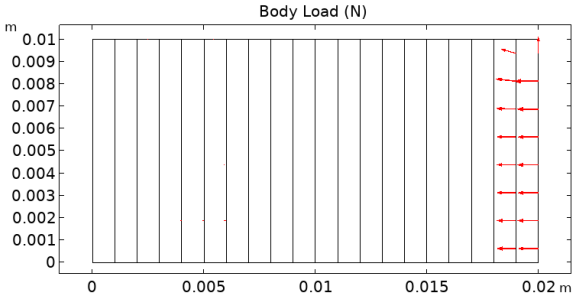

(b) The body load with a scaling factor of 7.1×10^{-10}

Figure B.13: The obtained pressure field (a) and body load (b) from the analysis of the fourth scenario of the PDE model

B.5. Solid beam with intermediate values

The schematic visualisation in the fifth scenario is identical to that of the first case, as shown in Figure B.1. However, intermediate values are explored by introducing the parameter γ. A solid region corresponds to $\gamma = 1$, while $\gamma = 0$ corresponds to a void region. The examination involves values for γ between 0 and 1.

The HFM proves to be sensitive to sharp edges, a limitation not shared by the PDE model. Moreover, the HFM model yields peculiar results, and its behaviour needs to be better understood. Consequently, this scenario will exclusively concentrate on the more reliable and robust PDE model.

From Figure B.14, it is evident that the desired results are achieved for $\gamma > 0.6$ for this problem with the specific parameters, illustrated in Figure B.14d to Figure B.14h. The pressure does not drop as required for $\gamma \leq 0.6$, leading to smaller body loads. The slow drop prevents the pressure from reaching the desired level within the specific constraints of this problem.

The obtained pressure field and body loads aim to provide insight and intuition into the behaviour of the Darcy method for various intermediate values.

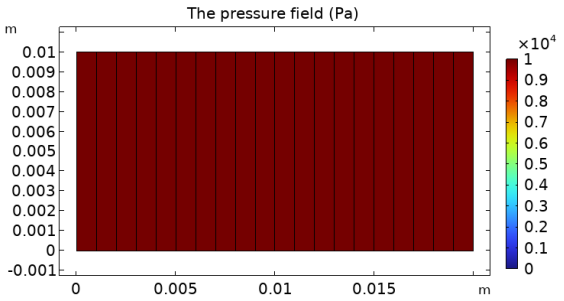

(a) The pressure field for $\gamma = 0.4$

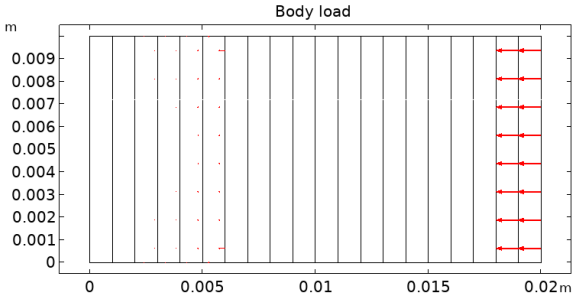

(b) The body load for $\gamma = 0.4$ with a scaling factor of 5.1×10^{-6}

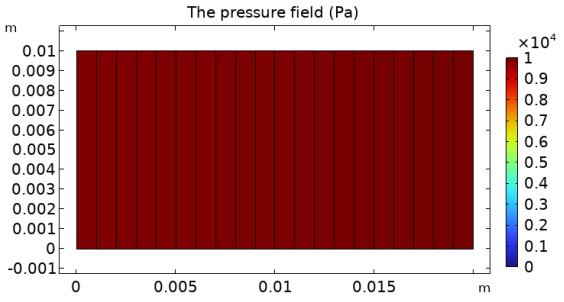

(c) The pressure field for $\gamma = 0.6$

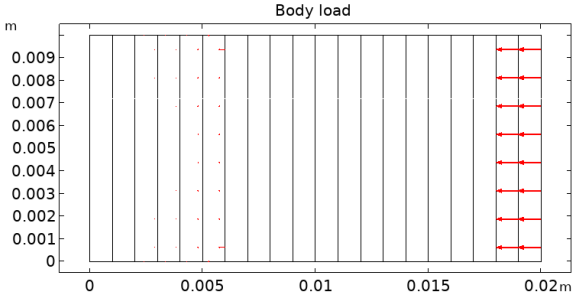

(d) The body load for $\gamma = 0.6$ with a scaling factor of 1.0×10^{-7}

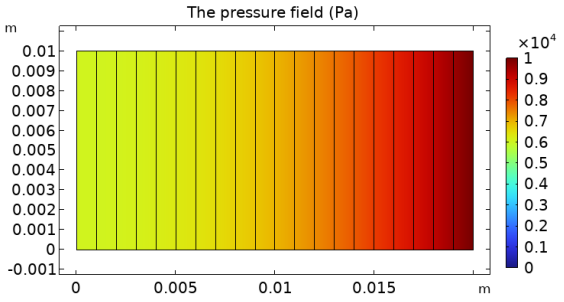

(e) The pressure field for $\gamma = 0.8$

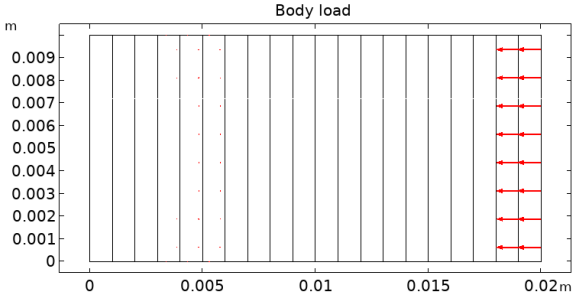

(f) The body load for $\gamma = 0.8$ with a scaling factor of 2.5×10^{-9}

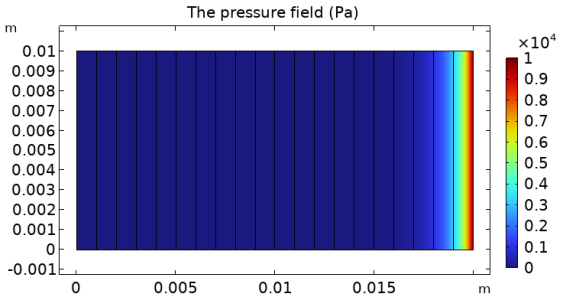

(g) The pressure field for $\gamma = 1.0$

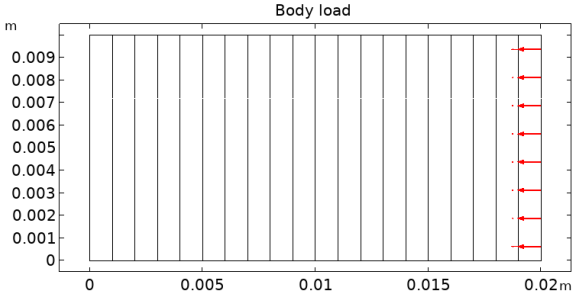

(h) The body load for $\gamma = 1.0$ with a scaling factor of 9.6×10^{-11}

Figure B.14: The pressure field (left column) and body loads (right columns) from the analysis of the fifth scenario for different values of γ of the PDE model under an applied pressure of 1×10^4 Pa

C

Intermediate values interpolation factor for C-beam with Wang method

Intermediate values for the density variables during the TO are inevitable, falling within the range of 0 to 1. Consequently, this results in intermediate values for γ_e. Therefore, examining the impact of these intermediate values on the C-beam model is crucial. This investigation aims to identify whether any intermediate value poses challenges, as such challenges could subsequently affect the TO. A parametric sweep on γ_e is conducted to observe potential numerical instabilities, where γ_e has values from 0 to 1 with increments of 0.01. In this section, the first strain method $\mathbf{E}_{W,1}$

In Figure C.1, the analysis results of the C-beam, incorporating the Wang method with varying values for γ_e in the void region, are illustrated. In this representation, the solid region maintains $\gamma_e = 1$. It is evident that when $\gamma_e = 1$ for the void region, the result is equivalent to a Neo-Hookean model.

In Table C.1, the maximum applied load for each analysis is presented for different values of γ_e. As γ_e increases from 0 to 0.6, forces f_1 and f_2 remain relatively stable. However, a noticeable shift occurs at γ_e values of 0.8 and 0.9, leading to a significant decrease in f_1 and f_2. This behaviour change can be attributed to the implementation of the Wang method, specifically designed to address numerical instabilities arising from void regions in nonlinear theory applications. As γ_e rises, the influence of the void areas becomes more pronounced, underscoring the significance of these nonlinear effects. Consequently, this amplified influence increases numerical instabilities, leading to a decrease in the values of the forces.

In conclusion, the results indicate that intermediate values do not induce numerical instabilities. Consequently, it is anticipated that the intermediate values of γ_e obtained from the design variables during the TO process will not give rise to any issues.

γ_e	f_1 (N)	f_2 (N)
0	0.0055	0.0145
0.1	0.0054	0.0144
0.2	0.0055	0.0145
0.4	0.0056	0.0146
0.6	0.0056	0.0146
0.8	0.0024	0.0114
1.0	0.0009	0.0099

Table C.1: The maximum applied load subjected to the C-beam incorporating the Wang method for various values of γ_e

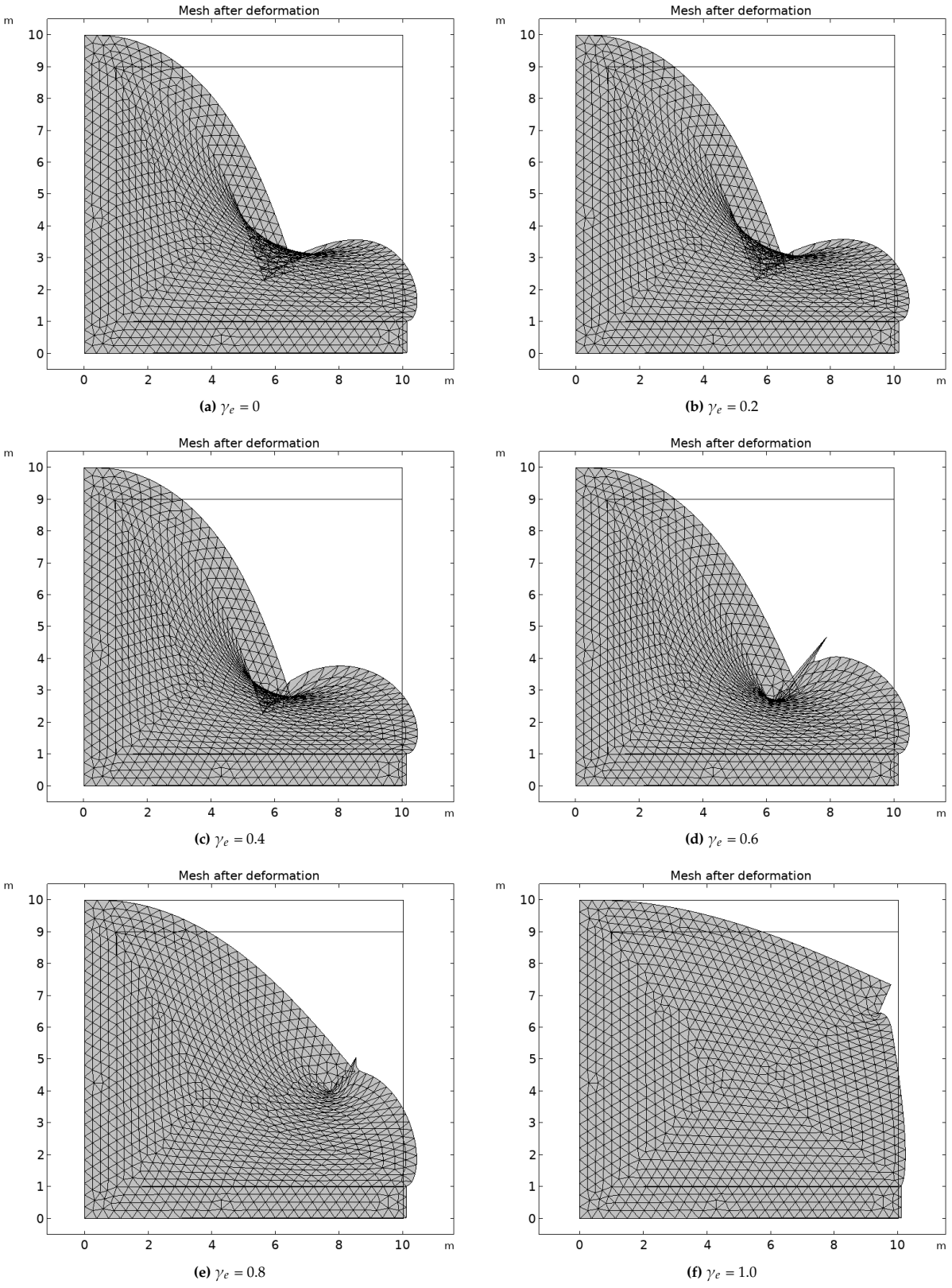

(a) $\gamma_e = 0$ **(b)** $\gamma_e = 0.2$

(c) $\gamma_e = 0.4$ **(d)** $\gamma_e = 0.6$

(e) $\gamma_e = 0.8$ **(f)** $\gamma_e = 1.0$

Figure C.1: The analysis results of a C-beam, incorporating the Wang method with varying values of γ_e for the void region within the C-beam.

D

Parameter study of the Wang method

A parameter study has been conducted to examine the influence of the parameters of γ_e on the TO results. The formula for the interpolation factor γ_e involves three parameters: β_1, η_1, and p. For clarity, the formula for γ_e is restated in Equation D.1.

$$\gamma_e = \frac{tanh(\beta_1\eta_1) + tanh(\beta_1(\tilde{\rho}_e^p - \eta_1))}{tanh(\beta_1\eta_1) + tanh(\beta_1(1-\eta_1))} \tag{D.1}$$

In this section, the TO problem consistently incorporates the Wang method. The schematic visualisation of the TO problem is represented in Figure D.1, illustrating the cantilever beam design and its associated boundary conditions. The Young's modulus of a solid element is $E_1 = 3 \times 10^9$ N/m^2, while the Young's modulus of a void element is $E_0 = E_1 \times 10^{-6}$ N/m^2. The out-of-plane thickness is 0.1m, and the poison ratio ν is set to 0.4. In the COMSOL models, the plane strain assumption is used, meaning all the z-components are zero. The applied force is equal to 150 kN unless stated otherwise. In addition, fifty iterations have been performed for each result using the GCMMA, as convergence has been reached after fifty iterations. The objective function is focused on minimising the total elastic strain energy.

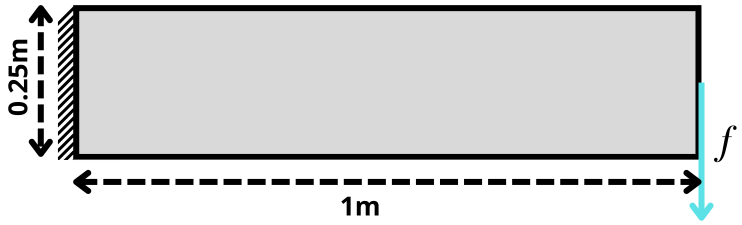

Figure D.1: The schematic visualisation of the cantilever beam and the associated boundary conditions

As part of the parameter study, the first investigation involves analysing the impact of altering β_1 in section D.2. The influence of changing η_1 on the results is explored in section D.3. Subsequently, the effect of varying parameter p is studied in section D.4. Finally, the consequences of adding projection are demonstrated in section D.5. It is important to note that the results in this section are obtained without using a filter or a projection.

Additionally, the simulations were conducted on an HP ZBook equipped with an Intel Core i7 processor (7th generation).

D.1. Implementation of a Helmholtz filter

Integrating a Helmholtz filter with the Wang method introduces challenges, resulting in unsolvable problems. While functional for small applied forces (around 1 N), the method encounters difficulties for higher applied forces. Specifically, a warning, "Forward solution failed, requesting reduced step", arises, leading to a stalled optimiser. Notably, for forces of the order of 10 kN, this warning arises after the first TO iteration. When the force exceeds 100 kN, COMSOL fails to complete the analysis before the first TO iteration.

Various aspects have been examined to address the challenges of implementing the Helmholtz filter. Initially, a segregated approach is used instead of the fully coupled approach. While the fully coupled method solves a single system of equations, the segregated approach subdivides the problem into distinct steps. In this model, the steps are the TO and the solid mechanics. Surprisingly, no differences are observed between the two models, concluding that the fully coupled and segregated approaches are equivalent in this context.

Furthermore, various solvers have been tested to analyse their impact on the results; however, these solvers yield identical outcomes. In a third investigation, diverse values for γ_e are applied and inspected for their effects, which are listed below. Here, X and Y are the horizontal and vertical coordinates of the design domain, respectively. Notably, the first four equations result in solutions, while the fifth introduces problems. The main difference is that in the first four equations, γ_e remains constant throughout each iteration. However, in the fifth equation, γ_e is a function of the variables associated with the TO and changes every iteration. This observation suggests that an γ_e dependent on TO variables leads to an unsolvable COMSOL model.

1. $\gamma_e = 4Y$
2. $\gamma_e = X^9$
3. $\gamma_e = \sin(1.5X)$
4. $\gamma_e = \frac{\tanh(\beta_1\eta_1)+\tanh(\beta_1(X^p-\eta_1))}{\tanh(\beta_1\eta_1)+\tanh(\beta_1(1-\eta 1))}$
5. $\gamma_e = \bar{\rho}_e$

Various aspects have been examined in an attempt to implement a filter, but none have shown to have an impact. Consequently, further research must be conducted to understand the relationship between the Helmholtz filter and the Wang method.

D.2. Changing the steepness of the Heaviside function

Initially, the variable β_1 is varied to explore its impact, with the corresponding results presented in Figure D.2. Here, η_1 is set to 0.01. Additionally, Table D.1 gives the objective functions and computational times associated with the problems. It is important to note that during the optimisation process, the obtained objective function values in the table are scaled based on the initial solution.

Examining the results in Table D.1, it is apparent that setting β_1 to 50 yields the lowest objective function, signifying the optimal outcome. However, the observed shape deviates from the configuration shown in Figure 5.7d. In contrast, both Figure D.2b and Figure D.2c exhibit designs similar to Figure 5.7d. Despite the similar objective functions for these designs, a notable difference in computational time exists. Consequently, it can be concluded that setting β_1 to 100 provides the optimal balance between objective function and computational efficiency. Additionally, setting β_1 to a value lower than 50 leads to divergence.

Parameter	Values					
β_1	50	100	150	200	300	500
Objective function	45700	48000	47600	47910	51700	53200
Computation time (min)	5	14	19	21	26	26

Table D.1: The objective function values for various values of β_1 for the TO of a cantilever beam incorporating the Wang method.

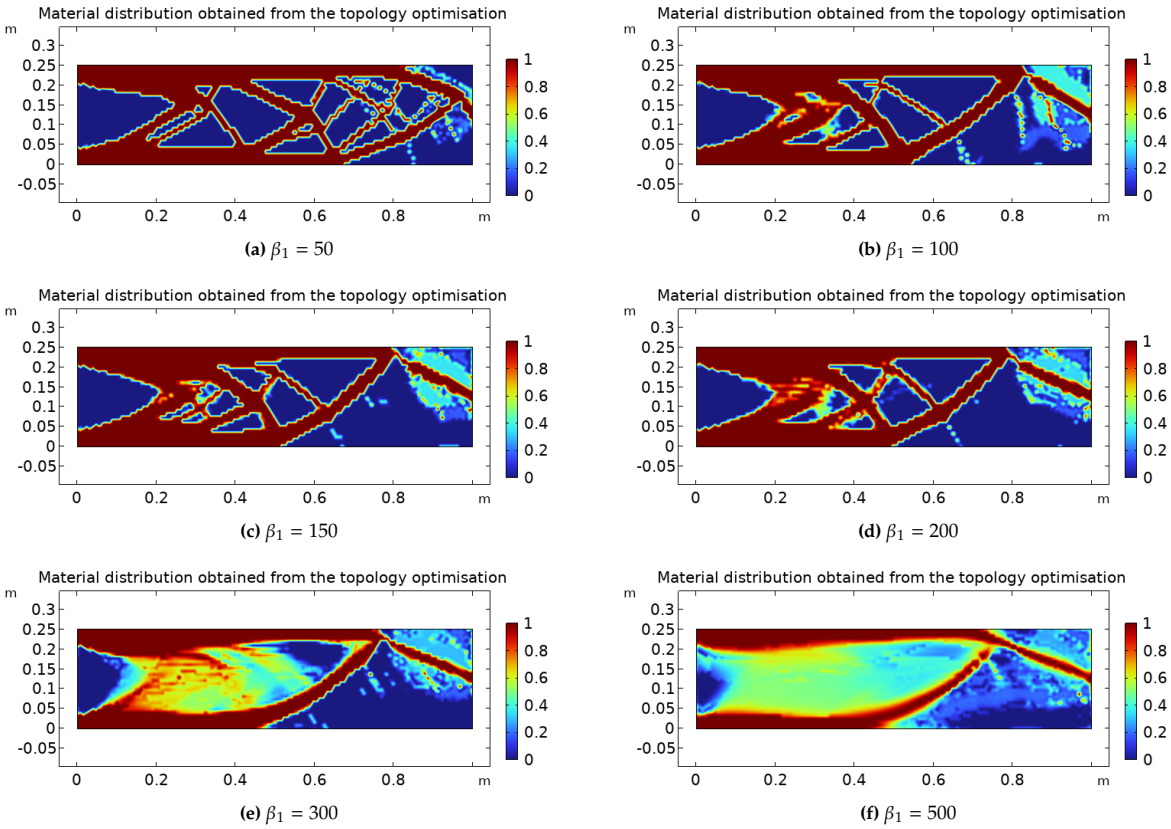

(a) $\beta_1 = 50$ **(b)** $\beta_1 = 100$

(c) $\beta_1 = 150$ **(d)** $\beta_1 = 200$

(e) $\beta_1 = 300$ **(f)** $\beta_1 = 500$

Figure D.2: The results obtained from the TO of a cantilever beam incorporating the Wang method, subjected to an applied force of 150 kN for varying values for β_1.

D.3. Changing the threshold of the Heaviside function

The second parameter to be adjusted is η_1 while keeping β_1 fixed at 100. In Figure D.3, the results for the TO of the cantilever beam, incorporating the Wang method, are illustrated for various values of η_1. The corresponding objective function values are detailed in Table D.2.

Results obtained for $\eta_1 < 0.0001$ are unfeasible, as the beam created on the right side separates from the structure. The most optimal objective function is achieved with a $\eta_1 = 0.001$; the computational time is also the lowest for this value. Therefore, the optimal solution is attained when η_1 is set to 0.001.

η_1 serves as the threshold determining the location of the transition between linear and nonlinear designs. Consequently, higher values for η_1 were anticipated to result in more linear designs. However, the obtained results contradict expectations, as increasing the value of η_1 leads to infeasible outcomes.

Parameter	Values							
η_1	0.00001	0.00005	0.0001	0.0005	0.001	0.005	0.01	0.05
Objective function	44500	44400	44600	44600	44500	46300	47800	52800
Computation time (min)	7	10	11	8	7	14	14	23

Table D.2: The objective function values for various values of η_1 for the TO of a cantilever beam incorporating the Wang method. The applied load is equal to 150 kN.

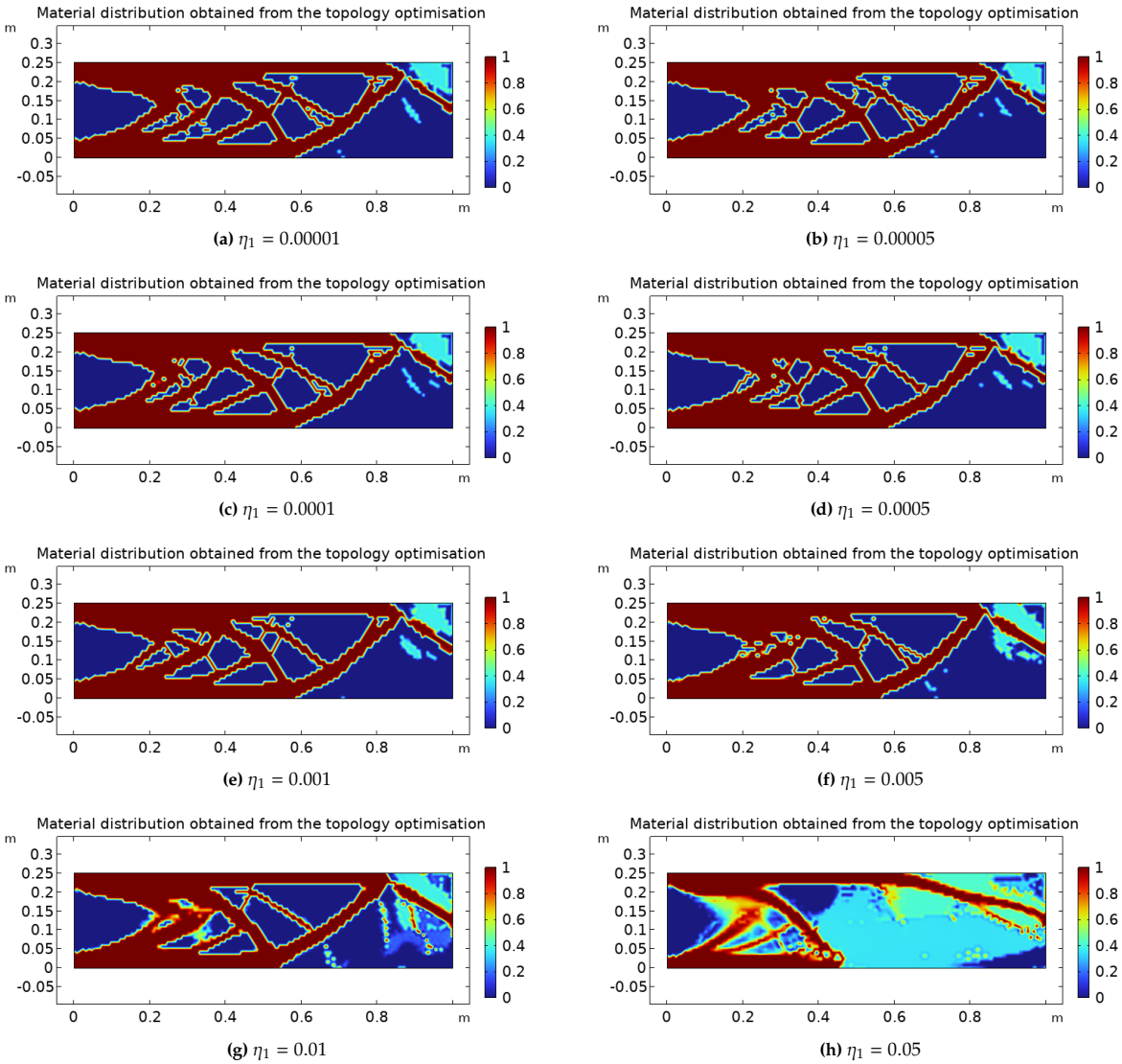

(a) $\eta_1 = 0.00001$ **(b)** $\eta_1 = 0.00005$

(c) $\eta_1 = 0.0001$ **(d)** $\eta_1 = 0.0005$

(e) $\eta_1 = 0.001$ **(f)** $\eta_1 = 0.005$

(g) $\eta_1 = 0.01$ **(h)** $\eta_1 = 0.05$

Figure D.3: The results of the TO of a cantilever beam incorporating the Wang method and is subjected to an applied force of 150 kN, for varying values for η_1, with β_1 held constant at 100.

To validate if $(\beta_1, \eta_1) = (100, 0.0005)$ remains optimal under higher loads, a similar investigation is conducted with a load of 250 kN, as illustrated in Figure D.4. The corresponding objective functions and computation times are presented in Table D.3.

From Table D.2 and Figure D.4, it is evident that a value of 0.01 for η_1 yields the most optimal solution, with the lowest objective function and computation time. Consequently, it can be concluded that $(\beta_1, \eta_1) = (100, 0.0005)$ remains the optimal solution under higher loads.

Parameter	Values			
η_1	0.0001	0.0005	0.001	0.005
Objective function	91700	92700	91400	98000
Computation time (min)	27	34	25	31

Table D.3: The objective function values and computational times for various values of η_1 for the TO of a cantilever beam incorporating the Wang method and the corresponding computation times. The applied load is equal to 250 kN.

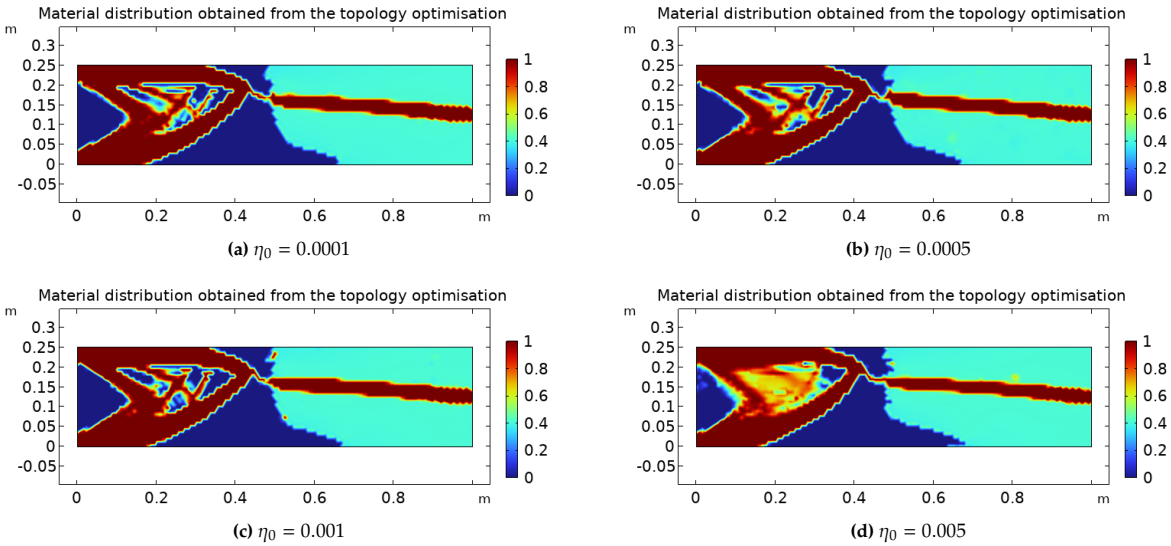

(a) $\eta_0 = 0.0001$ **(b)** $\eta_0 = 0.0005$

(c) $\eta_0 = 0.001$ **(d)** $\eta_0 = 0.005$

Figure D.4: The results obtained from the TO of a cantilever beam, which incorporates the Wang method and is subjected to an applied force of 250 kN for varying values of η_1, with β_1 held constant at 100.

D.4. Changing the penalisation factor

The last parameter that can be adjusted for γ_e is the penalisation factor p. By default, this is set to 3, which is considered the standard value in TO. However, observing the effects of changing this value can be interesting.

The results in Figure D.5 and Table D.4 demonstrate that higher values for p lead to worse outcomes compared to when p is set to 3 (Figure D.5b). Additionally, p equal to 2 yields a similar objective function to p equal to 3. However, there is also a notable difference in computational time.

Moreover, the shape of the resulting design for $p = 2$ produces results more closely aligned with those obtained from the TO employing a Neo-Hookean model for this specific load. Consequently, it can be asserted that $p = 2$ is the appropriate value. However, it is crucial to note that the obtained results are contingent on the simulation. The objective function varies with each computation, specifically oscillating between two values. This behaviour is notably peculiar and is not observed for $p = 3$. Hence, it can be inferred that a penalisation factor $p = 3$ provides the most optimal value for this parameter, as it introduces greater confidence in results and reduces computational time.

Parameter	Values			
Penalisation p	2	3	4	5
Objective function	44600	44500	47400	57300
Computation time (min)	12	7	7	9

Table D.4: The objective function values for various values of p for the TO of a cantilever beam incorporating the Wang method.

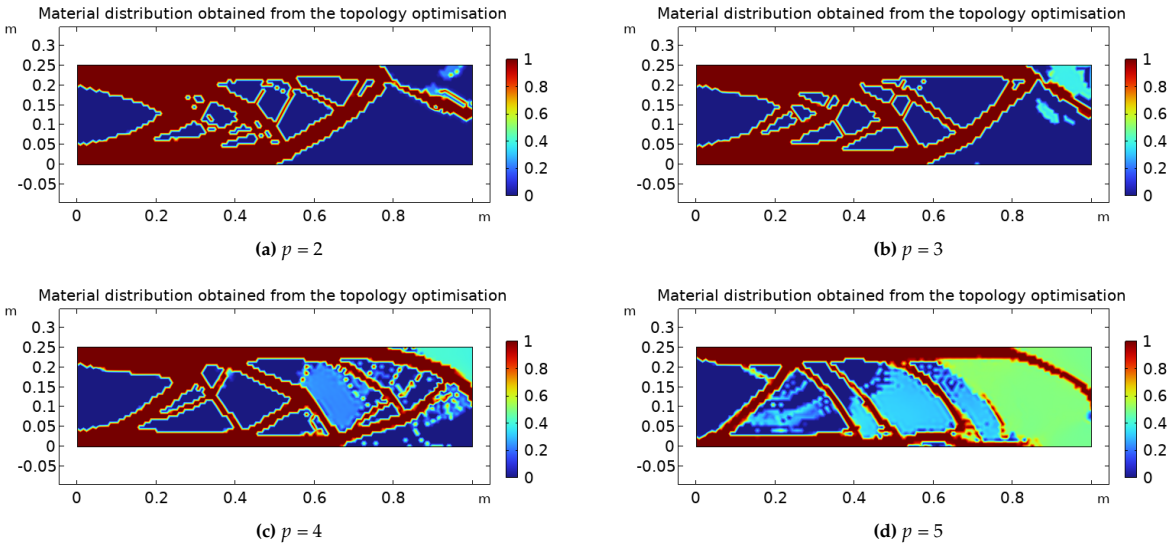

(a) $p = 2$ **(b)** $p = 3$

(c) $p = 4$ **(d)** $p = 5$

Figure D.5: The results obtained from the TO of a cantilever beam incorporating the Wang method and subjected to an applied force of 150 kN, for varying values for p, with β_1 and η_1 held constant at 100 and 0.001, respectively.

D.5. Adding Projection

The results presented in this section were obtained without a projection on the design variables. A test was conducted to observe the impact of introducing a projection on the design variables, and the results are illustrated in Figure D.6. It can be observed from Table D.5 that the objective function for the model with a projection has a notably lower value, indicating a more optimal solution. Despite the improvement in the objective function, the computational time is significantly higher compared to the model without the projection on the design variables. Therefore, the projection on the design variables will not be implemented in the models used in this thesis.

Parameter	Values	
Projection	No	Yes
Objective function	44500	41100
Computation time (min)	7	43

Table D.5: The objective function values obtained from the TO of a cantilever beam incorporating the Wang method, comparing implementations without and with projection.

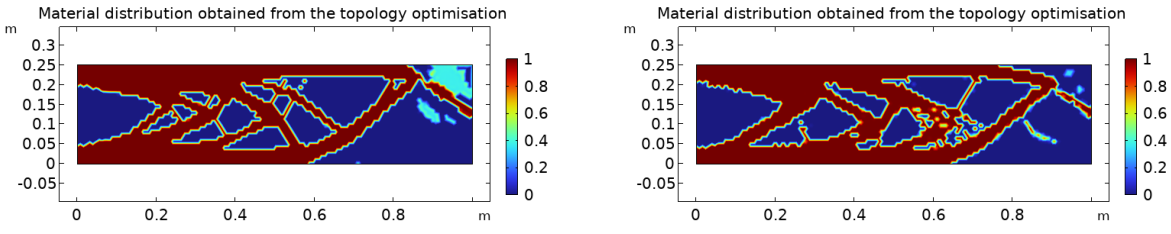

(a) Without projection **(b)** With projection

Figure D.6: The TO results of a cantilever beam using the Wang method under a 150 kN applied force, comparing implementations without (a) and with (b) projection. β_1, η_1, and p are held constant at 100, 0.001, and 3, respectively.

D.6. Topology optimisation of cantilever beam including the Wang method

This section presents the results obtained from the TO of a cantilever beam, incorporating the Wang method. The study explores various values of the applied force, as illustrated in Figure D.7. The parameters β_1, η_1, and p are set to 100, 0.001, and 3, respectively. The results show unexpected behaviour within the range of applied forces between 210 kN and 230 kN. During this interval, the structure undergoes a transition from a shape resembling Figure D.7e to one akin to Figure D.7g. COMSOL seems to encounter difficulties in achieving a smooth transition between these two shapes, and the cause of this phenomenon remains uncertain. Further investigation is needed to understand the underlying reasons for this behaviour.

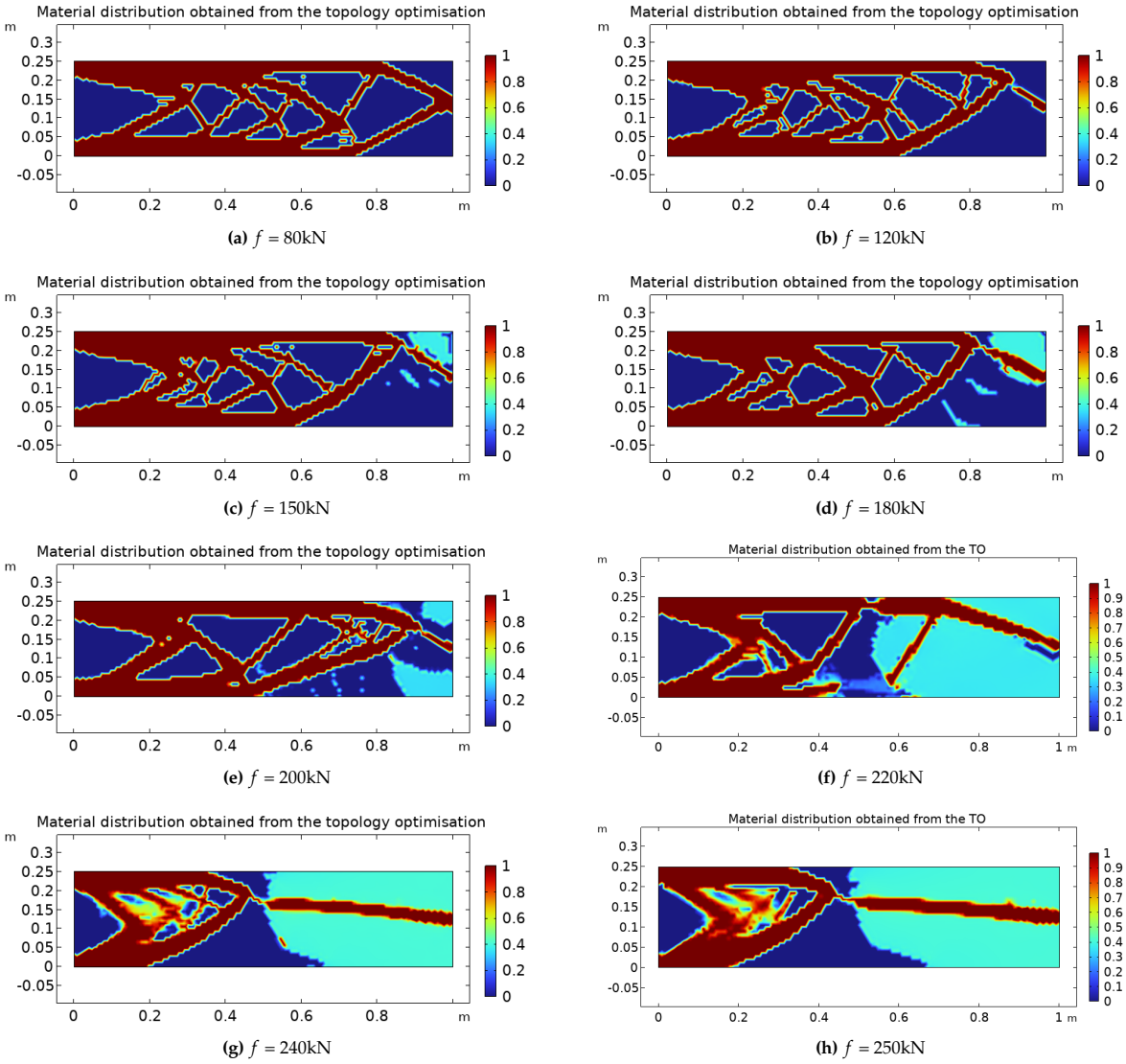

(a) $f = 80$kN **(b)** $f = 120$kN

(c) $f = 150$kN **(d)** $f = 180$kN

(e) $f = 200$kN **(f)** $f = 220$kN

(g) $f = 240$kN **(h)** $f = 250$kN

Figure D.7: The results of the TO of a cantilever beam incorporating the Wang method and subjected to various applied forces. β_1, η_1, and p held constant at 100, 0.001, and 3, respectively.

E

The codes of MATLAB

E.1. Code for the linear material model

This is a code that proves that the two linear strain energy density function are identical.

```
1
2  %constant
3  syms  nu E u_X u_Y v_X v_Y
4
5  %The parameters to calculate the value for the strain energy density
       functions
6  % nu = 0.4
7  % E = 180*10^6
8  % u_X = 0.03
9  % u_Y = 0.5
10 % v_X = 0.001
11 % v_Y = 0.9
12
13 %The Elastic moduli
14 D11 = E*(1-nu)/((1+nu)*(1-2*nu));
15 D12 = E*nu/((1+nu)*(1-2*nu));
16 D13 = E*nu/((1+nu)*(1-2*nu));
17 D14 = 0;
18 D15 = D14;
19 D16 = D14;
20 D22 = E*(1-nu)/((1+nu)*(1-2*nu));
21 D23 = E*nu/((1+nu)*(1-2*nu));
22 D24 = 0;
23 D25 = D24;
24 D26 = D24;
25 D33 = E*(1-nu)/((1+nu)*(1-2*nu));
26 D34 = 0;
27 D35 = D34;
28 D36 = D34;
29 D44 = 0.5*E/(1+nu);
30 D45 = 0;
31 D46 = D45;
32 D55 = 0.5*E/(1+nu);
33 D56 = D45;
34 D66 = 0.5*E/(1+nu);
35
```

```
D = [D11 D12 D13 D14 D15 D16; D12 D22 D23 D24 D25 D26;
    D13 D23 D33 D34 D35 D36; D14 D24 D34 D44 D45 D46;
    D15 D25 D35 D45 D55 D56; D16 D26 D36 D46 D56 D66]

% Calculating the strain matrix
e11 = u_X
e12 = 0.5*(u_Y+v_X)
e13 = 0;
e22 = v_Y
e23 = 0;
e33 = 0;

e = [e11 e12 e13; e12 e22 e23; e13 e23 e33];

% Calculating the Second Piola-Kirch stress tensor
S11 = D11*e11+D12*e22+D13*e33+2*D14*e12+2*D15*e23+2*D16*e13;
S12 = D14*e11+D24*e22+D34*e33+2*D44*e12+2*D45*e23+2*D46*e13;
S13 = D16*e11+D26*e22+D36*e33+2*D46*e12+2*D56*e23+2*D66*e13;
S22 = D12*e11+D22*e22+D24*e33+2*D24*e12+2*D25*e23+2*D26*e13;
S33 = D13*e11+D23*e22+D33*e33+2*D34*e12+2*D35*e23+2*D36*e13;
S23 = D15*e11+D25*e22+D35*e33+2*D45*e12+2*D55*e23+2*D56*e13;

S = [S11 S12 S13; S12 S22 S23; S13 S23 S33];

% Calculating the Lame parameters
mu_he= 0.5*E/(1+nu);
lambda = E*nu/((1+nu)*(1-2*nu));

% All the values for the parameters will be real
 assume(S, 'real');
 assume(e, 'real');
 assume(E,'real');
 assume(nu, 'real');
 assume([v_X, u_X, v_Y, u_Y, gamma_e], ['real'])

% Calculating the strain energy density functions
W = mu_he*dot(e(:),e(:))+ 0.5*lambda*trace(e)^2
Ws = 0.5*(dot(S(:),e(:)))
```

E.2. The code for the element material model interpolation method

```
%InterpolationStrainSEStress.mlx
%constant
clear all
close all
syms solidnu solidE uX uY vX vY gamma_e solidmuLame solidlambLame C11 C12
    C13 C23 C22 C33


format long
% Given values to the parameter, to calculate the values
solidnu = 0.4
solidE = 180*10^6
uX = 0.000192837
uY = 0.0000456456
vX = -0.000001
```

```
vY = -0.000000000000000777777777
gamma_e =0.7

solidmuLame= 0.5*solidE/(1+solidnu);
solidlambLame = solidE*solidnu/((1+solidnu)*(1-2*solidnu));


Calculating the strain energy density function for the nonlinear analysis

F11 = 1+uX*gamma_e ;
F12 = uY*gamma_e;
F13 = 0;
F21 = vX*gamma_e;
F22 = 1+vY*gamma_e;
F23 = 0;
F31 = 0;
F32 = 0;
F33 = 1;

C11 = F11^2+F21^2+F31^2;
C12 = F11*F12+F21*F22+F31*F32;
C13 = 0;
C22 = F12^2+F22^2+F32^2;
C23 = 0;
C33 = F13.^2+F23.^2+F33.^2;
C = [C11 C12 C13; C12 C22 C23; C13 C23 C33];

eXX = 0.5*(-1+C11);
eXY = 0.5*C12;
eXZ = 0.5*C13;
eYY = 0.5*(-1+C22)
eYZ = 0.5*C23;
eZZ = 0.5*(-1+C33);

I1_C = trace(C);

J_el = sqrt(det(C));

%hyperelastic
%phi_HE= 0.5*solidmuLame*(-3+I1_C)-solidmuLame*log(J_el)+0.5*solidlambLame
    *log(J_el)^2;
phi_HE_C = (solidlambLame*log(sqrt(- C33*C12^2 + 2*C12*C13*C23 - C22*C13^2
     - C11*C23^2 + C11*C22*C33))^2)/2 - solidmuLame*log(sqrt(- C33*C12^2 +
    2*C12*C13*C23 - C22*C13^2 - C11*C23^2 + C11*C22*C33)) + (solidmuLame*(
    C11 + C22 + C33 - 3))/2;
phi_HE_inter = (solidE*((gamma_e*uX + 1)^2 + gamma_e^2*uY^2 + gamma_e^2*vX
    ^2 + (gamma_e*vY + 1)^2 - 2))/(4*(solidnu + 1)) - (solidE*log(sqrt(((
    gamma_e*uX + 1)^2 + gamma_e^2*vX^2)*(gamma_e^2*uY^2 + (gamma_e*vY + 1)
    ^2) - (gamma_e*uY*(gamma_e*uX + 1) + gamma_e*vX*(gamma_e*vY + 1))^2)))
    /(2*(solidnu + 1)) - (solidE*solidnu*log(sqrt(((gamma_e*uX + 1)^2 +
    gamma_e^2*vX^2)*(gamma_e^2*uY^2 + (gamma_e*vY + 1)^2) - (gamma_e*uY*(
    gamma_e*uX + 1) + gamma_e*vX*(gamma_e*vY + 1))^2))^2)/(2*(2*solidnu -
    1)*(solidnu + 1));

Calculating the interpolated strain energy
%Linear St. Venant-Kirchhoff
```

```
phi_L = (solidlambLame*(uX + vY)^2)/2 + solidmuLame*(2*(uY/2 + vX/2)^2 + (uX)^2 + (vY)^2);

phi_L_inter = (solidlambLame*(uX*gamma_e + vY*gamma_e).^2)/2 + solidmuLame*(2*(uY*gamma_e/2 + vX*gamma_e/2).^2 + (uX*gamma_e).^2 + (vY*gamma_e).^2);


%Wang's method
%phi = phi_HE_inter-phi_L_inter+phi_L1;
phi = (solidE*((gamma_e*uX + 1)^2 + gamma_e^2*uY^2 + gamma_e^2*vX^2 + (gamma_e*vY + 1)^2 - 2))/(4*(solidnu + 1)) - (solidE*log(sqrt(gamma_e^4*uX^2*vY^2 - 2*gamma_e^4*uX*uY*vX*vY + gamma_e^4*uY^2*vX^2 + 2*gamma_e^3*uX^2*vY - 2*gamma_e^3*uX*uY*vX + 2*gamma_e^3*uX*vY^2 - 2*gamma_e^3*uY*vX*vY + gamma_e^2*uX^2 + 4*gamma_e^2*uX*vY - 2*gamma_e^2*uY*vX + gamma_e^2*vY^2 + 2*gamma_e*uX + 2*gamma_e*vY + 1)))/(2*(solidnu + 1)) + (solidE*(2*(uY/2 + vX/2)^2 + uX^2 + vY^2))/(2*(solidnu + 1)) - (solidE*(2*((gamma_e*uY)/2 + (gamma_e*vX)/2)^2 + gamma_e^2*uX^2 + gamma_e^2*vY^2))/(2*(solidnu + 1)) + (solidE*solidnu*(gamma_e*uX + gamma_e*vY)^2)/(2*(2*solidnu - 1)*(solidnu + 1)) - (solidE*solidnu*(uX + vY)^2)/(2*(2*solidnu - 1)*(solidnu + 1)) - (solidE*solidnu*log(sqrt(gamma_e^4*uX^2*vY^2 - 2*gamma_e^4*uX*uY*vX*vY + gamma_e^4*uY^2*vX^2 + 2*gamma_e^3*uX^2*vY - 2*gamma_e^3*uX*uY*vX + 2*gamma_e^3*uX*vY^2 - 2*gamma_e^3*uY*vX*vY + gamma_e^2*uX^2 + 4*gamma_e^2*uX*vY - 2*gamma_e^2*uY*vX + gamma_e^2*vY^2 + 2*gamma_e*uX + 2*gamma_e*vY + 1))^2)/(2*(2*solidnu - 1)*(solidnu + 1));

Calculating the stress for the linear part
S11_L = 2*((solidlambLame*(uX + vY))/2 + solidmuLame*uX);
S12_L = (solidmuLame*(uY + vX));
S13_L = 0;
S22_L = 2*((solidlambLame*(uX + vY))/2 + solidmuLame*vY);
S23_L = 0;
S33_L = 2*((solidlambLame*(uX + vY))/2);

S11_L_inter = 2*((solidlambLame*(uX*gamma_e + vY*gamma_e))/2 + solidmuLame*uX*gamma_e);
S12_L_inter =  solidmuLame*(uY*gamma_e + vX*gamma_e);
S13_L_inter = 0;
S22_L_inter = 2*((solidlambLame*(uX*gamma_e + vY*gamma_e))/2 + solidmuLame*vY*gamma_e);
S23_L_inter = 0;
S33_L_inter = 2*((solidlambLame*(uX*gamma_e + vY*gamma_e))/2);



Calculating the stress for the nonlinear part
%S11 = diff(phi_HE_C,C11)
%S11 = solidmuLame/2 - (solidmuLame*(C23^2 - C22*C33))/(2*(C33*C12^2 - 2*C12*C13*C23 + C22*C13^2 + C11*C23^2 - C11*C22*C33)) + (solidlambLame*log(sqrt(- C33*C12^2 + 2*C12*C13*C23 - C22*C13^2 - C11*C23^2 + C11*C22*C33))*(C23^2 - C22*C33))/(2*(C33*C12^2 - 2*C12*C13*C23 + C22*C13^2 + C11*C23^2 - C11*C22*C33))
S11_NL = 2*(solidmuLame/2 - (solidmuLame*(gamma_e^2*uY^2 + (gamma_e*vY + 1)^2))/(2*((gamma_e*uX + 1)^2 + gamma_e^2*vX^2)*(gamma_e^2*uY^2 + (gamma_e*vY + 1)^2) - 2*(gamma_e*uY*(gamma_e*uX + 1) + gamma_e*vX*(
```

```
    gamma_e*vY + 1))^2) + (solidlambLame*log(sqrt(((gamma_e*uX + 1)^2 +
    gamma_e^2*vX^2)*(gamma_e^2*uY^2 + (gamma_e*vY + 1)^2) - (gamma_e*uY*(
    gamma_e*uX + 1) + gamma_e*vX*(gamma_e*vY + 1))^2))*(gamma_e^2*uY^2 + (
    gamma_e*vY + 1)^2))/(2*((gamma_e*uX + 1)^2 + gamma_e^2*vX^2)*(gamma_e
    ^2*uY^2 + (gamma_e*vY + 1)^2) - 2*(gamma_e*uY*(gamma_e*uX + 1) +
    gamma_e*vX*(gamma_e*vY + 1))^2));
90
91  %S12 = diff(phi_HE_C,C12)
92  S12_d = (solidmuLame*(2*C13*C23 - 2*C12*C33))/(2*(C33*C12^2 - 2*C12*C13*
    C23 + C22*C13^2 + C11*C23^2 - C11*C22*C33)) - (solidlambLame*log(sqrt(-
     C33*C12^2 + 2*C12*C13*C23 - C22*C13^2 - C11*C23^2 + C11*C22*C33))*(2*
    C13*C23 - 2*C12*C33))/(2*(C33*C12^2 - 2*C12*C13*C23 + C22*C13^2 + C11*
    C23^2 - C11*C22*C33));
93  %S12_NL = (solidmuLame*(2*gamma_e*uY*(gamma_e*uX + 1) + 2*gamma_e*vX*(
    gamma_e*vY + 1)))/(2*((gamma_e*uX + 1)^2 + gamma_e^2*vX^2)*(gamma_e^2*
    uY^2 + (gamma_e*vY + 1)^2) - 2*(gamma_e*uY*(gamma_e*uX + 1) + gamma_e*
    vX*(gamma_e*vY + 1))^2) - (solidlambLame*log(sqrt(((gamma_e*uX + 1)^2 +
     gamma_e^2*vX^2)*(gamma_e^2*uY^2 + (gamma_e*vY + 1)^2) - (gamma_e*uY*(
    gamma_e*uX + 1) + gamma_e*vX*(gamma_e*vY + 1))^2))*(2*gamma_e*uY*(
    gamma_e*uX + 1) + 2*gamma_e*vX*(gamma_e*vY + 1)))/(2*((gamma_e*uX + 1)
    ^2 + gamma_e^2*vX^2)*(gamma_e^2*uY^2 + (gamma_e*vY + 1)^2) - 2*(gamma_e
    *uY*(gamma_e*uX + 1) + gamma_e*vX*(gamma_e*vY + 1))^2);
94  S12_NL = (solidmuLame*(2*gamma_e*uY*(gamma_e*uX + 1) + 2*gamma_e*vX*(
    gamma_e*vY + 1)))/(2*((gamma_e*uX + 1)^2 + gamma_e^2*vX^2)*(gamma_e^2*
    uY^2 + (gamma_e*vY + 1)^2) - 2*(gamma_e*uY*(gamma_e*uX + 1) + gamma_e*
    vX*(gamma_e*vY + 1))^2) - (solidlambLame*log(sqrt(sqrt((((gamma_e*uX +
    1)^2 + gamma_e^2*vX^2)*(gamma_e^2*uY^2 + (gamma_e*vY + 1)^2) - (gamma_e
    *uY*(gamma_e*uX + 1) + gamma_e*vX*(gamma_e*vY + 1))^2)^2)))*(2*gamma_e*
    uY*(gamma_e*uX + 1) + 2*gamma_e*vX*(gamma_e*vY + 1)))/(2*((gamma_e*uX +
     1)^2 + gamma_e^2*vX^2)*(gamma_e^2*uY^2 + (gamma_e*vY + 1)^2) - 2*(
    gamma_e*uY*(gamma_e*uX + 1) + gamma_e*vX*(gamma_e*vY + 1))^2);
95
96  %S13 = diff(phi_g1,C13)
97  %S13 = (solidmuLame*(2*C12*C23 - 2*C13*C22))/(2*(C33*C12^2 - 2*C12*C13*C23
     + C22*C13^2 + C11*C23^2 - C11*C22*C33)) - (solidlambLame*log(sqrt(-
    C33*C12^2 + 2*C12*C13*C23 - C22*C13^2 - C11*C23^2 + C11*C22*C33))*(2*
    C12*C23 - 2*C13*C22))/(2*(C33*C12^2 - 2*C12*C13*C23 + C22*C13^2 + C11*
    C23^2 - C11*C22*C33))
98  S13_NL = 0;
99
100 %S22 = diff(phi_HE_C,C22)
101 %S22 = solidmuLame/2 - (solidmuLame*(C13^2 - C11*C33))/(2*(C33*C12^2 - 2*
    C12*C13*C23 + C22*C13^2 + C11*C23^2 - C11*C22*C33)) + (solidlambLame*
    log(sqrt(- C33*C12^2 + 2*C12*C13*C23 - C22*C13^2 - C11*C23^2 + C11*C22*
    C33))*(C13^2 - C11*C33))/(2*(C33*C12^2 - 2*C12*C13*C23 + C22*C13^2 +
    C11*C23^2 - C11*C22*C33))
102 S22_NL = 2*(solidmuLame/2 - (solidmuLame*((gamma_e*uX + 1)^2 + gamma_e^2*
    vX^2))/(2*((gamma_e*uX + 1)^2 + gamma_e^2*vX^2)*(gamma_e^2*uY^2 + (
    gamma_e*vY + 1)^2) - 2*(gamma_e*uY*(gamma_e*uX + 1) + gamma_e*vX*(
    gamma_e*vY + 1))^2) + (solidlambLame*log(sqrt(((gamma_e*uX + 1)^2 +
    gamma_e^2*vX^2)*(gamma_e^2*uY^2 + (gamma_e*vY + 1)^2) - (gamma_e*uY*(
    gamma_e*uX + 1) + gamma_e*vX*(gamma_e*vY + 1))^2))*((gamma_e*uX + 1)^2
    + gamma_e^2*vX^2))/(2*((gamma_e*uX + 1)^2 + gamma_e^2*vX^2)*(gamma_e^2*
    uY^2 + (gamma_e*vY + 1)^2) - 2*(gamma_e*uY*(gamma_e*uX + 1) + gamma_e*
    vX*(gamma_e*vY + 1))^2));
103
```

```
104
105 %S23 = diff(phi_HE_C,C23)
106 %S23 = (solidmuLame*(2*C12*C13 - 2*C11*C23))/(2*(C33*C12^2 - 2*C12*C13*C23
     + C22*C13^2 + C11*C23^2 - C11*C22*C33)) - (solidlambLame*log(sqrt(-
    C33*C12^2 + 2*C12*C13*C23 - C22*C13^2 - C11*C23^2 + C11*C22*C33))*(2*
    C12*C13 - 2*C11*C23))/(2*(C33*C12^2 - 2*C12*C13*C23 + C22*C13^2 + C11*
    C23^2 - C11*C22*C33))
107 S23_NL = 0;
108
109 %S33 = diff(phi_HE_C,C33)
110 %S33 = solidmuLame/2 - (solidmuLame*(C12^2 - C11*C22))/(2*(C33*C12^2 - 2*
    C12*C13*C23 + C22*C13^2 + C11*C23^2 - C11*C22*C33)) + (solidlambLame*
    log(sqrt(- C33*C12^2 + 2*C12*C13*C23 - C22*C13^2 - C11*C23^2 + C11*C22*
    C33))*(C12^2 - C11*C22))/(2*(C33*C12^2 - 2*C12*C13*C23 + C22*C13^2 +
    C11*C23^2 - C11*C22*C33))
111 S33_NL = 2*(solidmuLame/2 - (solidmuLame*(((gamma_e*uX + 1)^2 + gamma_e^2*
    vX^2)*(gamma_e^2*uY^2 + (gamma_e*vY + 1)^2) - (gamma_e*uY*(gamma_e*uX +
     1) + gamma_e*vX*(gamma_e*vY + 1))^2))/(2*((gamma_e*uX + 1)^2 + gamma_e
    ^2*vX^2)*(gamma_e^2*uY^2 + (gamma_e*vY + 1)^2) - 2*(gamma_e*uY*(gamma_e
    *uX + 1) + gamma_e*vX*(gamma_e*vY + 1))^2) + (solidlambLame*log(sqrt
    ((((gamma_e*uX + 1)^2 + gamma_e^2*vX^2)*(gamma_e^2*uY^2 + (gamma_e*vY +
     1)^2) - (gamma_e*uY*(gamma_e*uX + 1) + gamma_e*vX*(gamma_e*vY + 1))^2)
    ))*(((gamma_e*uX + 1)^2 + gamma_e^2*vX^2)*(gamma_e^2*uY^2 + (gamma_e*vY
     + 1)^2) - (gamma_e*uY*(gamma_e*uX + 1) + gamma_e*vX*(gamma_e*vY + 1))
    ^2))/(2*((gamma_e*uX + 1)^2 + gamma_e^2*vX^2)*(gamma_e^2*uY^2 + (
    gamma_e*vY + 1)^2) - 2*(gamma_e*uY*(gamma_e*uX + 1) + gamma_e*vX*(
    gamma_e*vY + 1))^2));
112
113
114 Calculating Interpolating the stress
115 %S11 = S11_NL-S11_L_inter + S11_L
116 S11 = 2*(solidmuLame/2 + (solidlambLame*(uX + vY))/2 + solidmuLame*uX - (
    solidlambLame*(gamma_e*uX + gamma_e*vY))/2 - (solidmuLame*(gamma_e^2*uY
    ^2 + (gamma_e*vY + 1)^2))/((gamma_e^2*uY^2 + (gamma_e*vY + 1)^2)*(2*(
    gamma_e*uX + 1)^2 + 2*gamma_e^2*vX^2) - 2*(gamma_e*uY*(gamma_e*uX + 1)
    + gamma_e*vX*(gamma_e*vY + 1))^2) - gamma_e*solidmuLame*uX + (
    solidlambLame*log(sqrt(((gamma_e*uX + 1)^2 + gamma_e^2*vX^2)*(gamma_e
    ^2*uY^2 + (gamma_e*vY + 1)^2) - (gamma_e*uY*(gamma_e*uX + 1) + gamma_e*
    vX*(gamma_e*vY + 1))^2))*(gamma_e^2*uY^2 + (gamma_e*vY + 1)^2))/((
    gamma_e^2*uY^2 + (gamma_e*vY + 1)^2)*(2*(gamma_e*uX + 1)^2 + 2*gamma_e
    ^2*vX^2) - 2*(gamma_e*uY*(gamma_e*uX + 1) + gamma_e*vX*(gamma_e*vY + 1)
    )^2))
117
118 %S12 = S12_NL-S12_L_inter + S12_L
119 S12 = solidmuLame*(uY + vX) - solidmuLame*(gamma_e*uY + gamma_e*vX) + (
    solidmuLame*(2*gamma_e*uY*(gamma_e*uX + 1) + 2*gamma_e*vX*(gamma_e*vY +
     1)))/((gamma_e^2*uY^2 + (gamma_e*vY + 1)^2)*(2*(gamma_e*uX + 1)^2 + 2*
    gamma_e^2*vX^2) - 2*(gamma_e*uY*(gamma_e*uX + 1) + gamma_e*vX*(gamma_e*
    vY + 1))^2) - (solidlambLame*log(sqrt(((gamma_e*uX + 1)^2 + gamma_e^2*
    vX^2)*(gamma_e^2*uY^2 + (gamma_e*vY + 1)^2) - (gamma_e*uY*(gamma_e*uX +
     1) + gamma_e*vX*(gamma_e*vY + 1))^2))*(2*gamma_e*uY*(gamma_e*uX + 1) +
     2*gamma_e*vX*(gamma_e*vY + 1)))/((gamma_e^2*uY^2 + (gamma_e*vY + 1)^2)
    *(2*(gamma_e*uX + 1)^2 + 2*gamma_e^2*vX^2) - 2*(gamma_e*uY*(gamma_e*uX
    + 1) + gamma_e*vX*(gamma_e*vY + 1))^2)
120
121 %S13 = S13_NL-S13_L_inter + S13_L
```

```
S13 =0;

%S22 = S22_NL-S22_L_inter + S22_L
S22 = 2*(solidmuLame/2 + (solidlambLame*(uX + vY))/2 + solidmuLame*vY - (
    solidlambLame*(gamma_e*uX + gamma_e*vY))/2 - (solidmuLame*((gamma_e*uX
    + 1)^2 + gamma_e^2*vX^2))/((gamma_e^2*uY^2 + (gamma_e*vY + 1)^2)*(2*(
    gamma_e*uX + 1)^2 + 2*gamma_e^2*vX^2) - 2*(gamma_e*uY*(gamma_e*uX + 1)
    + gamma_e*vX*(gamma_e*vY + 1))^2) - gamma_e*solidmuLame*vY + (
    solidlambLame*log(sqrt(((gamma_e*uX + 1)^2 + gamma_e^2*vX^2)*(gamma_e
    ^2*uY^2 + (gamma_e*vY + 1)^2) - (gamma_e*uY*(gamma_e*uX + 1) + gamma_e*
    vX*(gamma_e*vY + 1))^2))*((gamma_e*uX + 1)^2 + gamma_e^2*vX^2))/((
    gamma_e^2*uY^2 + (gamma_e*vY + 1)^2)*(2*(gamma_e*uX + 1)^2 + 2*gamma_e
    ^2*vX^2) - 2*(gamma_e*uY*(gamma_e*uX + 1) + gamma_e*vX*(gamma_e*vY + 1)
    )^2))

%S23 = S23_NL-S23_L_inter + S23_L
S23 = 0;

%S33 = S33_NL-S33_L_inter + S33_L
S33 = 2*(solidmuLame/2 + (solidlambLame*(uX + vY))/2 - (solidlambLame*(
    gamma_e*uX + gamma_e*vY))/2 - (solidmuLame*(((gamma_e*uX + 1)^2 +
    gamma_e^2*vX^2)*(gamma_e^2*uY^2 + (gamma_e*vY + 1)^2) - (gamma_e*uY*(
    gamma_e*uX + 1) + gamma_e*vX*(gamma_e*vY + 1))^2))/((gamma_e^2*uY^2 + (
    gamma_e*vY + 1)^2)*(2*(gamma_e*uX + 1)^2 + 2*gamma_e^2*vX^2) - 2*(
    gamma_e*uY*(gamma_e*uX + 1) + gamma_e*vX*(gamma_e*vY + 1))^2) + (
    solidlambLame*log(sqrt((((gamma_e*uX + 1)^2 + gamma_e^2*vX^2)*(gamma_e
    ^2*uY^2 + (gamma_e*vY + 1)^2) - (gamma_e*uY*(gamma_e*uX + 1) + gamma_e*
    vX*(gamma_e*vY + 1))^2)))*(((gamma_e*uX + 1)^2 + gamma_e^2*vX^2)*(
    gamma_e^2*uY^2 + (gamma_e*vY + 1)^2) - (gamma_e*uY*(gamma_e*uX + 1) +
    gamma_e*vX*(gamma_e*vY + 1))^2))/((gamma_e^2*uY^2 + (gamma_e*vY + 1)^2)
    *(2*(gamma_e*uX + 1)^2 + 2*gamma_e^2*vX^2) - 2*(gamma_e*uY*(gamma_e*uX
    + 1) + gamma_e*vX*(gamma_e*vY + 1))^2))



Calculating interpolating the Strain


eXX_NL = (gamma_e*uX + 1)^2/2 + (gamma_e^2*vX^2)/2 - 1/2;
eXY_NL = (gamma_e*uY*(gamma_e*uX + 1))/2 + (gamma_e*vX*(gamma_e*vY + 1))
    /2;
eXZ_NL = 0;
eYY_NL = (gamma_e^2*uY^2)/2 + (gamma_e*vY + 1)^2/2 - 1/2;
eYZ_NL = 0;
eZZ_NL = 0;


e11_L = uX;
e12_L = 0.5*(uY+vX);
e13_L = 0;
e22_L = vY
e23_L = 0;
e33_L = 0;


e11_L_inter = uX*gamma_e;
```

```
e12_L_inter = 0.5*(uY*gamma_e+vX*gamma_e);
e13_L_inter = 0;
e22_L_inter = vY*gamma_e
e23_L_inter = 0;
e33_L_inter = 0;


%eXX_inter = eXX_NL - e11_L_inter + e11_L
eXX_inter = uX - gamma_e*uX + (gamma_e*uX + 1)^2/2 + (gamma_e^2*vX^2)/2 -
    (1/2);

%eXY_inter = eXY_NL - e12_L_inter + e12_L
eXY_inter = uY/2 + vX/2 - (gamma_e*uY)/2 - (gamma_e*vX)/2 + (gamma_e*uY*(
    gamma_e*uX + 1))/2 + (gamma_e*vX*(gamma_e*vY + 1))/2;

eXZ_inter = 0;

%eYY_inter = eYY_NL - e22_L_inter + e22_L
eYY_inter = vY - gamma_e*vY + (gamma_e^2*uY^2)/2 + (gamma_e*vY + 1)^2/2
    -0.5;

eYZ_inter = 0;
eZZ_inter = 0;
```